Solutions to the Cosmic Ray Fokker-Planck Equation and Time Dependent Diffusion Coefficients

by

Jordan Lasuik

A thesis submitted to the Faculty of Graduate Studies of
The University of Manitoba
in partial fulfillment of the requirements of the degree of

MASTER OF SCIENCE

Department of Physics and Astronomy
University of Manitoba
Winnipeg, Manitoba, Canada

Solutions to the Cosmic Ray Fokker-Planck Equation and Time Dependent Diffusion Coefficients

Jordan Lasuik

Supervisor: Dr. Andreas Shalchi

April 2, 2019

Abstract

For over a century the complicated nature of cosmic rays has provided mankind with many unanswered questions. Due to the non linear nature of turbulent magnetic fields and their interaction with charged particles there has been a mathematical struggle in the scientific community to find answers to some of these questions. In this thesis, the fundamental equation of cosmic ray propagation (the Fokker-Planck equation) is examined alongside its properties. The solution to this equation is found numerically, as well as approximated analytically, and the most popular models for the undetermined, Fokker-Planck scattering coefficient, are examined. As well, the perpendicular diffusion coefficients that drive the nature of cosmic ray propagation are examined by using the most contemporary theoretical model, time dependent UNLT theory. This theory demands assumptions for both the magnetic correlation tensor and the particle distribution function, therefore the most commonly made assumptions for each are explored.

Acknowledgements

I would like to thank my supervisor Andreas Shalchi for teaching me everything I know about magnetohydrodynamics, as well as for being a great supervisor and a brilliant physicist to work under.

I would like to thank the office staff in the department of physics and astronomy, Susan Beshta, Robyn Beaulieu, and Aymsley Bishop-Mahon for helping me and every other student in the department with an uncountable number of things.

I would like to thank the University of Manitoba and the Faculty of Science, for hosting me as a master's student.

I would like to thank NSERC and the UofM GETS program for helping fund my master's degree.

Lastly, I would like to thank every member of OPUS (2013-2019), who have made my time as an undergraduate and graduate student at the UofM far more interesting and fulfilling, as well for giving me the drive to never give up in my physics studies.

Without every one of these people/organizations, this thesis would not made been made possible.

Thank you all.

Contents

1 Introduction **4**
- 1.1 History . . . 4
- 1.2 Categories of Cosmic Rays . . . 4
- 1.3 Origins . . . 4
- 1.4 Importance in Modern Life . . . 5
- 1.5 Propagation . . . 5
- 1.6 The Unperturbed System . . . 5
- 1.7 Magnetic Turbulence . . . 6

2 The Fokker-Planck Equation **8**
- 2.1 History . . . 8
- 2.2 Numerical Solutions to the Fokker-Planck Equation . . . 9
  - 2.2.1 Numerical Differentiation . . . 9
  - 2.2.2 One Dimensional PDE Solving . . . 10
  - 2.2.3 Working in Higher Dimensions . . . 13
  - 2.2.4 Numerical Integration . . . 19
- 2.3 Modeling the Scattering Coefficient . . . 20
- 2.4 Comparing Analytic and Numerical Solutions . . . 27
- 2.5 Comparing Properties of Numerical Solutions . . . 32
- 2.6 Analytic Approximation to the Fokker-Planck Equation . . . 34
  - 2.6.1 The Setup . . . 34
  - 2.6.2 First-Order Approximation . . . 36
  - 2.6.3 Second-Order Approximation . . . 36
  - 2.6.4 Third-Order Approximation . . . 39
  - 2.6.5 Normalization . . . 43
  - 2.6.6 Deriving General Properties of the Solutions . . . 45
  - 2.6.7 Properties of the First-Order Solution . . . 48
  - 2.6.8 Properties of the Second-Order Solution . . . 48
  - 2.6.9 Properties of the Third-Order Solution . . . 51
  - 2.6.10 Integrated Solutions . . . 56

3 The Unified Non Linear Transport Theory **59**
- 3.1 Diffusive UNLT Theory . . . 59
- 3.2 Time Dependent UNLT Theory . . . 59
- 3.3 Turbulence Models . . . 61
  - 3.3.1 Noisy Slab Turbulence . . . 61
  - 3.3.2 Gaussian Correlation Model . . . 64
  - 3.3.3 2D Turbulence . . . 65
  - 3.3.4 Two-Component Turbulence . . . 68
  - 3.3.5 Numerical Methods . . . 71
- 3.4 Modeling the Perpendicular Exponential . . . 72
  - 3.4.1 Step Function Particle Distribution . . . 73
  - 3.4.2 Kappa Function Particle Distribution . . . 76

4 Discussion of Results **80**
- 4.1 Fokker-Planck Scattering Coefficient Models . . . 80
- 4.2 Approximate Solutions to the Fokker-Planck Equation . . . 80
- 4.3 Turbulence Models for Time Dependent UNLT Theory . . . 81
- 4.4 Particle Distribution Models for Time Dependent UNLT Theory . . . 82

5 Conclusion **82**

1 Introduction

1.1 History

In the late 19th century it was believed that electrical activity in the atmosphere stemmed from ionization of air by radioactive materials on Earth. However experiments in the early 20th century proved that this is not the case. In 1909 Theodor Wulf built an electrometer (see Hörandel (2013)) to measure the radiation levels at the bottom and the top of the Eiffel Tower. He found that there were higher rates of ionization at the top of the tower, and thus said that the ionization cannot be due entirely to Earth based radiation. This was not widely believed at first, but in 1911 Domenico Pacini showed that there was less radiation over lakes and seas than one meter below their surfaces (see Pacini (1912)), again showing that Earth based radiation cannot account for the majority of measured radiation. In the upcoming years from 1911-1913 Victor Hess conducted a series of balloon experiments (see Hess (1912)). He showed that atmospheric ionization dramatically increases as a function of altitude up past 6km in the atmosphere. These balloon experiments mark the discovery of cosmic radiation, and won Hess the Nobel Prize in 1936 (see NobelMedia (2018)). The term cosmic radiation however wasn't coined until the 1920s when Robert Millikan measured ionization levels from deep in lakes to high in the atmosphere at different locations all across the world (see Carlson & De Angelis (2011)). They were termed cosmic "rays" because he believed them to mostly consist of Gamma rays. This theory was disproved in 1927 when Jacob Clay showed that atmospheric radiation increased significantly with latitude, and therefore cosmic rays must be charged particles that are affected by the Earth's magnetic field (see Heisenberg (1946)). Eventually scientists came to realize that most (about %99 of) cosmic radiation was composed of protons, ionized helium nuclei, and electrons (see Heisenberg (1946)). Though some heavier particles called HZE (high atomic number and energy) ions are found as well. The high interest in the field of cosmic radiation in the early 20th century lead to other amazing insights and discoveries, such as the discovery of the positron.

1.2 Categories of Cosmic Rays

When scientists talk about cosmic rays, they are usually talking about one of two different types, primary or secondary rays. This research is specific to primary cosmic rays. These are cosmic rays which have not yet collided with any atmospheric particles. Once a primary cosmic ray has an interaction within the atmosphere it produces what are called secondary cosmic rays. These secondary cosmic rays have lower energies and consist of x-rays, muons, protons, alpha particles, pions, electrons, and neutrons (see Hooper & Scharff (1958)). Primary cosmic rays are detected via spacecraft outside of the Earth's atmosphere, or are traced back by the detection of secondary cosmic rays. This can be done because the paths of secondary cosmic rays usually lie within 1 deg of the path of the primary ray (see Mishev (2006)). Primary cosmic rays are those charged particles which approach earth from their source. Secondary cosmic rays are those which are produced by the interaction of primary cosmic rays with the atmosphere. The focus of this thesis is on the transport of primary cosmic rays. All primary cosmic rays can be put into four categories. Solar cosmic rays, which originate from the sun and travel through interplanetary space before reaching us (see Shalchi (2009)), galactic cosmic rays which originate mostly from supernovae and supernova remnants (see Blasi (2013)), extra-galactic cosmic rays, which can come from active galactic nuclei (AGN) (see Shalchi (2009)), and anomalous cosmic rays, whose origin is probably the near interstellar medium (see Christian (2011)). Each of these cosmic ray categories has a particular range of energies that they are found within (see Shalchi (2009)). Solar cosmic rays are found between $10-10^9 eV$, galactic cosmic rays are found between $10^9-10^{15} eV$, extra-galactic cosmic rays have energies of $10^{15}-10^{20} eV$, and anomalous cosmic rays are usually found to be around $10^6 eV$.

1.3 Origins

The origin of cosmic rays is often very difficult to determine. This is due to the fact that they are electrically charged and thus their trajectory is easily disturbed by any magnetic fields that they travel through between their source and the detector. One way to determine the origin of cosmic rays is to observe electromagnetic radiation produced by them at their source. This has been done in supernova remnants when cosmic rays travel in curved magnetic fields within the remnants, and thus produce

synchrotron radiation (see Shalchi (2009)). Another way is to model the effect that magnetic fields have on their trajectories. One cannot simply look at the mean fields of the systems these cosmic rays travel through to trace back their path, because there is a lot of turbulence in the galactic and solar magnetic fields. This magnetic turbulence is what gives the theory of cosmic ray propagation its non-linearity (see Shalchi (2009)). In 1948 Horace W. Babcock proposed the idea that cosmic rays were produced in magnetic variable stars (see Babcock (1948)). There have been many possible sources of cosmic rays identified since then, including quasars, supernovae, and active galactic nuclei. The validity of each of these as origins for cosmic rays has been debated but a general consensus has been achieved about the validity of some sources. Supernovae are the most agreed upon candidate for origins of extra-solar cosmic rays.

1.4 Importance in Modern Life

The study of cosmic rays is an ever increasingly important subject. As mankind begins to explore the universe one of the most difficult challenges is dealing with the threat of cosmic rays. In space travel, cosmic rays are a health threat. There are so many problems that this cosmic radiation can cause to human beings that they cannot all be listed here (see Townsend (2005)), some of these health threats include damage to skin tissue, increased risk of many types of cancer, haematopoietic syndrome, and cataracts. Even unmanned spacecraft have difficulty with radiation (see Stassinopoulos & Raymond (1988)). For instance, the Voyager 2 incident, which caused it to transmit unreadable data, was credited to the flipping of a single bit due to the interaction with a cosmic ray. This means that in order to achieve safer space flight for both manned and unmanned spacecraft mankind's understanding of cosmic rays must be furthered. Even on Earth, some problems are caused by cosmic rays. Earth's magnetosphere and atmosphere shield us from most of the energy cosmic rays bring to Earth, however it is not always enough. Even after propagating all the way to the surface cosmic rays still often have enough energy to interfere with electronics. This is happening more often, as technology allows for smaller and smaller transistors (see Ziegler *et al.* (1996)). Events that cause large amounts of cosmic rays to reach Earth such as solar flares or galactic supernovae could cause large scale issues due to groups of coinciding soft errors in computing systems across the world (see Ziegler (1996)).

1.5 Propagation

Among the interesting mysteries of cosmic rays is their complex propagation behaviour. Since these particles are usually traveling through magnetic fields in interstellar and interplanetary space, they are often interacting with turbulent fields. In these environments the magnetic fields are orders higher in magnitude than the electric fields. Therefore the specific interaction between cosmic rays and turbulent magnetic fields is most relevant. This process is inherently both statistical and non-linear, which makes it a difficult problem to solve. An unperturbed particle in a static field follows a helical path, but with turbulent fields this path is different in two significant ways. Firstly, the particle undergoes parallel and perpendicular scattering. When the words parallel and perpendicular are used in the context of turbulent particles transport the reference line is the mean background magnetic field. Secondly, the particles undergo velocity diffusion which over time means the particles will lose all information of their initial velocity distribution. These diffusion and scattering effects are the main study of this thesis.

1.6 The Unperturbed System

The most basic system that can be discussed is that of charged particles interacting with non-turbulent, magnetic fields. When the magnetic fields are non-turbulent the particles undergo propagation governed by the Lorentz force. This force is governed by the equation,

$$\frac{d}{dt}\vec{p} = q\left(\vec{E} + \frac{\vec{v}}{c} \times \vec{B}\right), \tag{1}$$

where $\vec{p}$ is the momentum of the particle, q is the particle's charge, $\vec{v}$ is the particle's velocity, and $\vec{E}$ and $\vec{B}$ are the electric and magnetic fields of the system. Although its turbulence does cause some momentum

diffusion effects, the electric field $\vec{E}$ is often ignored. Therefore the problem can be restated as,

$$\frac{d}{dt}\vec{p} = \frac{q\vec{v}}{c} \times \vec{B}. \tag{2}$$

The kinetic energy of these particles is conserved in this equation and thus the particles have a constant speed, $|\vec{v}| = constant$. After defining a coordinate system such that $\vec{B} = B_0\hat{z}$ the equations of motion are determined to be,

$$\begin{aligned} \dot{\vec{v}}_x &= \Omega\vec{v}_y, \\ \dot{\vec{v}}_y &= -\Omega\vec{v}_x, \\ \dot{\vec{v}}_z &= 0. \end{aligned} \tag{3}$$

where Ω is the relativistic gyro-frequency

$$\Omega = \frac{qB_0}{mc}\sqrt{1 - \frac{v^2}{c^2}}. \tag{4}$$

Here m is the particle's rest mass, and c is the speed of light in vacuum. These equations can be solved as

$$\begin{aligned} \vec{v}_x &= v_\perp cos(\Phi_0 - \Omega t), \\ \vec{v}_y &= v_\perp sin(\Phi_0 - \Omega t), \\ \vec{v}_z &= const. = v_\parallel, \end{aligned} \tag{5}$$

where $v_\perp$ and $v_\parallel$ are the velocity components perpendicular and parallel to the mean magnetic field, and the $\hat{z}$ direction, and Φ_0 is the initial gyro-phase (see Shalchi (2009)). These equations can be integrated to find the exact particle trajectories

$$\begin{aligned} x &= x_0 + \frac{v_\perp}{\Omega}\Big(sin(\Phi_0) - sin(\Phi_0 - \Omega t)\Big), \\ y &= y_0 + \frac{v_\perp}{\Omega}\Big(cos(\Phi_0) + cos(\Phi_0 - \Omega t)\Big), \\ z &= z_0 + v_\parallel t. \end{aligned} \tag{6}$$

These equations describe simple helical motion around the mean magnetic field, as well as linear propagation along that mean field. This is of course a non-statistical description because of the lack of statistical processes, however once turbulence is introduced a statistical description is required to describe the system.

1.7 Magnetic Turbulence

The turbulence of magnetic fields can be introduced as follows,

$$\vec{B} = B_0\hat{z} + \delta\vec{B}, \tag{7}$$

where $\delta\vec{B}$ is the turbulent component of the field. With turbulence, the equations of motion become,

$$\begin{aligned} \dot{v}_x &= \Omega\Big(v_y\big(1 + \frac{\delta B_z}{B_0}\big) - v_z\frac{\delta B_y}{B_0}\Big), \\ \dot{v}_y &= \Omega\Big(-v_x\big(1 + \frac{\delta B_z}{B_0}\big) + v_z\frac{\delta B_x}{B_0}\Big), \\ \dot{v}_z &= \Omega\Big(v_x\frac{\delta B_y}{B_0} - v_y\frac{\delta B_x}{B_0}\Big). \end{aligned} \tag{8}$$

These equations are not as easy to solve because δB can be a function of both position, $\vec{x}$, and time, t. To move on, properties of the statistical system are considered. The basis of statistical descriptions of

these systems is an equation called the Fokker-Planck equation. To understand the importance of this equation diffusion coefficients must first be understood. Diffusion coefficients describe particle transport in turbulent systems. The mean squared displacement of the particles in a turbulent system is defined as

$$< (\Delta x)^2 >= \left\langle \big(x(t) - x(0)\big)^2 \right\rangle. \tag{9}$$

The form of the mean squared displacement is usually assumed to be $< (\Delta x)^2 > \propto t^\sigma$ where the value of σ directly determines the type of diffusion of the system as follows.

$$\begin{aligned} &\text{For} \\ &0 < \sigma < 1 \quad \text{the system experiences sub-diffusion,} \\ &\sigma = 1 \quad \text{the system experiences Markovian diffusion,} \\ &1 < \sigma < 2 \quad \text{the system experiences super-diffusion, and for} \\ &\sigma = 2 \quad \text{the system experiences ballistic motion.} \end{aligned} \tag{10}$$

The running diffusion coefficient is defined in terms of the mean squared displacement,

$$\kappa_{xx}(t) = \frac{< (\Delta x)^2 >}{2t}, \tag{11}$$

where x can be any component of the Cartesian coordinate system. The two most important diffusion coefficients are called the perpendicular coefficient and the parallel diffusion coefficient. Using the specific variables of the Cartesian coordinate system and making use of the symmetry in the x-y plane, they are defined respectively as

$$\begin{aligned} \kappa_{xx} &= \kappa_{yy} = \kappa_\perp, \\ \kappa_{zz} &= \kappa_\parallel. \end{aligned} \tag{12}$$

These diffusion coefficients are not only extremely important in understanding how these turbulent systems work, but they are also directly related to the Fokker-Planck equation mentioned previously. The Fokker-Planck equation was developed in the early 1900's by Adriaan Fokker and Max Planck to describe the probability distribution function of particles experiencing both Brownian motion as well as outside forces (see Planck (1917)). In this case, the 2-D Fokker-Planck equation is

$$\frac{\partial f}{\partial t} = -v\mu\frac{\partial f}{\partial z} + \frac{\partial}{\partial \mu}\left(D_{\mu\mu}\frac{\partial f}{\partial \mu}\right), \tag{13}$$

where $f = f(\mu, z, t)$ is the ensemble averaged particle distribution function, $D_{\mu\mu}$ is called the pitch angle Fokker-Planck coefficient, and μ is the pitch angle cosine, defined as $\mu = cos(\theta)$, where θ is the angle between the particle's velocity vector and the mean magnetic field. Taking the solution $f(\mu, z, t)$ and considering its integral over μ-space results in the solution to the diffusion equation. Specifically,

$$F(z,t) = \frac{1}{2}\int_{-1}^{1} d\mu f(\mu, z, t) \tag{14}$$

is the solution to

$$\frac{\partial F}{\partial t} = \kappa_\parallel \frac{\partial^2 F}{\partial z^2}, \tag{15}$$

where $\kappa_\parallel$ is given by

$$\kappa_\parallel = \frac{v^2}{8}\int_{-1}^{1} \frac{(1-\mu^2)^2}{D_{\mu\mu}}. \tag{16}$$

This relation between the diffusion coefficient $\kappa_\parallel$ and the pitch angle Fokker-Planck coefficient, allows for the calculation of the diffusion coefficient. Other such relations and theories are discussed later. Since these theories are all related to the Fokker-Planck equation it is important to first attempt a solution to this equation.

2 The Fokker-Planck Equation

2.1 History

An in depth discussion of the Fokker-Planck equation as it is related to cosmic ray transport must of course begin with Max Planck and Adriaan Fokker. In the early 20th century Adriaan Fokker and Max Planck were doing research in the field of statistics. They came up with a way to model the change in the probability density of a particle's velocity over time when said particle is being acted on by both drag forces and stochastic forces. The following shows the equation modeled in one spatial dimension,

$$\frac{\partial \rho(x,t)}{\partial t} = -\frac{\partial}{\partial x}[\mu(x,t)\rho(x,t)] + \frac{\partial^2}{\partial x^2}[D(x,t)\rho(x,t)], \tag{17}$$

where ρ is the particle density function, t is time, μ is the drift velocity, and D is a diffusion coefficient. This equation is used in many different systems. For example if there is no drift velocity and a constant diffusion coefficient, then the standard Brownian motion equation emerges, also known as the Wiener process (see Revuz & Yor (2013)). Another example is if there is a drag force like friction and the diffusion coefficient has dependencies on its environment the Ornstein-Uhlenbeck equation emerges, which describes a massive particle undergoing a random walk process with friction taken into account (see Jacobsen (1996)). In 1966, a paper was published by J.R. Jokipii (see Jokipii (1966)) that took this statistical partial differential equation (PDE) and applied it to systems involving charged particles such as cosmic rays traveling through turbulent magnetic fields. This was not the first time this equation was applied to these systems, but it was the first time it was written in terms of observables rather than in terms of the mean step length.

$$\frac{\partial f}{\partial t} = -\mu v\frac{\partial f}{\partial z} + \frac{1}{2}\frac{\partial}{\partial \mu}\left[\frac{<(\Delta\mu)^2>}{\Delta t}\frac{\partial f}{\partial \mu}\right] + \frac{1}{2}\frac{<(\Delta x)^2>}{\Delta t}\left(\frac{\partial^2 f}{\partial x^2} + \frac{\partial^2 f}{\partial y^2}\right), \tag{18}$$

where f is the particle density function, t is time, v is the velocity of the particle, μ is the cosine of the angle between the particle's velocity vector and the local magnetic field (pitch angle), z is the coordinate that is parallel to the mean magnetic field, and x and y are the coordinates orthogonal to the mean magnetic field. It should be noted that the Fokker-Planck equation being dealt with here is now modeled for four dimensions. The three spatial dimensions and one dimension that describes the pitch angle of the particle. There are only a diffusive term in spatial dimensions that are orthogonal to the mean magnetic field, and a linear term in the spatial dimension parallel to the mean magnetic field due to the nature of the situation. Figure (1) shows the situation that is modeled by this equation.

The mean magnetic field of course has perturbations which are not shown visually in the figure and cause not only parallel spatial diffusion but also diffusion in pitch angle and in orbital radius. If particle motion in the $x-y$ plane is neglected the equation is simplified to the following,

$$\frac{\partial f}{\partial t} = -\mu v\frac{\partial f}{\partial z} + \frac{1}{2}\frac{\partial}{\partial \mu}\left[\frac{<(\Delta\mu)^2>}{\Delta t}\frac{\partial f}{\partial \mu}\right]. \tag{19}$$

with the pitch angle Fokker-Planck coefficient, $\frac{<\Delta\mu^2>}{2\Delta t} = D_{\mu\mu}$, we can write this as

$$\frac{\partial f}{\partial t} = -v\mu\frac{\partial f}{\partial z} + \frac{\partial}{\partial \mu}\left[D_{\mu\mu}(\mu)\frac{\partial f}{\partial \mu}\right]. \tag{20}$$

It can be defined as some constant D multiplied by some function $g(\mu)$ whose only dependence is on μ. However there are many different ways of modeling this function and there has yet to be a consensus on the most accurate form of $D_{\mu\mu}$. Later different ways to model $D_{\mu\mu}$ are examined, and then given these models some analytic solutions to the PDE (see Lasuik & Shalchi (2017)) are compared to numerical solution properties. First though, the process of solving this equation numerically is examined.

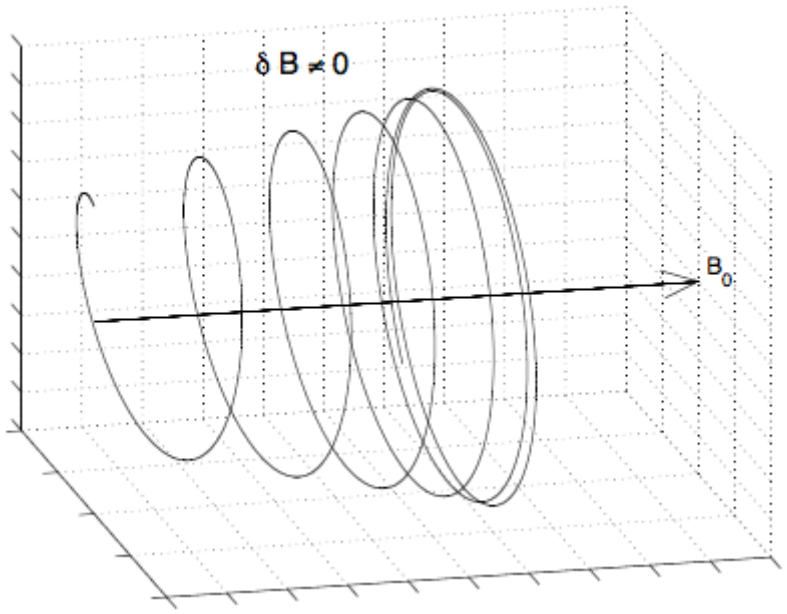

Figure 1: Figure from Shalchi (2009). Here a charged particle is moving through a turbulent magnetic field. The particle experiences a change in pitch angle, which causes spatial diffusion parallel to the magnetic field. It should be noted that due to pitch angle scattering at a 90° angle, the particle can return to a previous position.

2.2 Numerical Solutions to the Fokker-Planck Equation

2.2.1 Numerical Differentiation

In order to understand the numerical methods involved in solving partial differential equations, numerical differentiation must be discussed first. The definition of a derivative at $x = x_0$ is,

$$f'(x_0) = \lim_{h \to 0} \frac{f(x_0 + h) - f(x_0)}{h}. \tag{21}$$

By simply setting the grid spacing, h, to be extremely small, and taking the difference between adjacent values in the function then dividing by the grid spacing an approximate derivative of the function can be found. This method is called forward differencing. There are more accurate methods that can be utilized to solve derivatives, and those methods will be used when doing derivatives that are necessary for finding properties of the solutions. However when solving a PDE so many derivatives have to be repeatedly, therefore forward differencing is used because it is a fast and efficient method. It is important to note as well that there are second derivative terms in the PDE so the limit version of the second derivative definition at $x = x_0$ must also be utilized (see Thomson (1994)),

$$f''(x_0) = \lim_{h \to 0} \frac{f(x_0 + h) - 2f(x_0) + f(x_0 - h)}{h^2}. \tag{22}$$

Given this definition it is easy to see how to find a derivative numerically. This is the basis for one dimensional PDE solving.

One question that might be raised before moving on is how to find the derivative at the boundaries of a function. Since numerical functions always have a finite domain, there will arise a difficulty of having to find the value of the derivative at the beginning and end of the domain. Numerically, the functions, f(x), are actually just arrays of values where each i^{th} value in the array corresponds to the x value that is represented by the i^{th} bin in the array. The basic method of solving the derivative at any bin, i, requires

one to know the value of the function at not only the i^{th} bin, but also the $i+1^{th}$ bin for first derivatives, and both the $i+1^{th}$ bin and the $i-1^{th}$ bin for second derivatives. Since there is no known value for the $i-1^{th}$ bin when i is the first bin, and similarly there is no known value for the $i+1^{th}$ bin when i is the last bin in the array one must find another method of determining the derivative at these end points.

For the first derivative boundary there is only a problem with the last bin. To remove this problem one can employ what is called a backwards differencing formula. Instead of taking the $i+1^{th}$ bin and subtracting from it the i^{th} bin, one can take the i^{th} bin and subtract from it the $i-1^{th}$ bin as shown in the following equation,

$$f'(x_0) = \lim_{h \to 0} \frac{f(x_0) - f(x_0 - h)}{h}. \tag{23}$$

Unfortunately there is no such luxury of being able to difference from the other side in second derivatives. This is because information is needed about the bins on either side of the point where the derivative is to be determined. In these cases a more complex differencing formula can be used which requires the function to be expanded into its Taylor series and then approximated. Alternatively one can simply do the first derivative twice at these end points. It should be noted that while these methods must be utilized to find derivatives involved in solution properties to actually solve the PDE these methods are not needed due to the use of boundary conditions. This will be discussed in the next section.

2.2.2 One Dimensional PDE Solving

A more simple, one dimensional, form of the Fokker-Planck equation exists. This is the z-integrated Fokker-Planck equation,

$$\frac{\partial f}{\partial t} = D'_{\mu\mu}(\mu)\frac{\partial f}{\partial \mu} + D_{\mu\mu}(\mu)\frac{\partial^2 f}{\partial \mu^2}. \tag{24}$$

To solve the two dimensional Fokker-Planck equation first the one dimensional PDE solving methods must be examined. The basis of these are the so called explicit and implicit methods. The explicit method is the fastest, most efficient, but also least stable method. The method works as follows. In equation (24) there are both first and second-order derivatives, the equation is written out in the form shown in section (2.2.1), using equations (21) and (22) the following equation can be derived,

$$\begin{aligned} \frac{f(t_{j+1},\mu_i) - f(t_j,\mu_i)}{k} &= D'_{\mu\mu}(\mu)\frac{f(t_j,\mu_i) - f(t_j,\mu_{i-1})}{w} \\ &+ D_{\mu\mu}(\mu)\frac{f(t_j,\mu_{i+1}) - 2f(t_j,\mu_i) + f(t_j,\mu_{i-1})}{w^2}, \end{aligned} \tag{25}$$

where the index j indicates the bin in time which is being evaluated and the index i indicates the bin in μ which is being evaluated. The parameter k is defined as the t value at the j^{th} bin divided by the bin number j and w is defined as the μ value at the i^{th} bin divided by the bin number i. It can be noted that k and w are step sizes in the grid in the time and μ dimensions respectively.

Equation (20) has an initial condition which means that the solution at $t = 0$ which corresponds to $t_{1,i}$ for all i is known. That solution can then be propagated forwards in time. So the solution at each successive time step can be found given the solution at the previous time step. To put the equation in a form that reflects this equation (25) is rearranged to the following form,

$$\begin{aligned} f(t_{j+1},\mu_i) = f(t_j,\mu_i) + k\Bigg(& D'_{\mu\mu}(\mu)\frac{f(t_j,\mu_i) - f(t_j,\mu_{i-1})}{w} \\ & + D_{\mu\mu}(\mu)\frac{f(t_j,\mu_{i+1}) - 2f(t_j,\mu_i) + f(t_j,\mu_{i-1})}{w^2}\Bigg). \end{aligned} \tag{26}$$

In this equation the terms depending on the next time step are separated from the terms depending on the current time step. It is easy to see now that the value at bin i for the next time step is a function of the values in bins $i-1$, i, and $i+1$ at the current time step. This is the basic explicit differencing method and is visualized in figure (2).

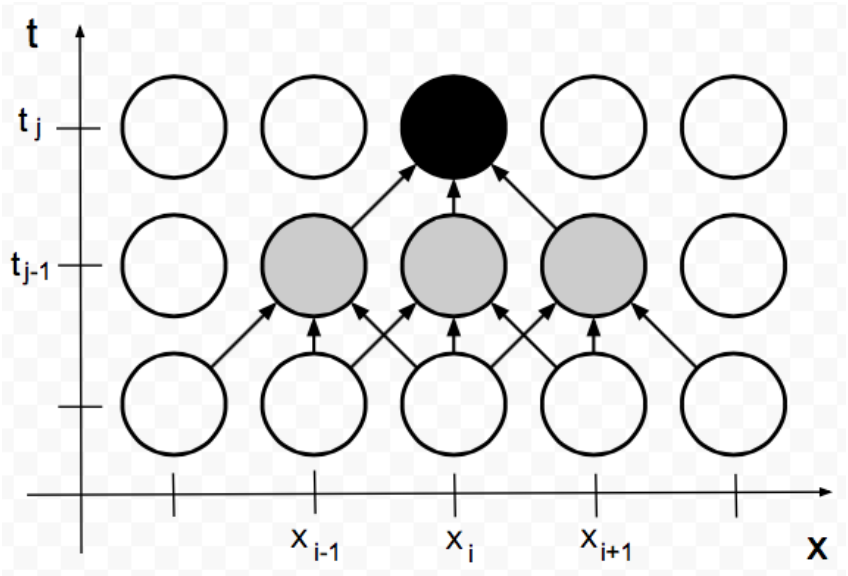

Figure 2: Arrows show the dependencies the value at a point has on the values at other points. The second row shows dependencies for all midpoints (points that are not boundary cases). The top row shows the dependencies that only the black dot has. These points that allow one to solve for the value at the black dot, are coloured grey. It is important to note that all gray dots are in a separate row from the black one.

The implicit method is a more advanced, slower, but more stable method of numerical PDE solving. The stability of these methods is discussed in Burden & Faires (1993). It works as follows. In an implicit method the indices in which the time derivative is taken are shifted. This method uses the backwards differencing formula (23) for the time derivative, while maintaining forward differencing for the μ derivative. Equation (26) using the implicit method becomes,

$$\begin{aligned} f(t_j,\mu_i) - k\Bigg(D'_{\mu\mu}(\mu)\frac{f(t_j,\mu_i) - f(t_j,\mu_{i-1})}{w} \\ + D_{\mu\mu}(\mu)\frac{f(t_j,\mu_{i+1}) - 2f(t_j,\mu_i) + f(t_j,\mu_{i-1})}{w^2}\Bigg) = f(t_{j-1},\mu_i). \end{aligned} \tag{27}$$

Now the value at bin i for the next time step is a function of the values in bins $i-1$, and $i+1$ at that next time step as well as the value in bin i at the current time step. This is an implicit differencing method and is visualized in figure (3).

It appears that there is a problem with this though because in order to determine the value in bin i at the next time step one needs to know the values in the bin next to it at that same future time step, but in order to determine them, one must know the values in the bins next to them and so on and so forth. This essentially results in a system of linear equations that need to be solved in order to determine the values in all of these bins. The system of linear equations however has l equations, where l is the total number of bins in the μ dimension, but $l+2$ unknowns because the equations corresponding to the bins at the beginning and end of the array require information about the bins next to them which do not exist. This problem is solved by employing the boundary conditions of the PDE. Boundary conditions allow the value in the first and last bin to be set given information about the physical nature of the system alone. For instance, for the one dimensional Fokker-Planck equation the coordinate μ is a pitch angle cosine which is symmetric about the $\theta = \pi$ point, and the $\theta = 0$. The boundaries are at $\mu = \pm 1$, which correspond to the points at which the cosine is symmetric. This means that if there were a bin on the outside of the boundary points it would be identical to the bins just inside the boundary points.

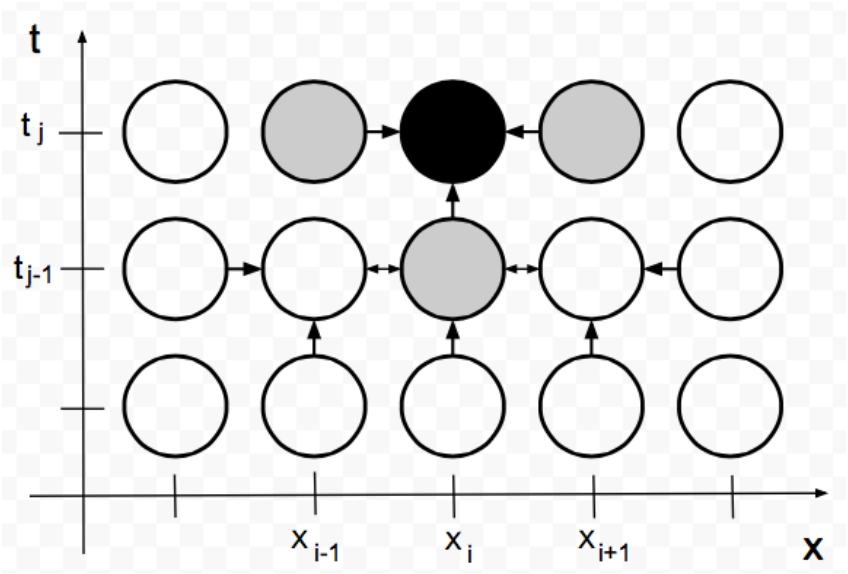

Figure 3: Arrows show the dependencies the value at a point has on the values at other points. The second row shows dependencies for all midpoints (points that are not boundary cases). The top row shows the dependencies that only the black dot has. These points that allow one to solve for the value at the black dot, are coloured grey. There are now grey dots that are in the same row as the black one.

This allows one to use these bins inside the boundary points twice, once as themselves and once as if they were the bins outside of the boundary points, thus adding two more equations to the system and the number of equations and unknowns equal. The system of equations can now be solved. Now to implicitly solve the PDE all that needs to be done is the system of equations needs to be solved at each time step. In order to solve this system of equations one can make use of the matrices that represent this system. The system can be represented as $Af(t_j, \mu) = f(t_{j-1}, \mu)$, where A is a square matrix with length L, where L is the number of bins in the array $f(t_j, \mu)$. The form of A is shown in equation (28).

$$A = \begin{pmatrix} 1 - \frac{kD\prime_{\mu\mu}(\mu)}{w} + \frac{2kD_{\mu\mu}(\mu)}{w^2} & -\frac{kD_{\mu\mu}(\mu)}{w^2} & 0 & \cdots \\ \frac{kD\prime_{\mu\mu}(\mu)}{w} - \frac{kD_{\mu\mu}(\mu)}{w^2} & 1 - \frac{kD\prime_{\mu\mu}(\mu)}{w} + \frac{2kD_{\mu\mu}(\mu)}{w^2} & \frac{kD_{\mu\mu}(\mu)}{w^2} & \\ 0 & \frac{kD\prime_{\mu\mu}(\mu)}{w} - \frac{kD_{\mu\mu}(\mu)}{w^2} & 1 - \frac{kD\prime_{\mu\mu}(\mu)}{w} + \frac{2kD_{\mu\mu}(\mu)}{w^2} & \ddots \\ \vdots & & \ddots & \ddots \end{pmatrix} \tag{28}$$

It's important to keep in mind that since $D_{\mu\mu}$ is a function of μ it changes across each column of the matrix. The only task left is to find the inverse of this matrix and multiply it by the PDE solution at time t_{j-1} to get the solution at time t_j. When this process is repeated over and over one can obtain the solution to the PDE at any time t. However, neither of these methods were used alone in this work. For the first derivative terms the implicit method was used however for the term with the second derivative an even more stable and complex method than the implicit method was used. A method which combines the techniques of explicit and implicit methods. This is called the Crank-Nicholson method (see Press *et al.* (1989)). It is implemented by taking the sum of both methods and dividing them in half at each time step. An illustration of this method is shown in figure (4).

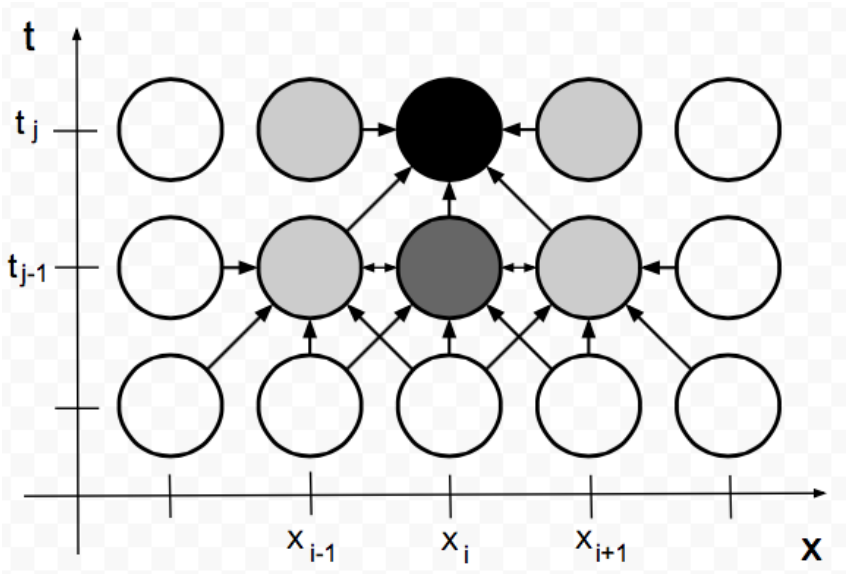

Figure 4: Arrows show the dependencies the value at a point has on the values at other points. The second row shows dependencies for all midpoints (points that are not boundary cases). The top row shows the dependencies that only the black dot has. These points that allow one to solve for the value at the black dot, are coloured gray. The dot coloured darker gray than the rest lends its contribution to the value of the black dot with twice the weight as the other dots.

2.2.3 Working in Higher Dimensions

Solving equation (20) requires one to take this one dimensional process and apply it to a higher dimensional PDE. In order to do this first write out equation (20) and transform it into a form that shows the derivatives in a discrete way as was done in section 2.2.2,

$$\frac{\partial f}{\partial t} = -v\mu\frac{\partial f}{\partial z} + D'_{\mu\mu}(\mu)\frac{\partial f}{\partial \mu} + D_{\mu\mu}(\mu)\frac{\partial^2 f}{\partial \mu^2}. \tag{29}$$

In this section (sec 2.2.3) only an implicit method is discussed in the interest of saving time. This can fairly easily be turned into an explicit or Crank-Nicolson method by applying the process shown in this section (sec 2.2.3) to the methods shown in section 2.2.2. The following shows the discrete form of the full Fokker-Planck equation,

$$\begin{aligned} f(t_j,\mu_i,z_p) - k\Bigg(&- v\mu\frac{f(t_j,\mu_i,z_p) - f(t_j,\mu_i,z_{p-1})}{s} + D'_{\mu\mu}(\mu)\frac{f(t_j,\mu_i,z_p) - f(t_j,\mu_{i-1},z_p)}{w} + \\ &D_{\mu\mu}(\mu)\frac{f(t_j,\mu_{i+1},z_p) - 2f(t_j,\mu_i,z_p) + f(t_j,\mu_{i-1},z_p)}{w^2}\Bigg) = f(t_{j-1},\mu_i,z_p), \end{aligned} \tag{30}$$

where s is the step size in the z dimension, p denotes the bin number in the z dimension, w is again the step size in the μ dimension, and i is again the bin number in the μ dimension. In order to implement this method the two dimensional function $f(t_j,\mu,z)$ must be turned into a one dimensional array. Then the $Af(t_j,\mu,z) = f(t_{j-1},\mu,z)$ matrix method can be implemented. In order to turn the two dimensional function into a one dimensional array one simply strips each column in the two dimensional matrix that

makes up the function and lies them in a row as shown in equation (31).

$$F = \begin{pmatrix} F_{1,1} & F_{1,2} & F_{1,3} \\ F_{2,1} & F_{2,2} & F_{3,3} \\ F_{3,1} & F_{3,2} & F_{3,3} \end{pmatrix} \Rightarrow \begin{pmatrix} F_{1,1} \\ F_{2,1} \\ F_{3,1} \\ F_{1,2} \\ F_{2,2} \\ F_{3,2} \\ F_{1,3} \\ F_{2,3} \\ F_{3,3} \end{pmatrix}, \tag{31}$$

where F is the two dimensional matrix or one dimensional array that represents the discrete function that is contained in the code. The columns of F in its matrix form are the function f where z is held constant and the rows of F in its matrix form are the function f where μ is held constant. This means that one can take the matrix A that was shown in section 2.2.2 as equation (28), and modify it to include the z derivative. This modified matrix is then used as a sub matrix in the new matrix A (shown in equation (32)). This is required in order to solve the three dimensional function $f(t, \mu, z)$. Each sub matrix is arranged along the main diagonal in the matrix,

$$A = \begin{pmatrix} \begin{pmatrix} A_1 \end{pmatrix} & & 0 \\ & \begin{pmatrix} A_2 \end{pmatrix} & \\ 0 & & \begin{pmatrix} A_3 \end{pmatrix} \end{pmatrix}, \tag{32}$$

where all elements which are not in the sub-matrices, A_i, are 0. Each sub-matrix will have non-zero matrix elements in the same places that are shown in equation (28) with the following exceptions,

$$A_{maindiag} = 1 + \frac{kv\mu}{s} - \frac{kD\prime_{\mu\mu}(\mu)}{w} + \frac{2kD_{\mu\mu}(\mu)}{w^2}, \tag{33}$$

$$A_{abovediag} = 1 + \frac{kv\mu}{s} - \frac{kD_{\mu\mu}(\mu)}{w^2}, \tag{34}$$

$$A_{belowdiag} = 1 + \frac{kv\mu}{s} + \frac{kD\prime_{\mu\mu}(\mu)}{w} - \frac{kD_{\mu\mu}(\mu)}{w^2}, \tag{35}$$

and

$$A_{offsetdiag} = -\frac{kv\mu}{s}. \tag{36}$$

The matrix elements along the main diagonal are as shown in equation (33). The elements adjacently above the main diagonal are shown in equation (34). The elements adjacently below the main diagonal are shown in equation (35). There are also now non-zero elements which are in a diagonal that is offset from the main diagonal by the number of steps in the μ dimension. These non-zero elements correspond to the $p-1$ part of the differencing in the z dimension and are shown in equation (36). All that is left is to implement the boundary conditions and solve for $f(t, \mu, z)$ in the following equation, $Af(t_j, \mu, z) = f(t_{j-1}, \mu, z)$, and then the full three dimensional PDE can be solved. The boundary conditions for μ were discussed in section 2.2.2. In the z dimension the boundary conditions are more simple. The boundary conditions in z are simply that the function is equal to zero at $z = \pm\infty$ which allows for hard values to be set in the outside bins. This removes the two extra unknown variables that would be needed to determine the solution to the set of linear equations that need to be solve at each time step. It can be noted that of course the z axis will not extend to $\pm\infty$ but one can employ a transform to to extend the coordinate system to be long enough that the function will not propagate far

enough to reach the boundaries. This is discussed in more detail at the end of this subsubsection. Our varibales must be dimensionaless for numerical work, therefore the following transformations are made,

$$\tau = Dt, \tag{37}$$

$$\tilde{z} = \frac{zD}{v}. \tag{38}$$

The equation with these new variables becomes

$$\frac{\partial f}{\partial \tau} = -\mu \frac{\partial f}{\partial \tilde{z}} + \frac{\partial}{\partial \mu}\left[\frac{D_{\mu\mu}(\mu)}{D}\frac{\partial f}{\partial \mu}\right]. \tag{39}$$

The numerical code solves this equation which is not explicitly dependent on the values of v and D. This solution can then be transformed back to the original form if values of these variables are determined and need to be used in other work. One final transformation that was used in the numerical code but then transformed back in order to find properties of the solution was a transform created in order to improve two aspects of the solution. The transform

$$\theta = 10\frac{|\tilde{z}|}{\tilde{z}}(e^{|\tilde{z}|} - 1), \tag{40}$$

compresses the original z axis to include finer detail about $z = 0$ and stretches the axis near the boundaries so that the propagation of $f(\tilde{z}, \mu, \tau)$ takes far longer to reach the edges of the numerical grid. The finer detail for small values of $\tilde{z}$ helps the code deal with what can become instability issues due to the sharp initial conditions of the function. The function naturally becomes less sharp as it reaches larger values of $\tilde{z}$, so the the fine detail is not needed there. Also there is an issue where the boundary conditions of $\tilde{z}$ are only actually valid at $\tilde{z} = \pm\infty$, so by stretching the axis out at higher values one can ensure the function never propagates to the boundaries and the condition is therefore satisfied by the nature of the transform alone. The function (40) is shown in figure (5). Areas with a slope less than 1 correspond to a compressed portion of the axis with finer detail that the function moves quickly through, areas with a slope greater than 1 correspond to a stretched out portion of the axis with less detail which the function takes longer to propagate through. The further away the slope is from 1 the greater the effect.

The last detail to add is that since in analytic work the initial condition of the solution to the Fokker-Planck equation is usually a Dirac-delta both in μ and z, in the numerical solution the initial condition used is a sharp peaked Gaussian function. Specifically in analytic work

$$f(t = 0, \mu, z) = \delta(\mu - \mu_0)\delta(z), \tag{41}$$

and in the numerical work the initial function

$$f(t = 0, \mu, z) = exp\left(-\left(\frac{\theta^2}{2\sigma_\theta^2} + \frac{(\mu - \mu_0)^2}{2\sigma_\mu^2}\right)\right) \tag{42}$$

was used. Here the values of the standard deviations σ_μ and σ_θ were each a function of the size of the grid used. Specifically

$$\sigma_\mu = 0.05(\mu_{max} - \mu_{min}) = 0.1, \tag{43}$$

and

$$\sigma_\theta = 0.05(z_{max} - z_{min}) = 0.08. \tag{44}$$

Figures (6) - (10) are some resultant plots of the numerical solution to $f(t, \mu, z)$ using $D_{\mu\mu} = D(1 - \mu^2)$ which is the isotropic form of $D_{\mu\mu}$. The isotropic form of $D_{\mu\mu}$ is a common and simple form of the the scattering coefficient. We use it in this analytic work because of its simplicity (see Shalchi *et al.* (2009) for a justification of the isotropic form). These figures also use an initial pitch angle cosine of $\mu_0 = 0.5$.

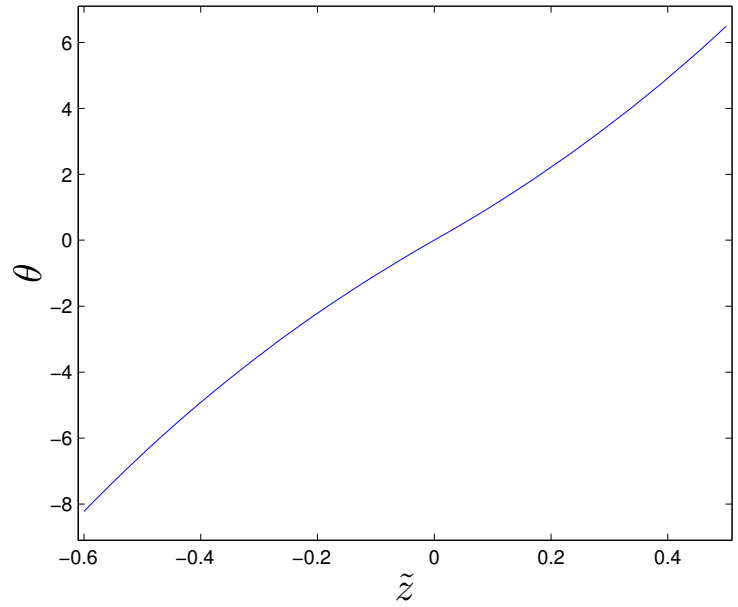

Figure 5: Shown is equation (40), the transformation function which allows for better numerical accuracy at positions on the z axis where the solution is significant.

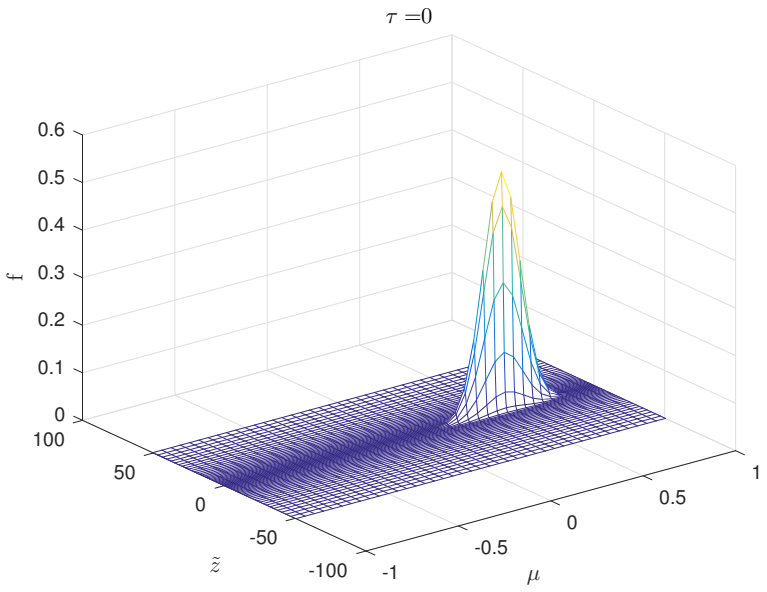

Figure 6: The numerical solution to equation (20) for a time $\tau = tD = 0$. This is the initial distribution.

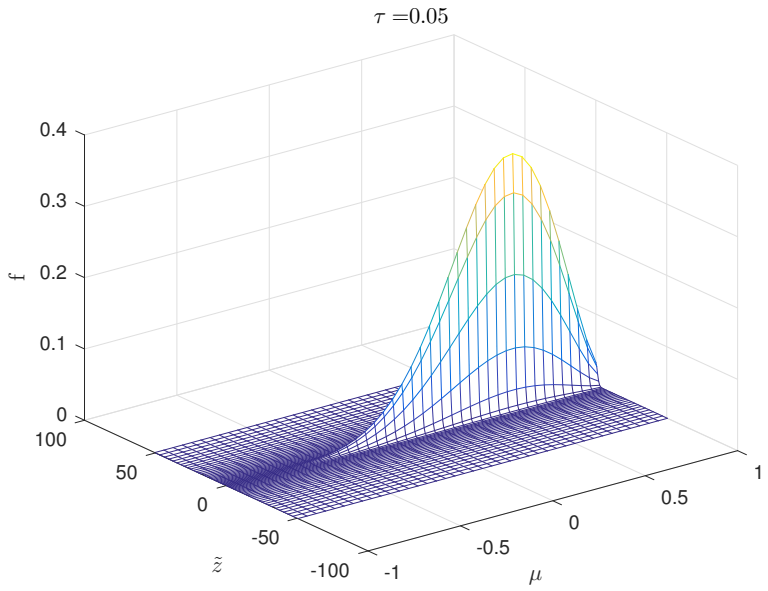

Figure 7: The numerical solution to equation (20) for a time $\tau = tD = 0.05$. This is how the solution propagates at very early times.

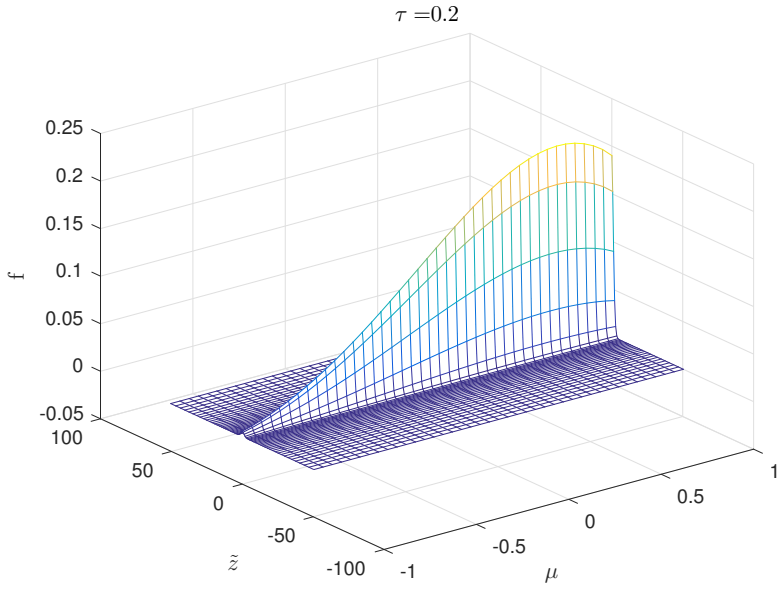

Figure 8: The numerical solution to equation (20) for a time $\tau = tD = 0.2$. This is how the solution propagates at very early times.

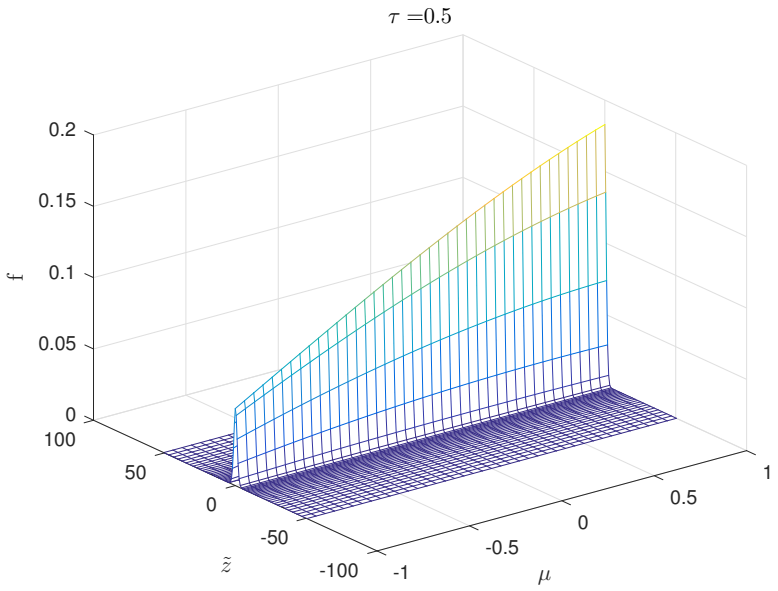

Figure 9: The numerical solution to equation (20) for a time $\tau = tD = 0.5$. This is the solution at what is called a non-isotropic time, because the solution is still a function of pitch angle.

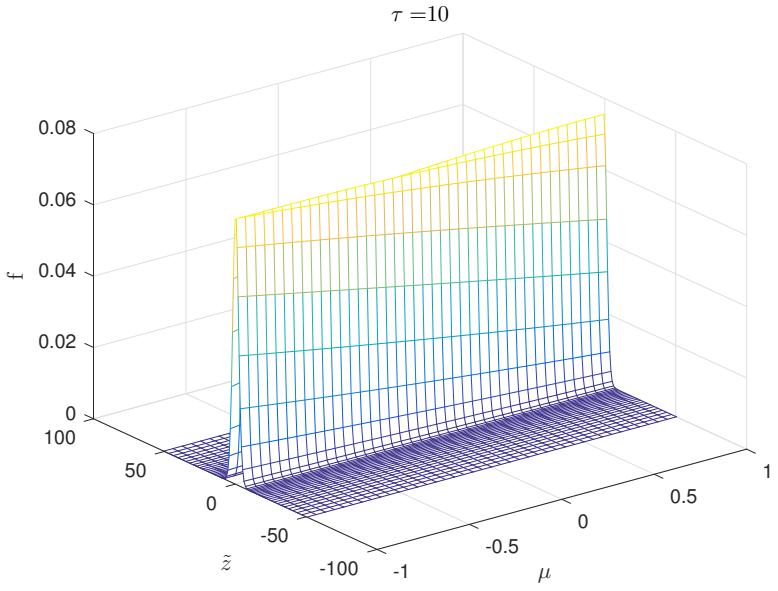

Figure 10: The numerical solution to equation (20) for a time $\tau = tD = 10$. This is the late time solution where there is no longer any pitch angle dependency.

2.2.4 Numerical Integration

In order to find some characteristics of the solution, expectation values of certain quantities need to be found. The expectation value of x can be defined as follows,

$$< x >= \frac{1}{2}\int_{-1}^{1} d\mu \int_{-\infty}^{\infty} dz\; x f(t,\mu,z). \tag{45}$$

In order to find these expectation values the solution $f(t,\mu,z)$ must be integrated numerically. Just like differentiation there are multiple methods of integrating functions numerically. First the trapezoidal integration method is discussed and then after Simpson's rule is discussed. Simpson's rule is a more complicated method and is the method which was implemented in the code (see Press *et al.* (1989)). The trapezoidal integration method is simple to understand with a diagram. Figure (11) shows how the area under the curve can be divided into discrete trapezoids which can then have their area's summed to find the total area under the curve. This method can be described by the following simple equation,

$$\int_a^b dx f(x) = \frac{(b-a)}{2}\Big(f(x=a) + f(x=b)\Big). \tag{46}$$

This comes from taking the general function f and writing it as a first-order Lagrange polynomial. This equation should be obvious when observing the problem from a geometric standpoint.

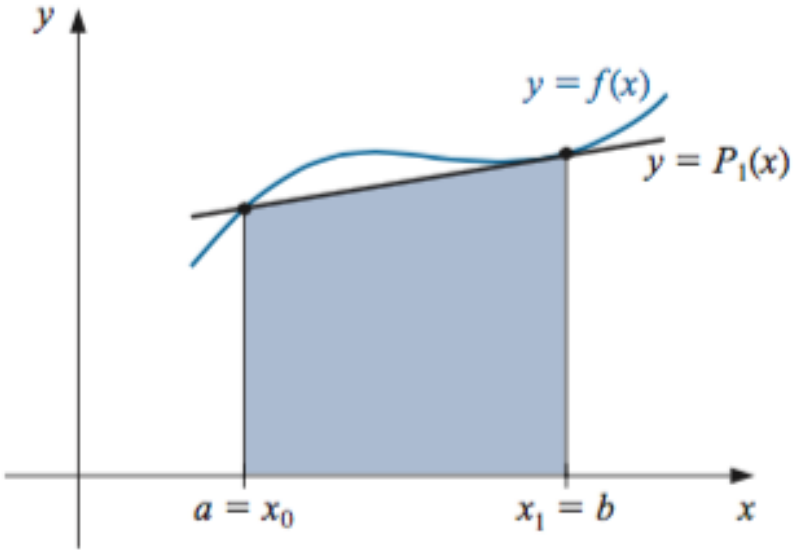

Figure 11: Figure from Burden & Faires (1993). Shown is the trapezoidal area that is created and integrated with the first method described in section 2.2.4. In a real integration the integration is broken up into many small trapezoid areas such as this one and then summed together.

By making the difference between a and b very small and summing a series of these integrals together a fair approximation of the area under a curve can be numerically determined. However this method is only a first-order approximation and will have difficulty with curves that are more varied as well as with situations where one cannot make the step size, $b-a$, very small. Simpson's rule is a second-order method of calculating an integral numerically. By expressing the general function as a Taylor expansion, taken to fourth order, one can derive the following equation,

$$\int_a^b dx f(x) = \frac{b-a}{3}(f(x=a) + 4f(x=b) + f(x=c)), \tag{47}$$

where b is the point directly in between points a and c. This models the discrete areas under the curve as the area under a second degree polynomial. Instead of simply summing a string of small integrals to get a larger area under the curve, in this case the integral is taken at each point b along the function then one must account for the overlap that occurs from this by taking the weight of each point b that is in the middle of the curve to be half a unit weight and the weight of each point b that is at second from the end of the curve as one unit weight. The points at the very edges of the function of course cannot be modeled by this because it requires points on both sides of the point b in order to compute, instead a trapezoidal method can be applied at the boundary. Alternatively at the boundary one can create ghost zones that approximate what the curve might reasonably be past the edge and use those. The code written for thus work implements the ghost zones method and is expanded to have the capability of integrating multiple dimensions at once up to a maximum of 10 dimensions.

2.3 Modeling the Scattering Coefficient

The parameter $D_{\mu\mu}$ is difficult to model accurately. Although there is a commonly used formulation where $D_{\mu\mu}$ is modeled as (see Kubo (1957)),

$$D_{\mu\mu} = \int_0^\infty dt < \dot{\mu}(t)\dot{\mu}(0) > . \tag{48}$$

Employing a second order quasi-linear approximation, along with the assumption that $|\mu| \leq \delta B/B_0$ this was shown in Shalchi (2009) to lead to the following,

$$D_{\mu\mu} = \frac{\pi D(s,q)}{2sl_{slab}}(1-\mu^2)R^{s-2}\frac{\delta B}{B_0}\left[\left(|\mu| + \frac{\delta B}{B_0}\right)^s + \left(\frac{\delta B}{B_0} - |\mu|\right)^s\right], \tag{49}$$

where $D(s,q)$ is a function that is independent of μ, s is the inertial range spectral index, l_{slab} is the slab bendover scale (which is the characteristic length scale for the spatial decorrelation of slab turbulence), $\delta B/B_0$ corresponds to the ration of the turbulence strength of the magnetic field to the strength of the mean magnetic field, R is a dimensionless rigidity which is equal to the Larmor radius divided by the slab bendover scale. When $|\mu| \ll \delta B/B_0$, Shalchi shows that equation (49) reduces to (see Lasuik *et al.* (2016)),

$$D_{\mu\mu} = (1-\mu^2)DB^{s+1}. \tag{50}$$

The condition $|\mu| \ll \delta B/B_0$, is usually satisfied in the strong turbulent regimes of these systems because $|\mu|$ is always less than 1 due to it being a cosine function. In this work the constant B^{s+1} has been absorbed into the other constant to make the model more simple. It is therefore just some constant, D, times some function of μ, $(1-\mu^2)$. The other models chosen are based mostly on the idea that they are similar functions to the isotropic one, and that they might make analytic solutions to the equation possible. Their chance of having an analytic solution is of utmost importance. Therefore the models examined are as follows:

$$D_{\mu\mu} = D \quad Constant\ Form \tag{51}$$

$$D_{\mu\mu} = D(1-\mu^2) \quad Isotropic\ Form \tag{52}$$

$$D_{\mu\mu} = D(1-|\mu|) \quad Linear\ Form \tag{53}$$

$$D_{\mu\mu} = D|\mu|(1-|\mu|) \quad Quasi-Linear\ Form \tag{54}$$

These forms are plotted in figure (12).

For each model of the scattering coefficient numerical solutions were found to the more general, z-dependent, Fokker-Planck equation (20). The solutions to the Fokker-Planck equation using the isotropic model (52) were previously shown in figures (6), (7), (9), and (10). The solutions using the constant $D_{\mu\mu}$ model (51) are shown in figures (13), (14), (15), and (16). The solutions to the Fokker-Planck

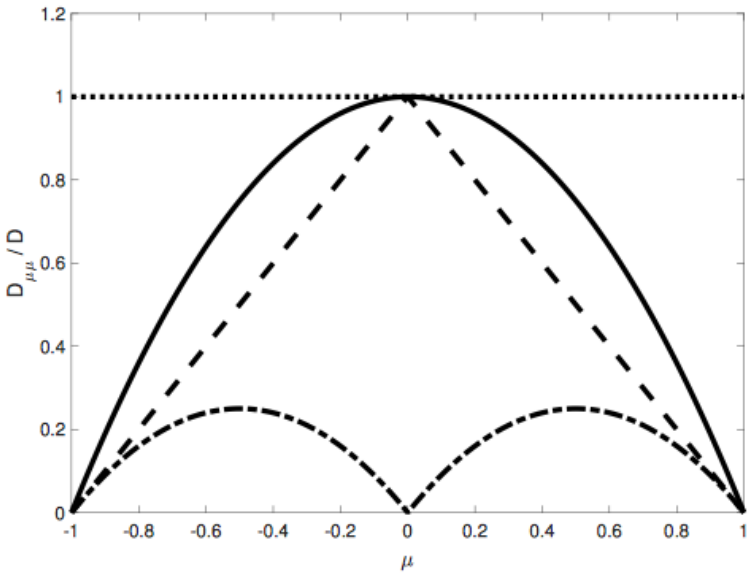

Figure 12: A plot of equations (51)-(54), normalized with respect to the constant D. The dotted line is the constant $D_{\mu\mu}$. The solid line is the isotropic $D_{\mu\mu}$. The dashed line is the linear $D_{\mu\mu}$. The dashed-dotted line is the quasi-linear $D_{\mu\mu}$.

equation using the linear $D_{\mu\mu}$ (53) are shown in figures (17), (18), (19), and (20). The solutions to the Fokker-Planck equation using the quasi-linear $D_{\mu\mu}$ (54) are shown in figures (21), (22), (23), and (24).

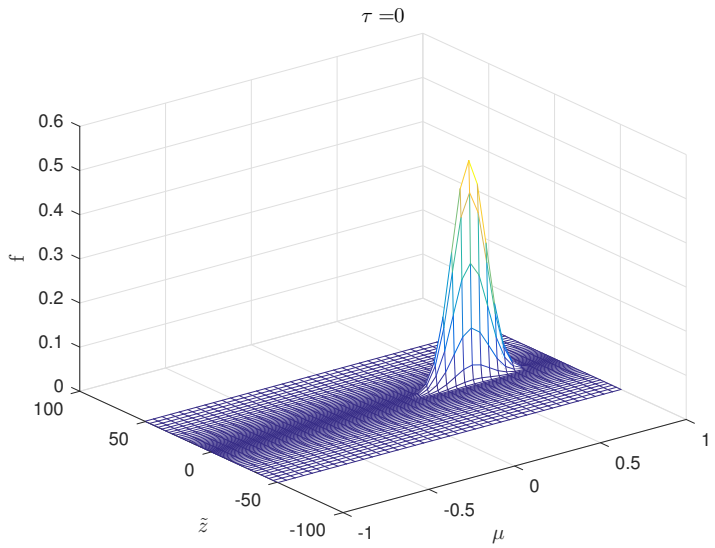

Figure 13: The numerical solution to equation (20) for a time $\tau = tD = 0$. Using the constant $D_{\mu\mu}$ (51), and an initial pitch angle cosine $\mu_0 = 0.5$. This is the initial distribution.

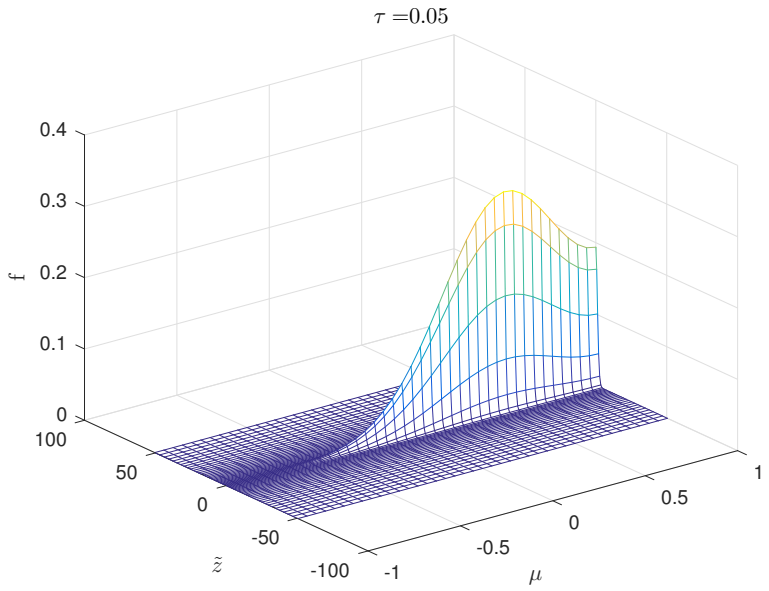

Figure 14: The numerical solution to equation (20) for a time $\tau = tD = 0.05$. Using the constant form of $D_{\mu\mu}$ (51), and an initial pitch angle cosine, $\mu_0 = 0.5$. This is how the solution propagates at very early times.

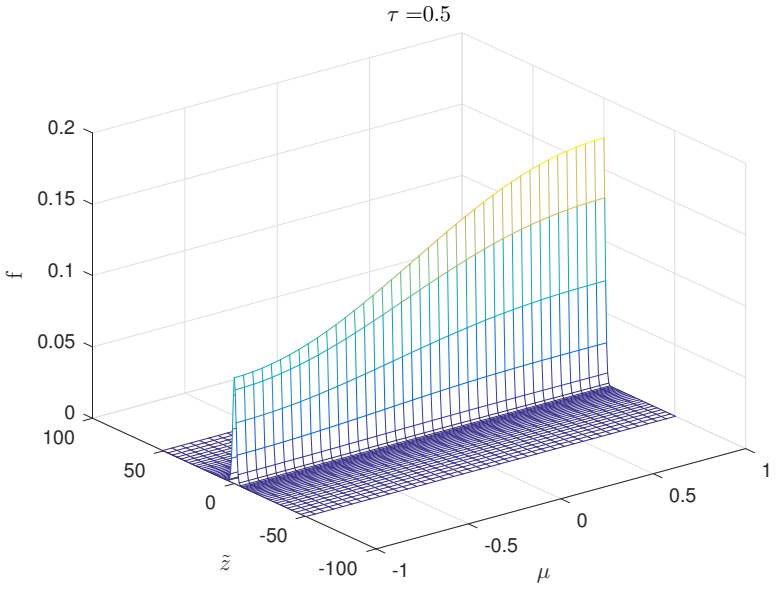

Figure 15: The numerical solution to equation (20) for a time $\tau = tD = 0.5$. Using the constant $D_{\mu\mu}$ (51), and an initial pitch angle cosine $\mu_0 = 0.5$. This is the solution at what is called a non-isotropic time, because the solution is still a function of pitch angle.

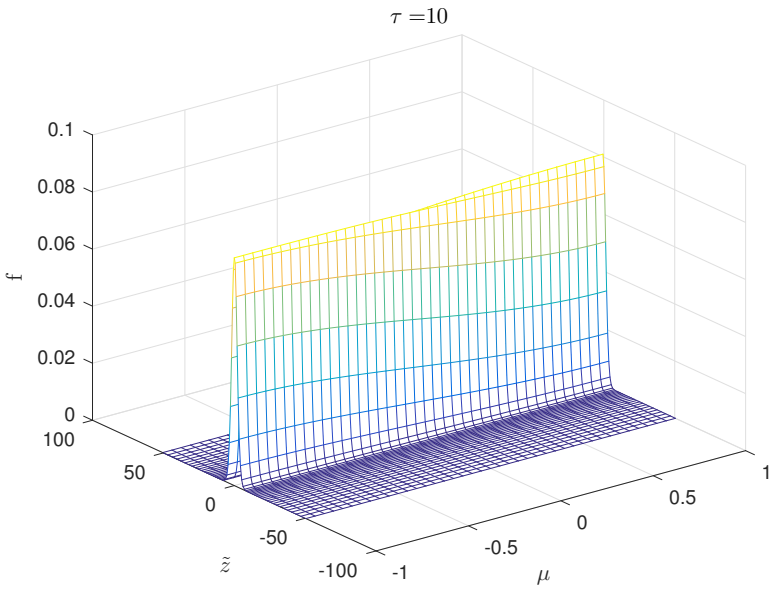

Figure 16: The numerical solution to equation (20) for a time $\tau = tD = 10$. Using the constant $D_{\mu\mu}$ (51), and an initial pitch angle cosine, $\mu_0 = 0.5$. This is the late time solution where there is no longer any pitch angle dependency.

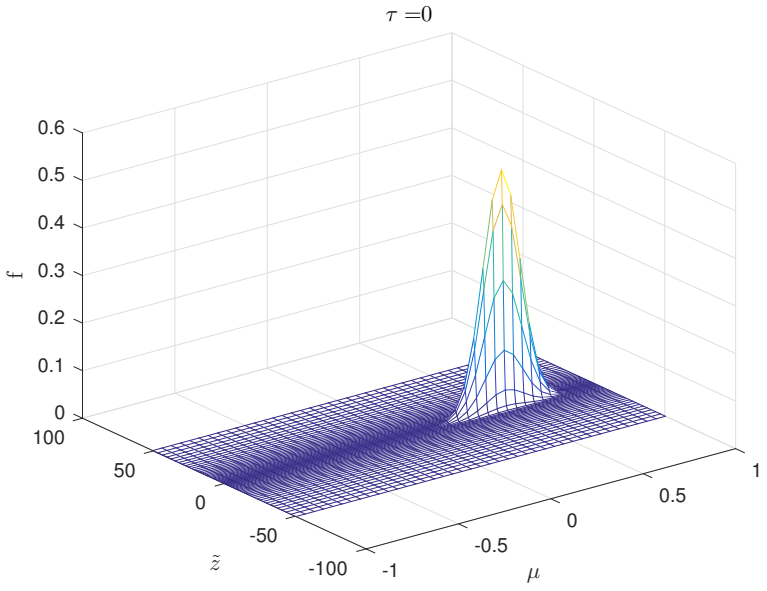

Figure 17: The numerical solution to equation (20) for a time $\tau = tD = 0$. Using the linear $D_{\mu\mu}$ (53), and an initial pitch angle cosine, $\mu_0 = 0.5$. This is the initial distribution.

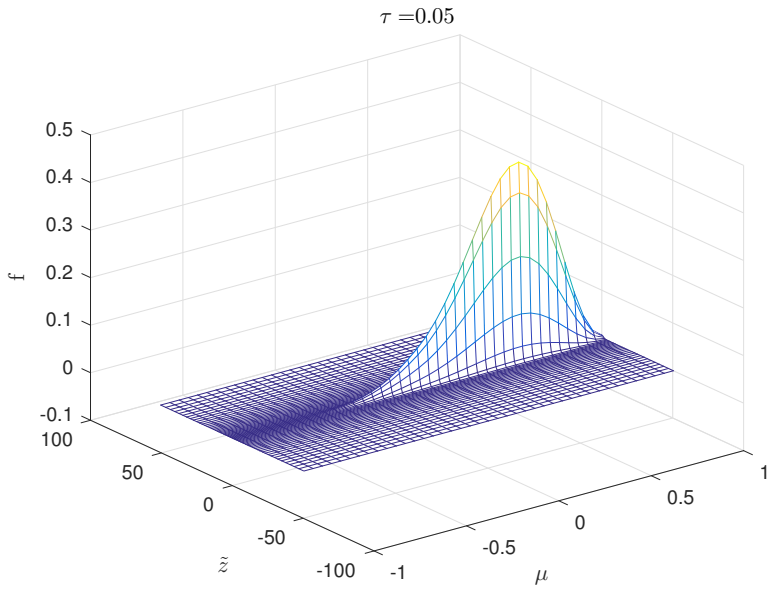

Figure 18: The numerical solution to equation (20) for a time $\tau = tD = 0.05$. Using the linear $D_{\mu\mu}$ (53), and an initial pitch angle cosine, $\mu_0 = 0.5$. This is how the solution propagates at very early times.

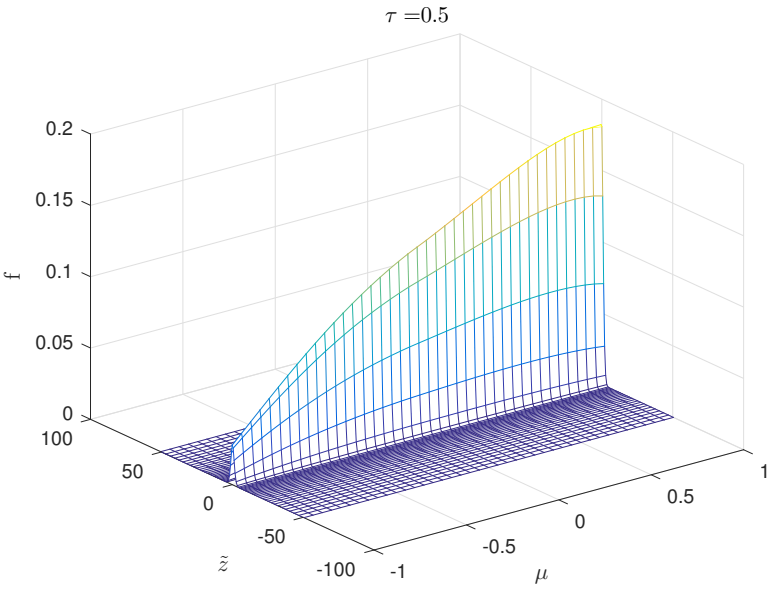

Figure 19: The numerical solution to equation (20) for a time $\tau = tD = 0.5$. Using the linear $D_{\mu\mu}$ (53), and an initial pitch angle cosine, $\mu_0 = 0.5$. This is the solution at what is called a non-isotropic time, because the solution is still a function of pitch angle.

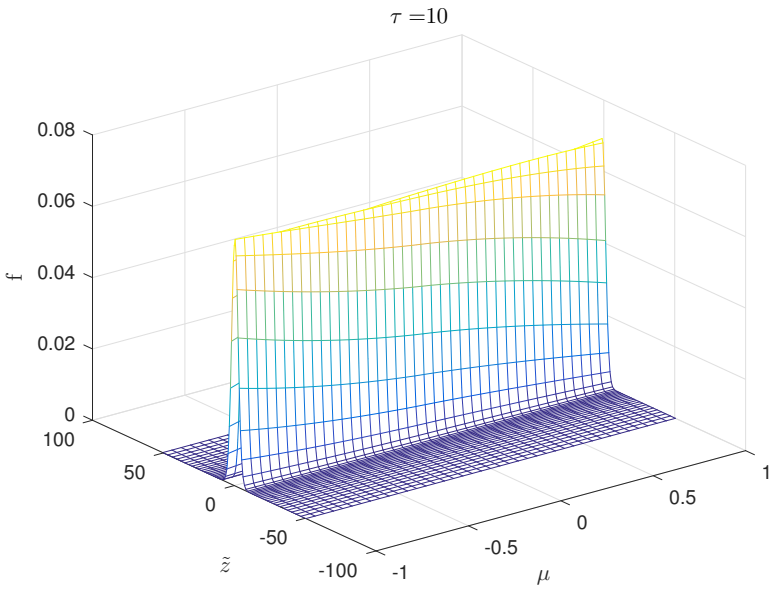

Figure 20: The numerical solution to equation (20) for a time $\tau = tD = 10$. Using the linear $D_{\mu\mu}$ (53), and an initial pitch angle cosine, $\mu_0 = 0.5$. This is the late time solution where there is no longer any pitch angle dependency.

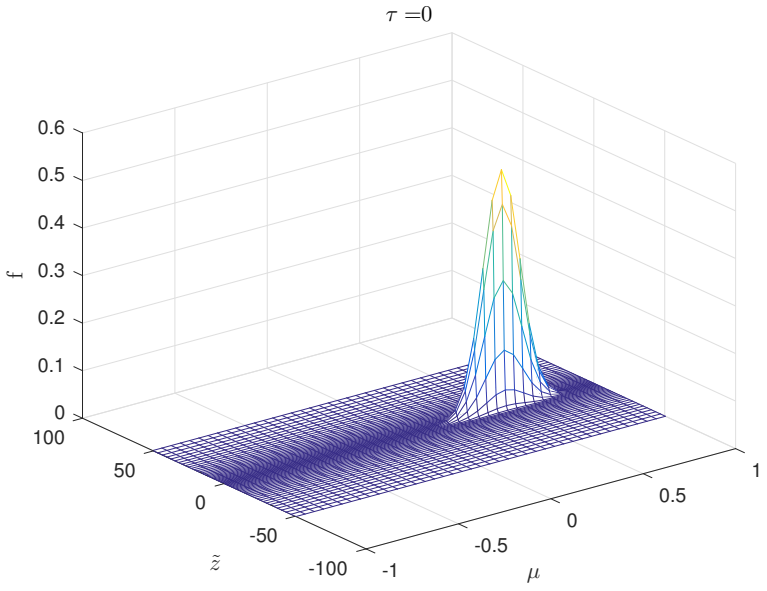

Figure 21: The numerical solution to equation (20) for a time $\tau = tD = 0$. Using the quasi-linear $D_{\mu\mu}$ (54), and an initial pitch angle cosine, $\mu_0 = 0.5$. This is the initial condition.

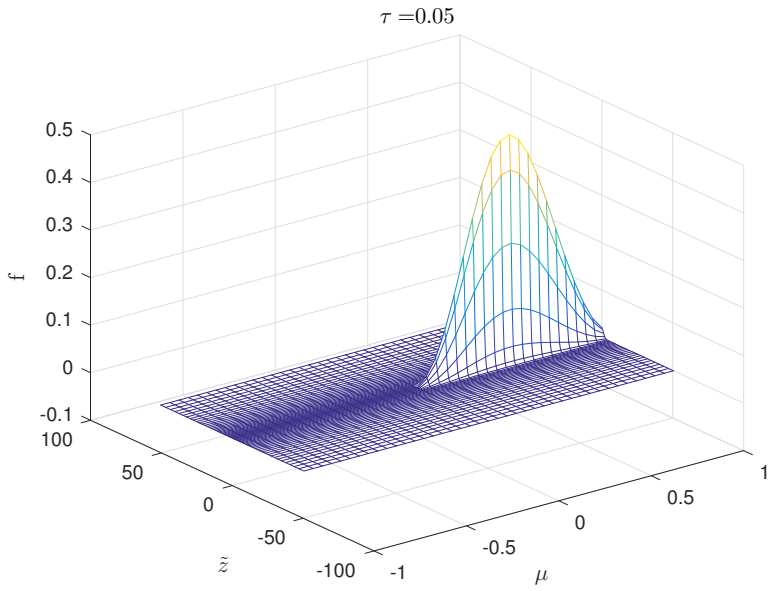

Figure 22: The numerical solution to equation (20) for a time $\tau = tD = 0.05$. Using the quasi-linear $D_{\mu\mu}$ (54), and an initial pitch angle cosine, $\mu_0 = 0.5$. This is how the solution propagates at very early times.

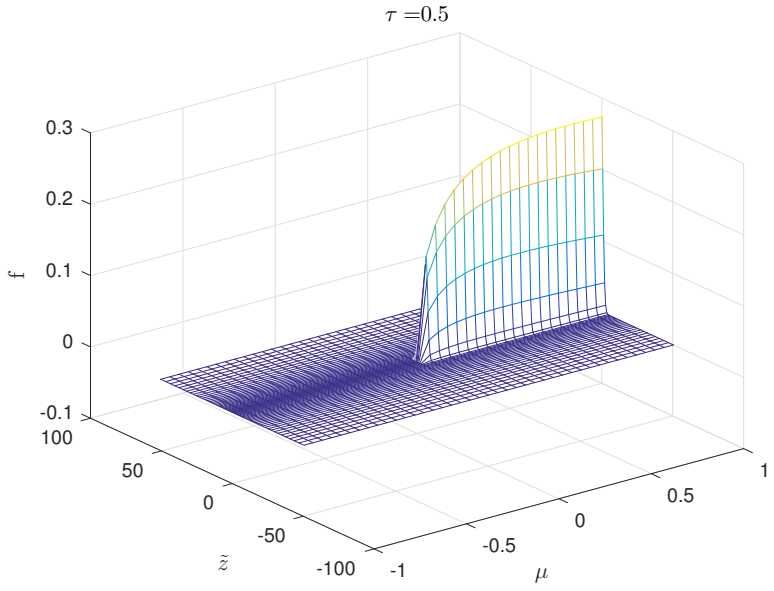

Figure 23: The numerical solution to equation (20) for a time $\tau = tD = 0.5$. Using the quasi-linear $D_{\mu\mu}$ (54), and an initial pitch angle cosine, $\mu_0 = 0.5$. This is the solution at what is called a non-isotropic time, because the solution is still a function of pitch angle.

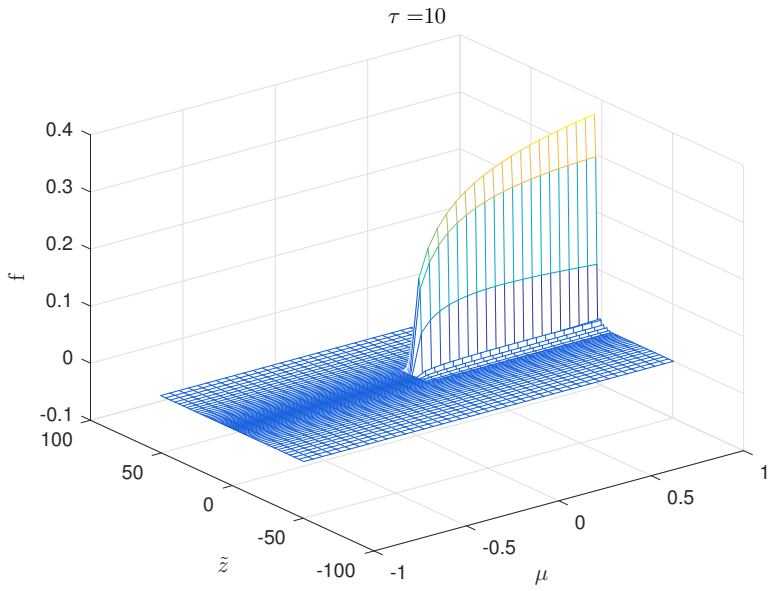

Figure 24: The numerical solution to equation (20) for a time $\tau = tD = 10$. Using the quasi-linear $D_{\mu\mu}$ (54), and an initial pitch angle cosine, $\mu_0 = 0.5$. This is the late time solution where there is no longer any pitch angle dependency. It is obvious that due to the nature of this model that, no matter how long one waits, the solution cannot propagate past $\mu = 0$. Therefore all the particles will have a pitch angle between either -1 and 0, or between 0 and 1, depending on the initial pitch angle.

2.4 Comparing Analytic and Numerical Solutions

Analytic solutions to the one dimensional Fokker-Planck equation (24) were found by Dr. Shalchi for all four of the $D_{\mu\mu}$ models (see Lasuik & Shalchi (2017)). The solution for the constant $D_{\mu\mu}$ is

$$\begin{aligned} F(\mu,t) &= 1 + 2\sum_{n=0}^{\infty} cos(\pi n\mu_0)cos(\pi n\mu)e^{-(\pi n)^2 Dt} \\ &+ 2\sum_{n=0}^{\infty} sin(\pi(n+1/2)\mu_0)sin(\pi(n+1/2)\mu)e^{-(\pi(n+1/2))^2 Dt}. \end{aligned} \tag{55}$$

The solution for the isotropic $D_{\mu\mu}$ is

$$F(\mu,t) = 1 + \sum_{n=1}^{\infty}(2n+1)P_n(\mu_0)P_n(\mu)e^{-n(n+1)Dt}, \tag{56}$$

where P_n is a Legendre polynomial. The solution for the linear $D_{\mu\mu}$ is

$$\begin{aligned} F(\mu,t) &= 1 + \sum_{n=1}^{\infty} \frac{J_0(z_n\sqrt{1-\mu_0})J_0(z_n\sqrt{1-\mu})}{J_0^2(z_n)} e^{-\frac{1}{4}z_n^2 Dt} + \\ &\frac{\mu_0\mu}{|\mu_0||\mu|}\sum_{n=1}^{\infty} \frac{J_0(y_n\sqrt{1-\mu_0})J_0(y_n\sqrt{1-\mu})}{J_1^2(y_n)} e^{-\frac{1}{4}y_n^2 Dt}, \end{aligned} \tag{57}$$

where y_n are the zeros to the Bessel function J_0, and z_n are the zeros to the Bessel function J_1. The solution for the quasi-linear $D_{\mu\mu}$ is

$$F^{\pm}(\mu,t) = 2\Theta(\pm\mu_0)\sum_{n=0}^{\infty}(2n+1)P_n(x_0 = 1 \mp 2\mu_0)P_n(x = 1 \mp 2\mu)e^{-n(n+1)Dt}, \tag{58}$$

where $F^{+}(\mu,t)$ is used for positive values of μ and $F^{-}(\mu,t)$ is used for negative values of μ, and P is a Legendre Polynomial.

For each of these models the more general Fokker-Planck equation (20) was solved numerically and then integrated over the z dimension to check the analytic solutions listed above. The integration was done via the Simpson method multi-dimensional integrator mentioned in section (2.2.4). These solutions are plotted for different values of τ in figures (25) - (28). As mentioned earlier the initial conditions of the numerical solutions are Gaussian functions rather than the Dirac-delta distribution which are the initial conditions for the analytic solutions. This is a constraint on the discrete nature of the numerical solution, and is the reason for the discrepancy in early τ value solutions. The solutions converge at later values of τ where the solution is not as dependant on the initial conditions. This shows that the particles, over time, lose all information about their initial conditions.

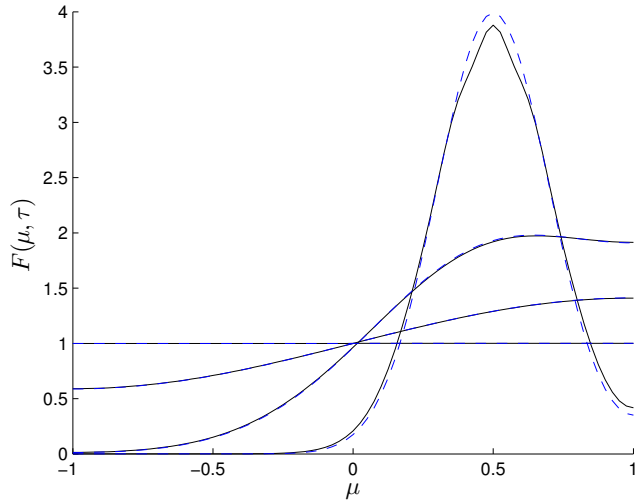

Figure 25: The analytic solutions to the z-averaged Fokker-Planck equation with a **constant** $D_{\mu\mu}$ (shown in equation (51)) is plotted as a blue dashed line. The numerical solutions to the Fokker-Planck equation with the same $D_{\mu\mu}$ then integrated over z is plotted as the solid black line. The plotted functions are at values of τ equal to 0.01, 0.1, 0.5, and 3. The later τ values correspond to a flatter function approaching a constant value.

To see the difference in these models better, and to show what the solutions to equation (24) look like, figures (29) - (32) show the numerical solutions to (24) of each model plotted against each other at varying times. These figures show that the linear model has solutions which are most similar to the isotropic model. This means that since the isotropic model is accepted as a good model, perhaps the linear model is nearly as good a model. Therefore there is reason to believe that further analytic work with the linear model may be a useful line of research. These figures also show that the solution of the quasi-linear model solution is an outlier to the others. It is certainly the most different from the isotropic model. It can be concluded then that further work with this model may not be of particular use.

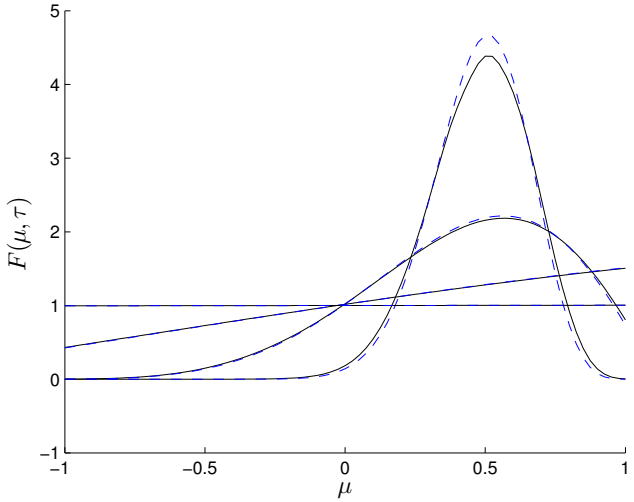

Figure 26: The analytic solutions to the z-averaged Fokker-Planck equation with an **isotropic** $D_{\mu\mu}$ (shown in equation (52)) is plotted as a blue dashed line. The numerical solutions to the Fokker-Planck equation with the same $D_{\mu\mu}$ then integrated over z is plotted as the solid black line. The plotted functions are at values of τ equal to 0.01, 0.1, 0.5, and 3. The later τ values correspond to a flatter function approaching a constant value.

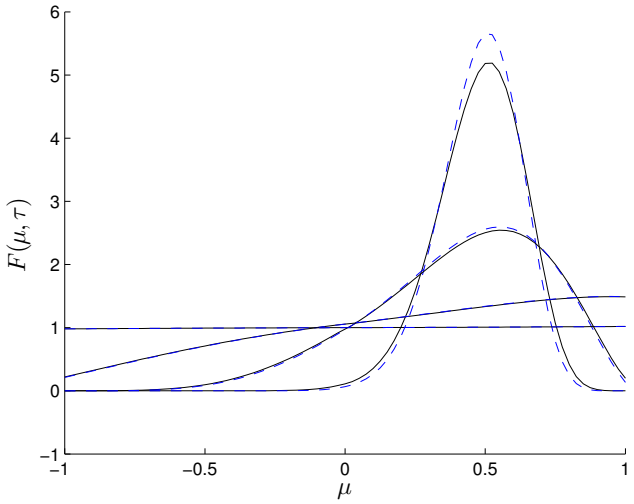

Figure 27: The analytic solutions to the z-averaged Fokker-Planck equation with a **linear** $D_{\mu\mu}$ (shown in equation (53)) is plotted as a blue dashed line. The numerical solutions to the Fokker-Planck equation with the same $D_{\mu\mu}$ then integrated over z is plotted as the solid black line. The plotted functions are at values of τ equal to 0.01, 0.1, 0.5, and 3. The later τ values correspond to a flatter function approaching a constant value.

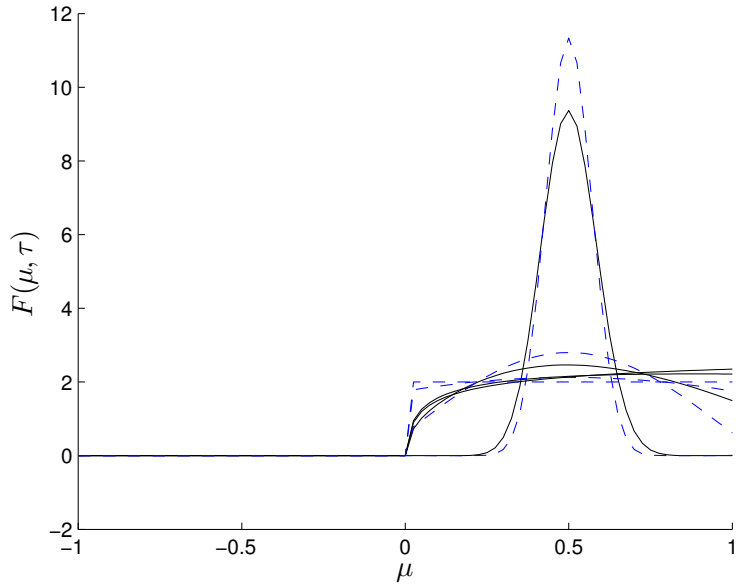

Figure 28: The analytic solutions to the z-averaged Fokker-Planck equation with a **quasi-linear** $D_{\mu\mu}$ (shown in equation (54)) is plotted as a blue dashed line. The numerical solutions to the Fokker-Planck equation with the same $D_{\mu\mu}$ then integrated over z is plotted as the solid black line. The plotted functions are at values of τ equal to 0.01, 0.1, 0.5, and 3. The later τ values correspond to a flatter function approaching a constant value.

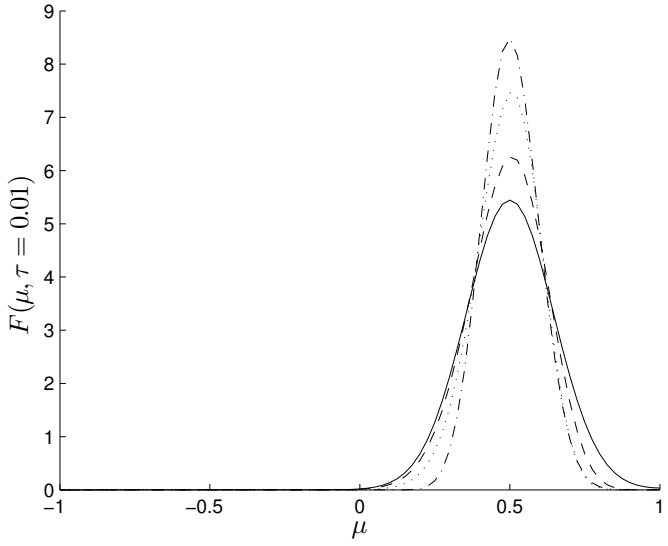

Figure 29: The numerical solutions to the Fokker-Planck equation then integrated over z is plotted for each $D_{\mu\mu}$ type at a $\tau = 0.01$. The solid line is the solution with the constant $D_{\mu\mu}$, the dashed line is the solution with the isotropic $D_{\mu\mu}$, the dotted line is the solution with the linear $D_{\mu\mu}$, and the dashed-dotted line is the solution with the quasi-linear $D_{\mu\mu}$.

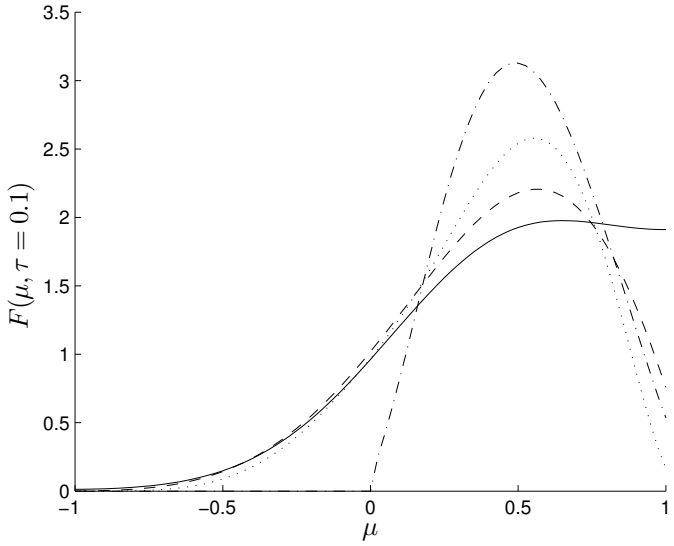

Figure 30: The numerical solutions to the Fokker-Planck equation then integrated over z is plotted for each $D_{\mu\mu}$ type at a $\tau = 0.1$. The solid line is the solution with the constant $D_{\mu\mu}$, the dashed line is the solution with the isotropic $D_{\mu\mu}$, the dotted line is the solution with the linear $D_{\mu\mu}$, and the dashed-dotted line is the solution with the quasi-linear $D_{\mu\mu}$.

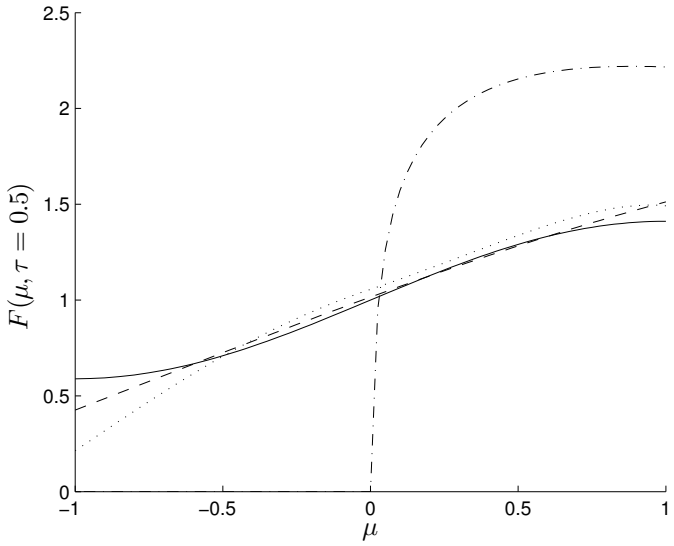

Figure 31: The numerical solutions to the Fokker-Planck equation then integrated over z is plotted for each $D_{\mu\mu}$ type at a $\tau = 0.5$. The solid line is the solution with the constant $D_{\mu\mu}$, the dashed line is the solution with the isotropic $D_{\mu\mu}$, the dotted line is the solution with the linear $D_{\mu\mu}$, and the dashed-dotted line is the solution with the quasi-linear $D_{\mu\mu}$.

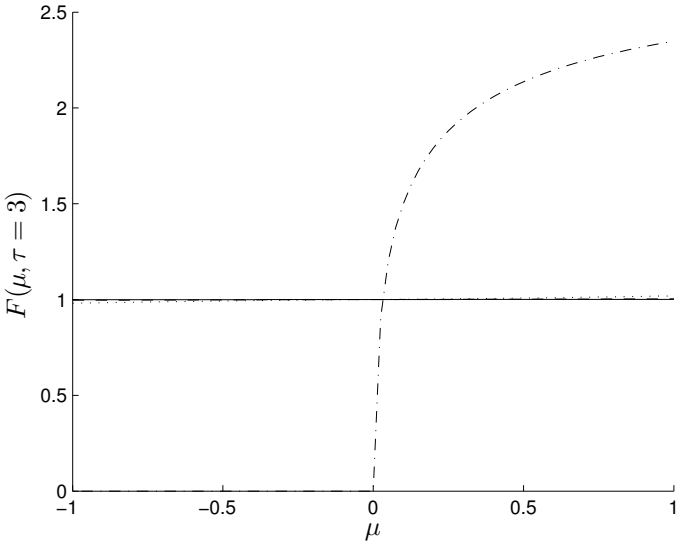

Figure 32: The numerical solutions to the Fokker-Planck equation then integrated over z is plotted for each $D_{\mu\mu}$ type at a $\tau = 3$. The solid line is the solution with the constant $D_{\mu\mu}$, the dashed line is the solution with the isotropic $D_{\mu\mu}$, the dotted line is the solution with the linear $D_{\mu\mu}$, and the dashed-dotted line is the solution with the quasi-linear $D_{\mu\mu}$.

2.5 Comparing Properties of Numerical Solutions

To compare the solutions with different $D_{\mu\mu}$ models to each other one must not only look at the solutions themselves but, even more importantly, their properties. One important quantity in cosmic ray diffusion theory is the velocity correlation function (VCF),

$$< v_0 v(t) >= \frac{v^2}{4} \int_{-1}^{1} d\mu_0 \int_{-1}^{1} d\mu \, \mu_0 \mu F(\mu, t), \tag{59}$$

where $F(\mu, t)$ is the z averaged solution to the Fokker-Planck equation. This is an important part of analyzing diffusion perpendicular to the magnetic field (see Matthaeus *et al.* (2003)). Figure (33) shows the comparison of the velocity correlation functions for each model of the scattering coefficient mentioned in subsection 2.3. These were each calculated by numerically considering the integral (59) using the numerical solutions to equation (20) for each model.

Another important property is the running diffusion coefficient mentioned briefly in subsection 1.7,

$$d_{zz} = \frac{1}{2} \frac{d}{dt} < (\Delta z)^2 > . \tag{60}$$

The late time limit of it is of particular interest. The late time limit of equation (60) is usually referred to as the parallel diffusion coefficient. This is a quantity that is actually measurable. Data can be plotted to these models, allowing determinations of their accuracy. This is done in Bieber *et al.* (1994), and it is shown that there are currently discrepancies between the curves predicted by the theory and the actual data curves. Determining this diffusion coefficient for different models of $D_{\mu\mu}$ gives some insight into this. Figure (34) shows the comparison of the running diffusion coefficients for each model of the scattering coefficient mentioned in subsection 2.3. These were each calculated by numerically considering the integral (60) using the numerical solutions to equation (20) for each model.

The VCF and the running diffusion coefficient are both explicitly dependent on $< \mu_0 \mu >$ and $< z^2 >$ respectively. It is also interesting to compare the expectation value $< z >$ for each result. These three quantities give insight into the similarities and differences between each solution. Figure (35) shows the comparison of $< z >$ for each model of the scattering coefficient mentioned in subsection 2.3. These were

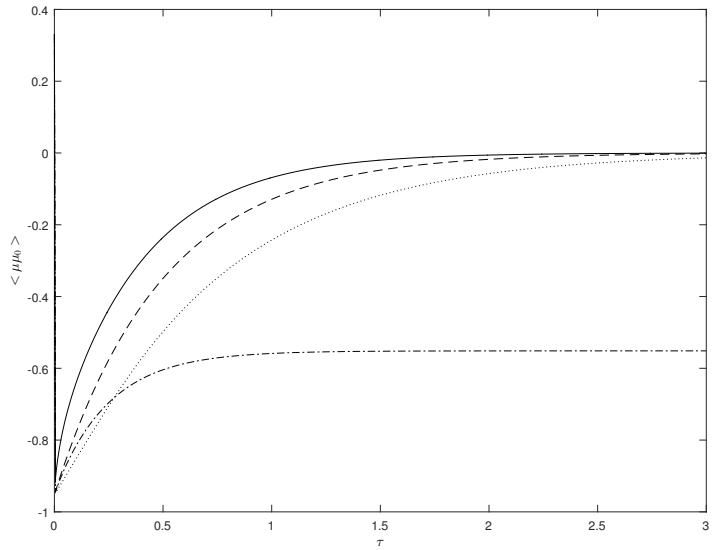

Figure 33: The velocity correlation function, normalized to its original value as a function of the transformed time τ. The solid line is for the constant $D_{\mu\mu}$, the isotropic $D_{\mu\mu}$ is the dashed line, the linear $D_{\mu\mu}$ is the dotted line, the quasi-linear $D_{\mu\mu}$ is the dashed-dotted line.

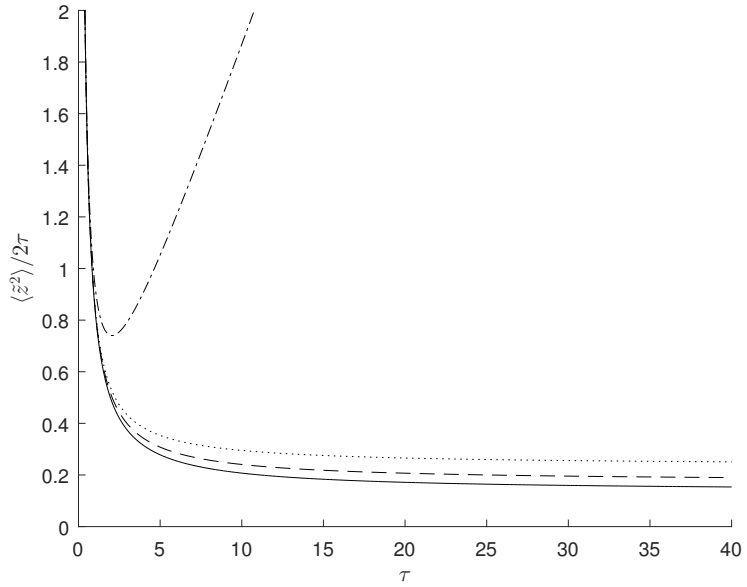

Figure 34: The velocity independent running diffusion coefficient as a function of the transformed time τ. The solid line is for the constant $D_{\mu\mu}$, the isotropic $D_{\mu\mu}$ is the dashed line, the linear $D_{\mu\mu}$ is the dotted line, the quasi-linear $D_{\mu\mu}$ is the dashed-dotted line.

each calculated by numerically solving the integral (60) using the numerical solutions to equation (20)

for each model.

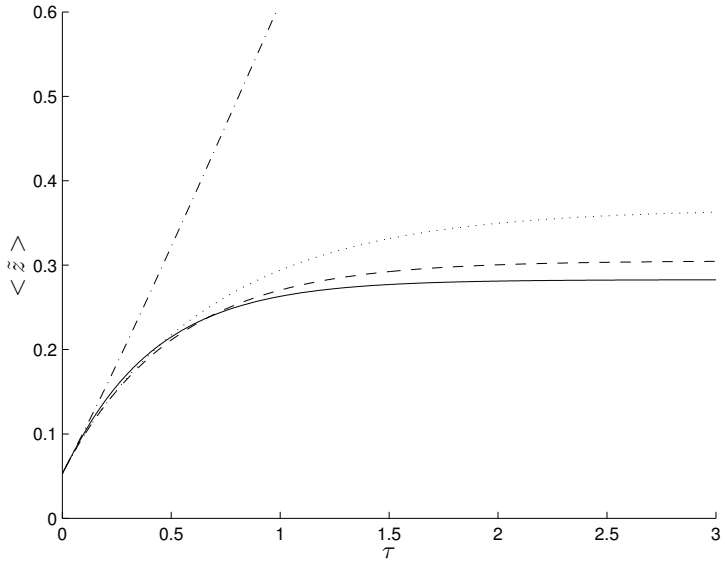

Figure 35: The expectation value $\langle \tilde{z} \rangle$ as a function of the transformed time τ. The solid line is for the constant $D_{\mu\mu}$, the isotropic $D_{\mu\mu}$ is the dashed line, the linear $D_{\mu\mu}$ is the dotted line, the quasi-linear $D_{\mu\mu}$ is the dashed-dotted line.

It can be seen from plots (6) - (35) that the quasi-linear form of $D_{\mu\mu}$ yields extremely different results compared to the isotropic results. In future work equation (54) can be disregarded as a possible model for the scattering coefficient. Also of note is that the constant form of $D_{\mu\mu}$ appears to be equally as valid as, if not more valid than, the linear form when compared to the isotropic form. This means devoting time to solving analytic equations with the constant form may be looked at in future work, as the full Fokker-Planck equation is more likely to be solvable with a constant $D_{\mu\mu}$ than with the linear form. This is a very promising result for future research opportunities.

2.6 Analytic Approximation to the Fokker-Planck Equation

The Fokker-Planck equation in the form (20) has been studied for over a century. However the only analytic solutions to it that have been found contain sums of infinite terms (see Malkov (2017)). These solutions only have a practical use in computational work where large sums can be computed and manipulated more easily than in analytic work. To do useful analytic work scientists must find a more elegant form of the solution. For analytic purposes it is in fact more useful to have a simple solution which is only an approximate solution as long as the approximation is similar enough to the real solution. In this subsection a subspace approximation that makes use of Legendre polynomials is derived and analyzed. Since many different forms of the PDE have thus far been discussed, it should be made clear that this subsection deals only with

$$\frac{\partial f}{\partial t} + v\mu \frac{\partial f}{\partial z} = \frac{\partial}{\partial \mu}\left[D_{\mu\mu}(\mu) \frac{\partial f}{\partial \mu} \right]. \tag{61}$$

2.6.1 The Setup

Since it is unlikely to be possible to solve this equation with an arbitrary pitch-angle coefficient $D_{\mu\mu}$, only the isotropic form is considered.

$$D_{\mu\mu} = D(1 - \mu^2). \tag{62}$$

With the Fourier representation

$$f(z,\mu,t) = \int_{-\infty}^{\infty} dk F(k,\mu,t) e^{ikz}, \tag{63}$$

equation (61) can be written as

$$\frac{\partial F}{\partial t} = -iv\mu k F + D\frac{\partial}{\partial \mu}\left((1-\mu^2)\frac{\partial F}{\partial \mu}\right). \tag{64}$$

Expanding the solution, F, as a series of Legendre polynomials results in

$$F(\mu,t) = \sum_{n=0}^{\infty} C_n(t) P_n(\mu), \tag{65}$$

and equation (64) expanded by this solution leads to

$$\sum_n \dot{C}_n P_n + iv\mu k \sum_n C_n P_n = D\sum_n C_n \frac{\partial}{\partial \mu}\left((1-\mu^2)\frac{\partial P_n}{\partial \mu}\right). \tag{66}$$

It should be noted that the coefficients C_n are functions of t, and k, but not of μ, and the Legendre polynomials are only functions of μ. The following is a well known relation for Legendre polynomials, shown in Abramowitz & Stegun (1964),

$$\frac{\partial}{\partial \mu}\left((1-\mu^2)\frac{\partial P_n}{\partial \mu}\right) = -n(n+1)P_n. \tag{67}$$

Using equation (67) with equation (66) results in

$$\sum_n \dot{C}_n P_n + iv\mu k \sum_n C_n P_n = -D\sum_n C_n n(n+1) P_n. \tag{68}$$

To get rid of the last explicit μ dependence the relation (see Abramowitz & Stegun (1964))

$$\mu P_n(\mu) = \left(\frac{n+1}{2n+1}\right)P_{n+1} + \left(\frac{n}{2n+1}\right)P_{n-1}, \tag{69}$$

is used. One can now write equation (68) as

$$\sum_n \dot{C}_n P_n + ivk \sum_n C_n \left[\left(\frac{n+1}{2n+1}\right)P_{n+1} + \left(\frac{n}{2n+1}\right)P_{n-1}\right] = -D\sum_n C_n n(n+1) P_n. \tag{70}$$

The Legendre polynomial property satisfying the orthogonality relation is (see again Abramowitz & Stegun (1964)),

$$\int_{-1}^{1} d\mu P_n P_m = \frac{2}{2m+1}\delta_{nm}. \tag{71}$$

After multiplying equation (70) by P_m, integrating over all μ, using the orthogonality relation of the Legendre polynomials, and simplifying the resultant equation is

$$\dot{C}_m = -Dm(m+1)C_m - ivk\frac{m}{2m-1}C_{m-1} - ivk\frac{m+1}{2m+3}C_{m+1}. \tag{72}$$

This is an important relationship between each coefficient C_m and its neighboring coefficients C_{m-1} and C_{m+1}, which can be exploited in order to solve equation (65) to different orders. Specifically this is an infinite series of coupled ordinary differential equations (ODEs). The series is terminated by setting $C_{n+m} = 0$ for the n'th order approximation, where $m = 0, 1, 2, ...\infty$. The first three coupled ODE's are as follows. For $m = 0$

$$\dot{C}_0 = \frac{-ivk}{3}C_1, \tag{73}$$

for $m = 1$

$$\dot{C}_1 = -2DC_1 - ivkC_0 - \frac{2ivk}{5}C_2, \tag{74}$$

and for $m = 2$

$$\dot{C}_2 = -6DC_2 - \frac{2ivk}{3}C_1 - \frac{3ivk}{7}C_3. \tag{75}$$

A first, second, and third-order subspace approximation is applied in the following three sections (secs 2.6.2, 2.6.3, and 2.6.4). They are then compared both to each other and numerical results to determine their validity and usefulness.

2.6.2 First-Order Approximation

The first-order approximation corresponds to $C_{1+m} = 0$ for $m \geq 0$. Therefore the only non-trivial relation for the coefficients is equation (73), and the Legendre polynomial solution reduces to

$$F_1(\mu, t) = C_0. \tag{76}$$

To determine C_0 the initial condition is employed

$$F(\mu, t = 0) = \sum_n C_n(t = 0)P_n = \frac{1}{\pi}\delta(\mu - \mu_0), \tag{77}$$

where μ_0 is the initial pitch angle cosine. Multiplying this equation by P_m and integrating over μ leads to

$$C_m(t = 0) = \frac{2m + 1}{2\pi}P_m(\mu_0). \tag{78}$$

Given this equation for $m = 0$,

$$C_0 = \frac{1}{2\pi}, \tag{79}$$

can easily be derived. Since $C_1 = 0$ equation (73) can be integrated over t to show that C_0 is constant in time and therefore

$$C_0(t) = C_0(t = 0) = \frac{1}{2\pi}. \tag{80}$$

Which of course when used with equation (76) results in

$$F_1(\mu, t) = F_1(\mu, t = 0) = \frac{1}{2\pi}. \tag{81}$$

It can also be shown that by integrating this solution over k-space (see equation (63)), the first-order solution to equation (61) as a function of z is

$$f(z, \mu, t) = \delta(z). \tag{82}$$

This is a trivial solution, so higher order approximations must be examined.

2.6.3 Second-Order Approximation

The second-order approximation corresponds to $C^*_{2+m} = 0$ for $m = 0, 1, 2, ...\infty$, where * denotes the difference from the first-order $C's$. Therefore the only non-trivial relations for the coefficients are equations (73) and (74). The Legendre polynomial solution reduces to

$$F_2(\mu, t) = C^*_0 + \mu C^*_1. \tag{83}$$

In order to find C^*_0 and C^*_1 the two coupled first-order ODEs, (73) and (74), must be solved. By basic substitution this problem can be turned into a single second-order ODE given by

$$\ddot{C}^*_0 = -2D\dot{C}^*_0 - \frac{v^2k^2}{3}C^*_0. \tag{84}$$

With this form of ODE, it is customary to use the ansatz

$$C_0^* = \sum_i b_i e^{\omega_i t}. \tag{85}$$

This leads to

$$\omega^2 + 2D\omega + \frac{v^2 k^2}{3} = 0. \tag{86}$$

Thus the eigenvalues ω can be determined to be

$$\omega_\pm = -D \pm \sqrt{D^2 - v^2 k^2/3}. \tag{87}$$

The coefficient C_0^* can now be written as

$$C_0^* = b_+ e^{\omega_+ t} + b_- e^{\omega_- t}, \tag{88}$$

and by using equation (73), it can be determined that

$$C_1^* = \frac{-3}{ivk}(b_+ \omega_+ e^{\omega_+ t} + b_- \omega_- e^{\omega_- t}). \tag{89}$$

The solution $F(\mu, t)$ can therefore be expressed as

$$F_2(\mu, t) = b_+ e^{\omega_+ t} + b_- e^{\omega_- t} - \frac{3\mu}{ivk}(b_+ \omega_+ e^{\omega_+ t} + b_- \omega_- e^{\omega_- t}). \tag{90}$$

In order to find the coefficients $b_\pm$ the initial condition, equation (78) must be used. Using this condition for $m = 0$ and $m = 1$ results in

$$C_0^*(t = 0) = \frac{1}{2\pi}, \tag{91}$$

and

$$C_1^*(t = 0) = \frac{3\mu_0}{2\pi}. \tag{92}$$

Using condition (91) in equation (88), then evaluating it at $t = 0$ results in

$$b_+ + b_- = \frac{1}{2\pi}. \tag{93}$$

Using condition (92) in equation (89), then evaluating it at $t = 0$ results in

$$b_+ \omega_+ + b_- \omega_- = -\frac{ivk\mu_0}{2\pi}. \tag{94}$$

Algebraically solving equations (93) and (94) for b_+ and b_- gives

$$b_\pm = \mp \frac{(ivk\mu_0 + \omega_\mp)}{2\pi(\omega_+ - \omega_-)}. \tag{95}$$

Using equations (95) and (87) in equation (90) provides a full second-order subspace solution $F_2(\mu, t)$. Figures (36), (37), and (38) show the second-order subspace solution to equation (61) for $t = 0$, an anisotropic pitch angle distribution time, and a late time. One can see that over time the pitch angle dependence becomes isotropic, and the particle position parallel to the mean field expands from a Dirac distribution to a Gaussian distribution. These plots are made by taking the solution (90), putting it into equation (63), and numerically integrating over k-space. The transformations, $\tilde{z} = zD/v$, and $\tau = Dt$ were made to allow for proper numerical integration and plotting. It should be noted that at early times there is some noise in the analytic solution due to the numerical integration of equation (63). This is true for each of the 3 orders of solutions. Forms of the second order solution for the weak scattering ($D^2 \ll v^2 k^2/3$) and strong scattering ($D^2 \gg v^2 k^2/3$) limits are explored in Lasuik & Shalchi (2019).

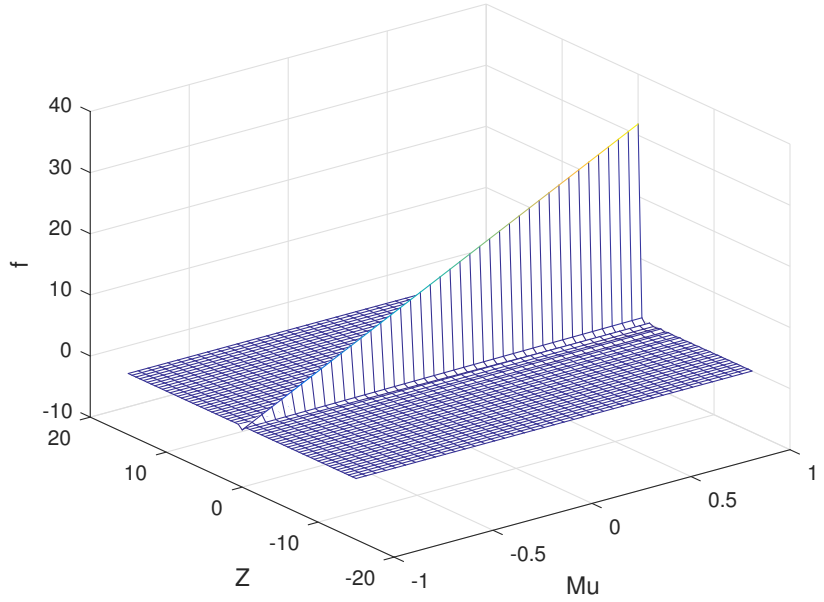

Figure 36: The second-order solution $f(z, \mu, t)$ as given by equation (63), using equation (90), for the time $\tau = 0$.

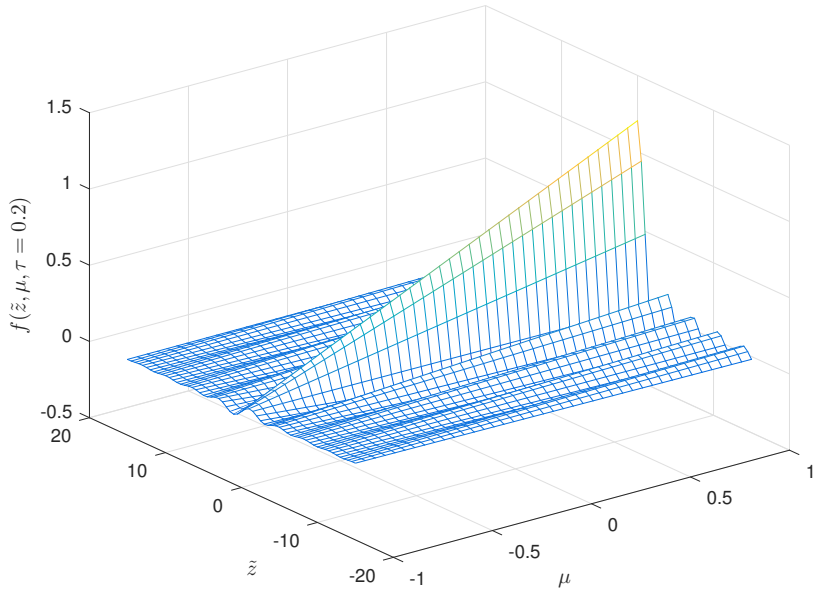

Figure 37: The second-order solution $f(z, \mu, t)$ as given by equation (63), using equation (90), for the time $\tau = 0.2$.

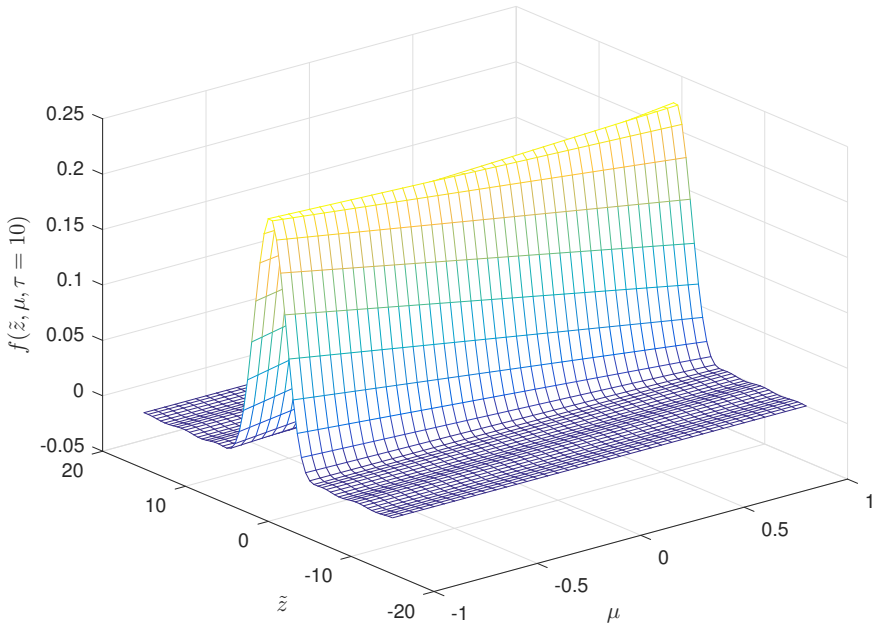

Figure 38: The second-order solution $f(z, \mu, t)$ as given by equation (63), using equation (90), for the time $\tau = 10$.

2.6.4 Third-Order Approximation

The third-order approximation corresponds to $C^{**}_{3+m} = 0$ for $m = 0, 1, 2, ...\infty$. Therefore the non-trivial relations for the coefficients are given by equations (73), (74), and (75), and the Legendre polynomial solution reduces to

$$F_3(\mu, t) = C^{**}_0 + \mu C^{**}_1 + \frac{1}{2}(3\mu^2 - 1)C^{**}_2. \tag{96}$$

In order to find C^{**}_0, C^{**}_1, and C^{**}_2 the coupled first-order ODEs, (73), (74), and (75), must be solved. By substitution this problem can be turned into a single third-order ODE given by

$$3\dddot{C}^{**}_0 + 24D\ddot{C}^{**}_0 + (36D^2 + \frac{9}{5}v^2k^2)\dot{C}^{**}_0 + 6Dv^2k^2C^{**}_0 = 0. \tag{97}$$

Using the ansatz

$$C^{**}_0 = \sum_{i=1}^{3} b_i e^{\omega_i t} \tag{98}$$

leads to

$$3\omega^3 + 24D\omega^2 + (36D^2 + \frac{9}{5}v^2k^2)\omega + 6Dv^2k^2 = 0. \tag{99}$$

To determine the coefficients b_i, the initial condition, (77), must be utilized. Which, as in the above subsubsection, leads to the initial coefficient relation (78). Using this relation for $m = 0$ and $m = 1$ results in equations (91) and (92) respectively. Using this relation for $m = 2$ results in

$$C^{**}_2(t = 0) = \frac{5}{4\pi}(3\mu_0^2 - 1). \tag{100}$$

Using condition (91) in equation (98) evaluated at $t = 0$ results in

$$b_1 + b_2 + b_3 = \frac{1}{2\pi}. \tag{101}$$

Using condition (92) along with equation (98) in equation (73) evaluated at $t = 0$ results in

$$b_1\omega_1 + b_2\omega_2 + b_3\omega_3 = -\frac{ivk\mu_0}{2\pi}. \tag{102}$$

Now considering the time derivative of equation (73), and using equation (98) evaluated at $t = 0$ leads to

$$b_1\omega_1^2 + b_2\omega_2^2 + b_3\omega_3^2 = -\frac{ivk}{3}\frac{dC_1^{**}}{dt}\bigg|_{t=0}. \tag{103}$$

Finally using equations (91), (92), (100), and (103) in equation (75), then evaluating it at $t = 0$ results in the third linear equation for the $b_i's$

$$\frac{3}{ivk}(b_1\omega_1^2 + b_2\omega_2^2 + b_3\omega_3^2) = \frac{3D\mu_0}{\pi} + \frac{ivk}{2\pi} + \frac{ivk}{2\pi}(3\mu_0^2 - 1). \tag{104}$$

Solving the linear equations (101), (102), and (104) for b_1, b_2, and b_3 results in

$$\begin{aligned} b_1 &= \frac{ivk\mu_0(2D + \omega_2 + \omega_3) - v^2k^2\mu_0 + \omega_2\omega_3}{2\pi(\omega_1 - \omega_2)(\omega_1 - \omega_3)}, \\ b_2 &= \frac{ivk\mu_0(2D + \omega_1 + \omega_3) - v^2k^2\mu_0 + \omega_1\omega_3}{2\pi(\omega_2 - \omega_3)(\omega_2 - \omega_1)}, \\ b_3 &= \frac{ivk\mu_0(2D + \omega_1 + \omega_2) - v^2k^2\mu_0 + \omega_1\omega_2}{2\pi(\omega_1 - \omega_3)(\omega_2 - \omega_3)}. \end{aligned} \tag{105}$$

The third-order solution has three roots corresponding to the 3 eigenvalues of equation (98), these were found using Matlab's Symbolic Toolbox and are given by

$$\begin{aligned} \omega_1 = &\left(\left(\left(\frac{k^2v^2}{5} - \frac{(28D^2)}{9}\right)^3 + \left(\frac{(512D^3)}{27} - \frac{(4D(12D^2 + \frac{(3k^2v^2)}{5}))}{3} + Dk^2v^2\right)^2\right)^{(1/2)} - \frac{(512D^3)}{27}\right. \\ &\left. + \frac{\left(4D(12D^2 + \frac{(3k^2v^2)}{5})\right)}{3} - Dk^2v^2\right)^{(1/3)} - \frac{(8D)}{3} - \left(\frac{k^2v^2}{5} - \frac{(28D^2)}{9}\right)\Big/\left(-\frac{(512D^3)}{27}\right. \\ &\left. + \left(\left(\frac{k^2v^2}{5} - \frac{(28D^2)}{9}\right)^3 + \left(\frac{(512D^3)}{27} - \frac{(4D(\frac{(3k^2v^2)}{5} + 12D^2))}{3} + Dk^2v^2\right)^2\right)^{(1/2)} + \frac{(4D(\frac{(3k^2v^2)}{5} + 12D^2))}{3}\right. \\ &\left. - Dk^2v^2\right)^{(1/3)}, \end{aligned} \tag{106}$$

$$\begin{aligned} \omega_2 = &\left(\frac{k^2v^2}{5} - \frac{(28D^2)}{9}\right)\left(2\left(-\frac{(512D^3)}{27} + \left(\left(\frac{k^2v^2}{5} - \frac{(28D^2)}{9}\right)^3 + \left(\frac{(512D^3)}{27} - \frac{(4D(\frac{(3k^2v^2)}{5} + 12D^2))}{3}\right.\right.\right.\right. \\ &\left.\left.\left.\left. + Dk^2v^2\right)^2\right)^{(1/2)} + \frac{(4D(\frac{(3k^2v^2)}{5} + 12D^2))}{3} - Dk^2v^2\right)^{(1/3)}\right)^{-1} - \left(\left(\left(\frac{k^2v^2}{5} - \frac{(28D^2)}{9}\right)^3 + \left(\frac{(512D^3)}{27}\right.\right.\right. \\ &\left.\left.\left. - \frac{(4D(12D^2 + \frac{(3k^2v^2)}{5}))}{3} + Dk^2v^2\right)^2\right)^{(1/2)} - \frac{(512D^3)}{27} + \frac{(4D(12D^2 + \frac{(3k^2v^2)}{5}))}{3} - \right. \\ &\left. Dk^2v^2\right)^{(1/3)}/2 - \frac{(8D)}{3} - \left(3^{(1/2)}\left(\left(\left(\left(\frac{k^2v^2}{5} - \frac{(28D^2)}{9}\right)^3 + \left(\frac{(512D^3)}{27} - \frac{(4D(12D^2 + \frac{(3k^2v^2)}{5}))}{3}\right.\right.\right.\right. \right. \\ &\left.\left.\left.\left. + Dk^2v^2\right)^2\right)^{(1/2)} - \frac{(512D^3)}{27} + \frac{(4D(12D^2 + \frac{(3k^2v^2)}{5}))}{3} - Dk^2v^2\right)^{(1/3)} \right. \\ &\left. + \left(\frac{k^2v^2}{5} - \frac{(28D^2)}{9}\right)\Big/\left(-\frac{(512D^3)}{27} + \left(\left(\frac{k^2v^2}{5} - \frac{(28D^2)}{9}\right)^3 + \left(\frac{(512D^3)}{27} - \frac{(4D(\frac{(3k^2v^2)}{5} + 12D^2))}{3}\right.\right.\right. \right. \\ &\left.\left.\left. + Dk^2v^2\right)^2\right)^{(1/2)} + \frac{(4D(\frac{(3k^2v^2)}{5} + 12D^2))}{3} - Dk^2v^2\right)^{(1/3)}\right)i\Big)/2, \end{aligned} \tag{107}$$

and

$$\omega_3 = \left(\frac{k^2v^2}{5} - \frac{(28D^2)}{9}\right)\left(2\Big(-\frac{(512D^3)}{27} + \Big((\frac{k^2v^2}{5} - \frac{(28D^2)}{9})^3 + (\frac{(512D^3)}{27} - \frac{(4D(\frac{(3k^2v^2)}{5} + 12D^2))}{3} + Dk^2v^2)^2\Big)^{(1/2)} + \frac{(4D(\frac{(3k^2v^2)}{5} + 12D^2))}{3} - Dk^2v^2\Big)^{(1/3)}\right)^{-1} - \left(\Big((\frac{k^2v^2}{5} - \frac{(28D^2)}{9})^3 + \Big(\frac{(512D^3)}{27} - \frac{(4D(12D^2 + \frac{(3k^2v^2)}{5}))}{3} + Dk^2v^2\Big)^2\Big)^{(1/2)} - \frac{(512D^3)}{27} + \frac{(4D(12D^2 + \frac{(3k^2v^2)}{5}))}{3} - Dk^2v^2\right)^{(1/3)}/2 - \frac{(8D)}{3} + \left(3^{(1/2)}\left(\Big(\Big((\frac{k^2v^2}{5} - \frac{(28D^2)}{9})^3 + (\frac{(512D^3)}{27} - \frac{(4D(12D^2 + \frac{(3k^2v^2)}{5}))}{3} + Dk^2v^2)^2\Big)^{(1/2)} - \frac{(512D^3)}{27} + \frac{(4D(12D^2 + \frac{(3k^2v^2)}{5}))}{3} - Dk^2v^2\Big)^{(1/3)} + \Big(\frac{k^2v^2}{5} - \frac{(28D^2)}{9}\Big)/\Big(-\frac{(512D^3)}{27} + \Big((\frac{k^2v^2}{5} - \frac{(28D^2)}{9})^3 + (\frac{(512D^3)}{27} - \frac{(4D(\frac{(3k^2v^2)}{5} + 12D^2))}{3} + Dk^2v^2)^2\Big)^{(1/2)} + \frac{(4D(\frac{(3k^2v^2)}{5} + 12D^2))}{3} - Dk^2v^2\Big)^{(1/3)}\right)i\Big)/2. \tag{108}$$

Along with equations (96), (98), (106), (107), (108) and (105) the equations

$$C_1^{**} = -\frac{3}{ivk}\dot{C_0^{**}} \tag{109}$$

and

$$C_2^{**} = -\frac{5}{2ivk}(\dot{C_1^{**}} + 2DC_1^{**} + ivkC_0^{**}) \tag{110}$$

offer a complete solution to the third-order subspace approximation of equation (64). Figures (39), (40), and (41) show the third-order subspace approximate solution to equation (61) for an initial time, an anisotropic distribution time, and a late time.

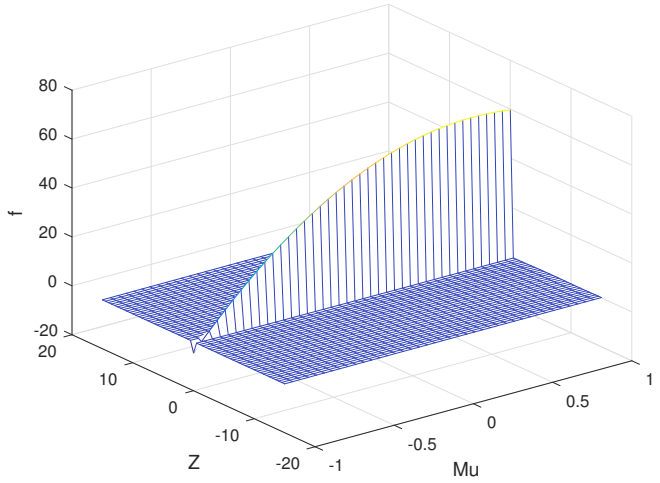

Figure 39: The third-order solution $f(z, \mu, t)$ as given by equation (63), using equation (96), for the time $\tau = 0$.

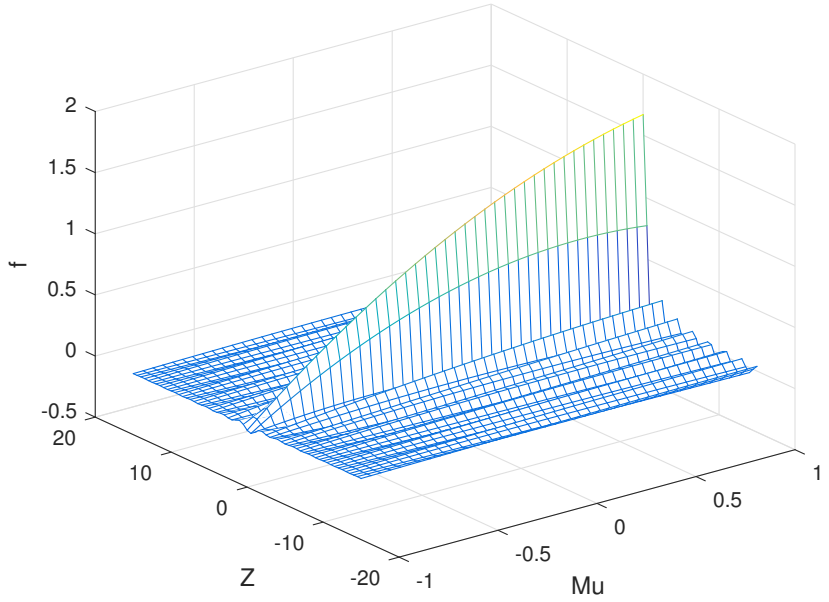

Figure 40: The third-order solution $f(z, \mu, t)$ as given by equation (63), using equation (96), for the time $\tau = 0.2$.

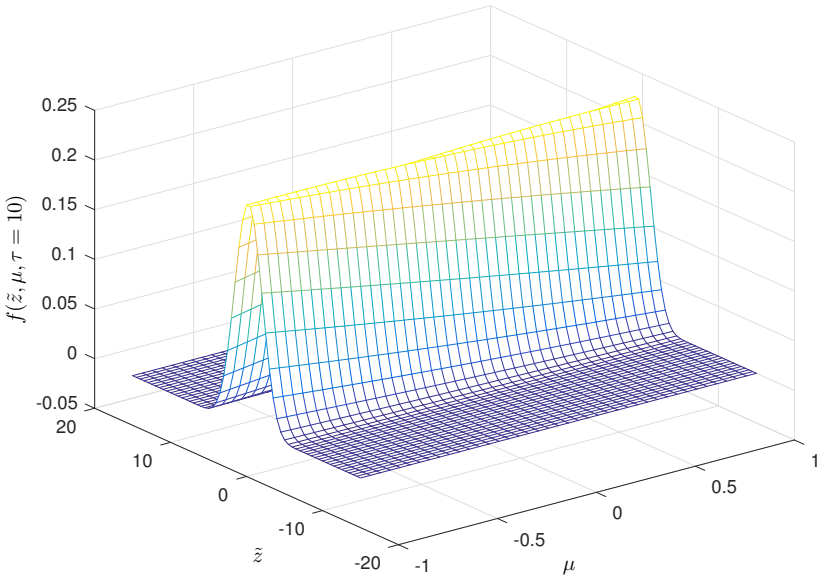

Figure 41: The third-order solution $f(z, \mu, t)$ as given by equation (63), using equation (96), for the time $\tau = 10$.

2.6.5 Normalization

All solutions to equation (61) must follow the normalization condition

$$\frac{1}{2}\int_{-1}^{1} d\mu \int_{-\infty}^{\infty} dz f(z,\mu,t) = 1. \tag{111}$$

Replacing $f(z,\mu,t)$ with $F(k,\mu,t)$ using equation (63) and integrating over z leads to the normalization condition

$$\int_{-1}^{1} d\mu F(k=0,\mu,t) = \frac{1}{\pi}. \tag{112}$$

It can be shown that the analytic solutions for all orders follow the normalization condition despite no explicit enforcement of that condition during derivations. For the first-order solution

$$F_1(k=0,\mu,t) = \frac{1}{2\pi}. \tag{113}$$

Therefore

$$\int_{-1}^{1} d\mu F_1(k=0,\mu,t) = \frac{1}{\pi}. \tag{114}$$

To evaluate $F(k=0,\mu,t)$ for the second-order solution the following evaluations must be used.

$$\omega_+(k=0) = 0, \tag{115}$$

$$\omega_-(k=0) = -2D, \tag{116}$$

$$b_+(k=0) = \frac{1}{2\pi}, \tag{117}$$

and

$$b_-(k=0) = 0, \tag{118}$$

As well one must consider the limits as $k \to 0$ of ω_+/k, and b_-/k. Each of these at first glance evaluate to $0/0$, therefore L'Hôpital's rule may be used. After one use of L'Hôpital's rule ω_+/k becomes

$$\lim_{k\to 0}\frac{\omega_+}{k} = \lim_{k\to 0}\frac{d\omega_+}{dk}, \tag{119}$$

where

$$\frac{d\omega_+}{dk} = \frac{-v^2k/3}{2\sqrt{D^2 - v^2k^2/3}}, \tag{120}$$

which evaluates to 0 at $k=0$. Therefore

$$\lim_{k\to 0}\frac{\omega_+}{k} = 0. \tag{121}$$

After one use of L'Hôpital's rule the limit of b_-/k as $k \to 0$ becomes

$$\lim_{k\to 0}\frac{b_-}{k} = \lim_{k\to 0}\frac{db_-}{dk}, \tag{122}$$

where

$$\frac{db_-}{dk} = \left(\frac{1}{4\pi^2(\omega_+ - \omega_-)^2}\right)\left(\frac{d\omega_+}{dk}\big(2\pi(\omega_+ - \omega_-)\big) - (ivk\mu_0 + \omega_+)\Big(2\pi\frac{d\omega_+}{dk} - 2\pi\frac{d\omega_-}{dk}\Big)\right), \tag{123}$$

which evaluates to 0 at $k=0$. Therefore

$$\lim_{k\to 0}\frac{b_-}{k} = 0. \tag{124}$$

It is now clear that

$$F_2(k=0,\mu,t)=\frac{1}{2\pi}, \tag{125}$$

and therefore

$$\int_{-1}^{1} d\mu F_2(k=o,\mu,t)=\frac{1}{\pi}. \tag{126}$$

To show that the third-order solution is normalized it is convenient to show that after integrating over all μ some of the terms in the solution (96) vanish for any arbitrary coefficients. Firstly all terms of odd order in μ go to 0 after integration due to their symmetry, and secondly the integral

$$\int_{-1}^{1} d\mu(3\mu^2-1)=0. \tag{127}$$

Therefore the integral to prove normalization

$$\int_{-1}^{1} d\mu\big(C_0^{**}(k=0)+\mu C_1^{**}(k=0)+\frac{1}{2}(3\mu^2-1)C_2^{**}(k=0)\big), \tag{128}$$

reduces to

$$\int_{-1}^{1} d\mu C_0^{**}(k=0). \tag{129}$$

$C_0^{**}(k=0)$ is given by

$$C_0^{**}(k=0)=\sum_{i-1}^{3} b_i(k=0)e^{\omega_i(k=0)t}, \tag{130}$$

where

$$\begin{aligned}
\omega_1(k=0)&=\frac{D}{3}\left((-80+72\sqrt{3}i)^{1/3}-8+\frac{28}{(-80+72\sqrt{3}i)^{1/3}}\right)=0,\\
\omega_2(k=0)&=\frac{-D}{3}\left(\frac{1+\sqrt{3}i}{2}(-80+72\sqrt{3}i)^{1/3}+8+\frac{14-14\sqrt{3}i}{(-80+72\sqrt{3}i)^{1/3}}\right)=-2D,\\
\omega_3(k=0)&=\frac{-D}{3}\left(\frac{1-\sqrt{3}i}{2}(-80+72\sqrt{3}i)^{1/3}+8+\frac{14+14\sqrt{3}i}{(-80+72\sqrt{3}i)^{1/3}}\right)=-6D.
\end{aligned} \tag{131}$$

as well as

$$\begin{aligned}
b_1(k=0)&=\frac{(\omega_2\omega_3)|_{k=0}}{2\pi(\omega_1-\omega_2)|_{k=0}(\omega_1-\omega_3)|_{k=0}},\\
b_2(k=0)&=\frac{(\omega_1\omega_3)|_{k=0}}{2\pi(\omega_2-\omega_3)|_{k=0}(\omega_2-\omega_1)|_{k=0}},\\
b_3(k=0)&=\frac{(\omega_1\omega_2)|_{k=0}}{2\pi(\omega_1-\omega_3)|_{k=0}(\omega_2-\omega_3)|_{k=0}},
\end{aligned} \tag{132}$$

To properly evaluate equations (132), the following evaluations are required

$$\begin{aligned}
(\omega_1-\omega_2)|_{k=0}&=\frac{D}{3}\left((-80+72\sqrt{3}i)\frac{(3-\sqrt{3}i)}{2}+\frac{(42+14\sqrt{3}i)}{(-80+72\sqrt{3}i)^{1/3}}\right)=6D,\\
(\omega_2-\omega_3)|_{k=0}&=\frac{D}{3}\left(\frac{28\sqrt{3}i}{(-80+72\sqrt{3}i)^{1/3}}-\sqrt{3}i(-80+72\sqrt{3}i)^{1/3}\right)=4D,\\
(\omega_1-\omega_2)|_{k=0}&=\frac{D}{3}\left(\frac{(42-14\sqrt{3}i)}{(-80+72\sqrt{3}i)^{1/3}}+\frac{(3+\sqrt{3}i)}{2}(-80+72\sqrt{3}i)^{1/3}\right)=2D.
\end{aligned} \tag{133}$$

These all being finite and simple, it is now easy to show

$$\begin{aligned}
b_1(k=0)&=\frac{1}{2\pi},\\
b_2(k=0)&=0,\\
b_3(k=0)&=0.
\end{aligned} \tag{134}$$

Therefore $C_0^{**}(k=0)$ becomes

$$C_0^{**}(k=0) = \frac{1}{2\pi}, \tag{135}$$

and

$$\int_{-1}^{1} d\mu C_0^{**}(k=0) = \frac{1}{\pi}. \tag{136}$$

Thus the normalization condition

$$\int_{-1}^{1} d\mu F_3(k=0,\mu,t) = \frac{1}{\pi} \tag{137}$$

is satisfied for the third-order solution.

2.6.6 Deriving General Properties of the Solutions

The expectation value of a variable in a solution can be defined as

$$\langle A \rangle = \frac{1}{2}\int_{-1}^{1} d\mu \int_{-\infty}^{\infty} dz A f(z,\mu,t). \tag{138}$$

The interesting expectation values of the solutions are $\langle z \rangle$, $\langle z^2 \rangle$, $\langle \mu \rangle$, $\langle \mu^2 \rangle$, $\langle e^{-ikz} \rangle$, $\langle \mu_0 \mu e^{-ikz} \rangle$, and $\langle \mu_0 \mu e^{-i\vec{k}\cdot\vec{x}} \rangle$. For the latter 3 expectation values one must also integrate over all possible initial pitch angles, μ_0. Before calculation these expectation values must be written in terms of the Fourier space solution. The following shows how each expectation value can be written as such. First by definition (138),

$$\langle z^n \rangle = \frac{1}{2}\int_{-1}^{1} d\mu \int_{-\infty}^{\infty} dz z^n f(z,\mu,t). \tag{139}$$

Which by equation (63), can be written in Fourier space as

$$\langle z^n \rangle = \frac{1}{2}\int_{-1}^{1} d\mu \int_{-\infty}^{\infty} dk F(k,\mu,t) \int_{-\infty}^{\infty} z^n e^{ikz}. \tag{140}$$

By deriving e^{ikz} n-times one can show that

$$z^n e^{ivk} = (-i)^n \frac{d^n}{dk^n} e^{ivk}. \tag{141}$$

Using equations (140) and (141) and then integrating over z results in

$$\langle z^n \rangle = (-i)^n \pi \int_{-1}^{1} d\mu \int_{-\infty}^{\infty} dk F(k,\mu,t) \frac{d^n}{dk^n}\delta(k). \tag{142}$$

Then integrating by parts n-times gives

$$\begin{aligned} \langle z^n \rangle = (-i)\pi^n \pi \int_{-1}^{1} d\mu \Bigg(F \frac{d^{n-1}\delta(k)}{dk^{n-1}}\Big|_{-\infty}^{\infty} - \frac{dF}{dk}\frac{d^{n-2}\delta(k)}{dk^{n-2}}\Big|_{-\infty}^{\infty} + \\ ... + (-1)^{n-1}\delta(k)\frac{d^{n-1}F}{dk^{n-1}}\Big|_{-\infty}^{\infty} + (-1)^n \int_{-\infty}^{\infty} dk \delta(k) \frac{d^n F}{dk^n} \Bigg), \end{aligned} \tag{143}$$

which reduces to

$$\langle z^n \rangle = (i)^n \pi \int_{-1}^{1} d\mu \int_{-\infty}^{\infty} dk \frac{d^n}{dk^n}(F(k,\mu,t))\delta(k), \tag{144}$$

because $\delta(k)$ and all of its derivatives are 0 as $k \to \pm\infty$. Integrating over k gives the general result of

$$\langle z^n \rangle = (i)^n \pi \int_{-1}^{1} d\mu \left(\frac{d^n}{dk^n}(F(k,\mu,t)) \right)\Big|_{k=0}. \tag{145}$$

Take note of the Legendre polynomial property that

$$\int_{-1}^{1} dx P_m(x) = \begin{cases} 2 & m = 0 \\ 0 & m > 0 \end{cases}. \tag{146}$$

Since Legendre polynomials are being used to approximate the solutions equations (65) and (146) can be used in equation (145). Then by integrating over μ, one can write

$$\langle z^n \rangle = 2\pi(i)^n \left(\frac{d^n}{dk^n}(C_0(k,t)) \right) \Big|_{k=0}. \tag{147}$$

For $\langle \mu \rangle$, by definition (138),

$$\langle \mu \rangle = \frac{1}{2} \int_{-1}^{1} d\mu \int_{-\infty}^{\infty} dz \mu f(z, \mu, t). \tag{148}$$

Which by equation (63), can be written in Fourier space as

$$\langle \mu \rangle = \frac{1}{2} \int_{-1}^{1} d\mu \mu \int_{-\infty}^{\infty} dk F(k, \mu, t) \int_{-\infty}^{\infty} dz e^{ikz}. \tag{149}$$

Using the relation

$$\int_{-\infty}^{\infty} dy e^{ixy} = 2\pi\delta(x), \tag{150}$$

leads to to

$$\langle \mu \rangle = \pi \int_{-1}^{1} d\mu \mu \int_{-\infty}^{\infty} dk F(k, \mu, t) \delta(k). \tag{151}$$

Integrating over k space gives

$$\langle \mu \rangle = \pi \int_{-1}^{1} d\mu \mu \int_{-\infty}^{\infty} dk F(k, \mu, t) \delta(k), \tag{152}$$

and then integrating again over z gives

$$\langle \mu \rangle = \pi \int_{-1}^{1} d\mu \mu F(k = 0, \mu, t). \tag{153}$$

Since $\mu = P_1(\mu)$ equation (65) can be used to write

$$\langle \mu \rangle = \pi \sum_{n=0}^{\infty} C_n(k,t) \Big|_{k=0} \int_{-1}^{1} d\mu P_1(\mu) P_n(\mu). \tag{154}$$

Then equation (71) can be used to write

$$\langle \mu \rangle = \frac{2\pi}{3} \sum_{n=0}^{\infty} C_n(k,t) \Big|_{k=0} \delta_{1,n}. \tag{155}$$

Making use of the Kronecker delta to evaluate the sum results in

$$\langle \mu \rangle = \frac{2\pi}{3} C_1(k,t) \Big|_{k=0}. \tag{156}$$

For $\langle \mu \rangle$

$$\langle \mu^2 \rangle = \frac{1}{2} \int_{-1}^{1} d\mu \int_{-\infty}^{\infty} dz \mu^2 f(z, \mu, t). \tag{157}$$

Which by equation (63), can be written in Fourier space as

$$\langle \mu^2 \rangle = \frac{1}{2} \int_{-1}^{1} d\mu \mu^2 \int_{-\infty}^{\infty} dk F(k, \mu, t) \int_{-\infty}^{\infty} dz e^{ikz}. \tag{158}$$

Integrating over k space gives

$$\langle \mu^2 \rangle = \pi \int_{-1}^{1} d\mu \mu^2 \int_{-\infty}^{\infty} dk F(k,\mu,t)\delta(k), \tag{159}$$

and then integrating again over z gives

$$\langle \mu^2 \rangle = \pi \int_{-1}^{1} d\mu \mu^2 F(k=0,\mu,t). \tag{160}$$

Since $\mu^2 = 2P_2(\mu)/3 + P_0(\mu)/3$ equation (65) is used to write

$$\langle \mu^2 \rangle = \pi \sum_{n=0}^{\infty} C_n(k,t)\Big|_{k=0} \left(\int_{-1}^{1} d\mu \frac{2}{3} P_2(\mu) P_n(\mu) + \int_{-1}^{1} d\mu \frac{1}{3} P_0(\mu) P_n(\mu) \right). \tag{161}$$

Then equation (71) is used to show

$$\langle \mu^2 \rangle = \frac{4\pi}{15} \sum_{n=0}^{\infty} C_n(k,t)\Big|_{k=0} \delta_{2,n} + \frac{2\pi}{3} \sum_{n=0}^{\infty} C_n(k,t)\Big|_{k=0} \delta_{0,n}, \tag{162}$$

which by use of the Dirac to evaluate the sum results in

$$\langle \mu^2 \rangle = \frac{4\pi}{15} C_2(k=0,t) + \frac{2\pi}{3} C_0(k=0,t). \tag{163}$$

To evaluate $\langle \mu_0 \mu e^{-ikz} \rangle$ first the integral over initial pitch angle must be added to definition (138), as such

$$\langle \mu_0 \mu e^{-ikz} \rangle = \frac{1}{4} \int_{-1}^{1} d\mu_0 \int_{-1}^{1} d\mu \int_{-\infty}^{\infty} dz \mu_0 \mu e^{-ikz} f(z,\mu,t). \tag{164}$$

Replacing $f(z,\mu,t)$ with equation (63) leads to

$$\langle \mu_0 \mu e^{-ikz} \rangle = \frac{1}{4} \int_{-1}^{1} d\mu_0 \mu_0 \int_{-1}^{1} d\mu \mu \int_{-\infty}^{\infty} dk' F(k',\mu,t) \int_{-\infty}^{\infty} dz e^{i(k'-k)z}, \tag{165}$$

which integrates over z to

$$\langle \mu_0 \mu e^{-ikz} \rangle = \frac{\pi}{2} \int_{-1}^{1} d\mu_0 \mu_0 \int_{-1}^{1} d\mu \mu \int_{-\infty}^{\infty} dk' F(k',\mu,t)\delta(k'-k). \tag{166}$$

This simplifies to

$$\langle \mu_0 \mu e^{-ikz} \rangle = \frac{\pi}{2} \int_{-1}^{1} d\mu_0 \mu_0 \int_{-1}^{1} d\mu \mu F(k,\mu,t). \tag{167}$$

Replacing $F(k,\mu,t)$ with equation (65), and μ with $P_1(\mu)$ results in

$$\langle \mu_0 \mu e^{-ikz} \rangle = \frac{\pi}{2} \int_{-1}^{1} d\mu_0 \mu_0 \int_{-1}^{1} d\mu \sum_n C_n P_n P_1, \tag{168}$$

which due to the orthogonality of Legendre polynomials (equation (71)) reduces to

$$\langle \mu_0 \mu e^{-ikz} \rangle = \frac{\pi}{3} \int_{-1}^{1} d\mu_0 \mu_0 C_1. \tag{169}$$

One can similarly derive the equation for $\langle e^{-ikz} \rangle$. Beginning with equation (167) without the $\mu\mu_0$ term,

$$\langle e^{-ikz} \rangle = \frac{\pi}{2} \int_{-1}^{1} d\mu_0 \int_{-1}^{1} d\mu F(k,\mu,t). \tag{170}$$

Then replacing $F(k,\mu,t)$ with equation (65), and taking advantage of the fact that $P_0 = 1$ gives

$$\langle e^{-ikz}\rangle = \frac{\pi}{2}\int_{-1}^{1} d\mu_0 \int_{-1}^{1} d\mu \sum_n C_n P_n P_0. \tag{171}$$

Again due to Legendre orthogonality this reduces to

$$\langle e^{-ikz}\rangle = \pi \int_{-1}^{1} d\mu_0 C_0. \tag{172}$$

To determine $\langle \mu\mu_0 e^{-i\vec{k}\cdot\vec{x}}\rangle$, one can split up the exponential $e^{-i\vec{k}\cdot\vec{x}}$ into the product $e^{-i\vec{k}_\parallel\cdot\vec{x}_\parallel}e^{-i\vec{k}_\perp\cdot\vec{x}_\perp}$. Now using this product, and equation (167) it should be obvious that

$$\langle \mu_0\mu e^{-i\vec{k}\cdot\vec{x}}\rangle = \frac{\pi}{2}\int_{-1}^{1} d\mu_0\mu_0 \int_{-1}^{1} d\mu\mu F(k,\mu,t) e^{-i\vec{k}_\perp\cdot\vec{x}_\perp}. \tag{173}$$

A model for $e^{-ik_\perp\cdot x_\perp}$ must be made in order to solve this integral. Two models will be used. The first model is

$$e^{-i\vec{k}_\perp\cdot\vec{x}_\perp} = e^{-\alpha|\mu|}, \tag{174}$$

and the second model is

$$. \tag{175}$$

2.6.7 Properties of the First-Order Solution

For the first-order solution, given equation (76), it can be seen that the expectation value of μ is

$$\langle\mu\rangle_1 = 0, \tag{176}$$

where the subscript 1 is used to denote that this is the first-order expectation value. Similarly for the expectation value of $\mu_0\mu e^{-ikz}$,

$$\langle \mu_0\mu e^{-ikz}\rangle_1 = 0. \tag{177}$$

To find $\langle\mu^2\rangle$, recall that for first-order $C_2 = 0$, and $C_0 = 1/2\pi$, therefore by equation (163),

$$\langle\mu^2\rangle_1 = \frac{1}{3}. \tag{178}$$

Since C_0 is a constant in the solution (80) equation (147) can be used to also see that

$$\langle z\rangle_1 = \langle z^2\rangle_1 = 0. \tag{179}$$

Specifically $C_0 = \frac{1}{2\pi}$ which along with equation (172) leads to

$$\langle e^{-ikz}\rangle_1 = 1. \tag{180}$$

Recall that for the expectation value $\langle \mu\mu_0 e^{-i\vec{k}\cdot\vec{x}}\rangle$ there are two models (174) and (175). Using the model $e^{-i\vec{k}_\perp\cdot\vec{x}_\perp} = e^{-\alpha|\mu|}$ is the same result as using the model $e^{-i\vec{k}_\perp\cdot\vec{x}_\perp} = e^{-\beta\mu^2}$. This result is that

$$\langle \mu\mu_0 e^{-i\vec{k}\cdot\vec{x}}\rangle_1 = 0. \tag{181}$$

2.6.8 Properties of the Second-Order Solution

For the second-order solution, given (83), equations (89) and (156) are used to write

$$\begin{aligned}\langle\mu\rangle_2 = \frac{2\pi}{ivk}&(b_+(k=0)\omega_+(k=0)e^{\omega_+(k=0)(k=0)t}\\ &+ b_-(k=0)\omega_-(k=0)e^{\omega_-(k=0)t}).\end{aligned} \tag{182}$$

Now $\omega_\pm(k=0)$ and $b_\pm(k=0)$ must be evaluated. By observing equation (87), it is obvious that

$$\begin{aligned}\omega_+(k=0)&=0,\\ \omega_-(k=0)&=-2D.\end{aligned} \tag{183}$$

By evaluating equation (95) at $k=0$ it can be shown that

$$\begin{aligned}b_+(k=0)&=\frac{-1}{2\pi},\\ b_-(k=0)&=0.\end{aligned} \tag{184}$$

The limits of ω_+/k and b_-/k as $k\to 0$ now have to be considered. L'Hôpital's rule is used to show that

$$\lim_{k\to 0}\frac{\omega_+}{k}=\lim_{k\to 0}\frac{d}{dk}\omega_+=0. \tag{185}$$

This limit can be used to show that

$$\lim_{k\to 0}\frac{b_-}{k}=\frac{-iv\mu_0}{4\pi D}. \tag{186}$$

Using equations (185) and (186) results in

$$\langle\mu\rangle_2=\mu_0 e^{-2Dt}. \tag{187}$$

To determine $\langle\mu^2\rangle$ recall that for the second-order solution $C_2^*=0$, and $C_0^*=b_+e^{\omega_+ t}+b_-e^{\omega_- t}$. By using the limits (183) and (184) along with equation (163) it is easy to show that,

$$\langle\mu^2\rangle_2=\frac{1}{3}. \tag{188}$$

To determine the expectation value of $\mu_0\mu e^{-ikz}$ for the second-order solution, the following integral must be considered,

$$\int_{-1}^{1}d\mu_0\mu_0 b_\pm=\int_{-1}^{1}d\mu_0\Big(\frac{ivk\mu_0^2+\omega_\pm\mu_0}{2\pi(\omega_+-\omega_-)}\Big). \tag{189}$$

Any terms with odd powers of μ_0 integrate to zero over the given interval. Therefore

$$\int_{-1}^{1}d\mu_0\mu_0 b_\pm=\mp\frac{ivk}{3\pi(\omega_+-\omega_-)}. \tag{190}$$

Given equations (169) and (190)

$$\langle\mu_0\mu e^{-ikz}\rangle_2=\frac{\omega_+e^{\omega_+ t}-\omega_-e^{\omega_- t}}{3(\omega_+-\omega_-)}. \tag{191}$$

To determine the expectation value of z, equations (85) and (147) are used to write

$$\langle z\rangle_2=2\pi i\frac{d}{dk}(b_+e^{\omega_+ t}+b_-e^{\omega_- t})\Big|_{k=0}. \tag{192}$$

Which expands to

$$\begin{aligned}\langle z\rangle_2=2\pi i(&e^{\omega_+ t}\frac{d}{dk}b_+ + b_+te^{\omega_+ t}\frac{d}{dk}\omega_+\\ &+e^{\omega_- t}\frac{d}{dk}b_- + b_-te^{\omega_- t}\frac{d}{dk}\omega_-)\Big|_{k=0}.\end{aligned} \tag{193}$$

It can be shown that

$$\frac{d}{dk}\omega_\pm(k=0)=0, \tag{194}$$

and

$$\frac{d}{dk}b_\pm(k=0)=\mp\frac{\mu_0 iv}{4\pi D}, \tag{195}$$

which along with equations (183) and (184) allows an evaluation of equation (193). This evaluates to

$$\langle z\rangle_2 = \frac{\mu_0 v}{2D}(1 - e^{-2Dt}). \tag{196}$$

Now to derive $\langle z^2\rangle_2$ the following must be evaluated,

$$\begin{aligned}\frac{d^2}{dk^2}C_0^*(k,t) = e^{\omega_+ t}\frac{d^2}{dk^2}b_+ + 2\frac{d}{dk}\omega_+\frac{d}{dk}b_+ te^{\omega_+ t} + b_+ t^2 e^{\omega_+ t}\frac{d^2}{dk^2}\omega_+ \\ + e^{\omega_- t}\frac{d^2}{dk^2}b_- + 2\frac{d}{dk}\omega_-\frac{d}{dk}b_- te^{\omega_- t} + b_- t^2 e^{\omega_- t}\frac{d^2}{dk^2}\omega_-\end{aligned} \tag{197}$$

at $k = 0$. To do this one has to consider the following

$$\frac{d^2}{dk^2}\omega_\pm = \mp\frac{v^2}{3D}, \tag{198}$$

and

$$\frac{d^2}{dk^2}b_\pm(k=0) = \pm\frac{v^2}{12\pi D^2}. \tag{199}$$

Now using equations (183), (184), (194), (195), (198), (199) in equation (197) gives

$$\frac{d^2}{dk^2}C_0^* = \frac{v^2}{6\pi D}\left(\frac{1}{2D} - \frac{e^{-2Dt}}{2D} - t\right). \tag{200}$$

By equation (147) it can finally be determined that

$$\langle z^2\rangle_2 = \frac{v^2}{3D}\left(\frac{e^{-2Dt}}{2D} + t - \frac{1}{2D}\right). \tag{201}$$

The limit of $\langle z^2\rangle_2$ as $t \to \infty$ goes to

$$\langle z^2\rangle_2 = \frac{tv^2}{3D}. \tag{202}$$

This matches the expected limit without subspace approximations

$$\langle z^2\rangle = 2\kappa_\parallel t, \tag{203}$$

with

$$\kappa_\parallel = \frac{v^2}{6D}. \tag{204}$$

To determine $\langle e^{-ikz}\rangle_2$ equation (85) must be integrated over μ_0. Since the only μ_0 dependent variables in C_0^* are b_+ and b_-, it is useful to find

$$\int_{-1}^{1} d\mu_0 b_\pm = \mp\int_{-1}^{1} d\mu_0 \frac{(ivk\mu_0 + \omega_\mp)}{2\pi(\omega_+ - \omega_-)}. \tag{205}$$

Since the integral is symmetric the term which is odd in μ_0 vanishes and leaves

$$\int_{-1}^{1} d\mu_0 b_\pm = \mp\frac{\omega_\mp}{\pi(\omega_+ - \omega_-)}. \tag{206}$$

Combining equations (172) and (206) results in

$$\langle e^{-ikz}\rangle_2 = \frac{\omega_+ e^{\omega_- t} - \omega_- e^{\omega_+ t}}{\omega_+ - \omega_-}. \tag{207}$$

Recall again that for the expectation value $\langle \mu\mu_0 e^{-i\vec{k}\cdot\vec{x}}\rangle_2$ there are two models. Using the model $e^{-i\vec{k}_\perp\cdot\vec{x}_\perp} = e^{-\alpha|\mu|}$ requires the use of

$$\int_{-1}^{1} dx x e^{-\alpha|x|} = 0, \quad \textit{and} \tag{208}$$

$$\int_{-1}^{1} dx x^2 e^{-\alpha|x|} = \frac{1}{\alpha^3} e^{\alpha(-2\alpha^2-4\alpha+4e^{\alpha}-4)}. \tag{209}$$

Given these integrals along with equation (206) it can be determined that

$$\langle \mu\mu_0 e^{-i\vec{k}\cdot\vec{x}} \rangle_{2\alpha} = \frac{e^{-\alpha}(-\alpha^2-2\alpha+2e^{\alpha}-2)}{\alpha^3(\omega_+-\omega_-)}(\omega_+ e^{\omega_+ t} - \omega_- e^{\omega_- t}), \tag{210}$$

where the subscript $_{2\alpha}$ has been used to denote the second-order solution using equation (174) as the model. Using the model $e^{-i\vec{k}_\perp\cdot\vec{x}_\perp} = e^{-\beta\mu^2}$ requires the use of

$$\int_{-1}^{1} dx x e^{-\beta x^2} = 0, \tag{211}$$

and

$$\int_{-1}^{1} dx x^2 e^{-\beta x^2} = \frac{\sqrt{\pi} Erf(\sqrt{\beta})}{2\beta^{3/2}} - \frac{e^{-\beta}}{\beta}. \tag{212}$$

Given these new integrals along with equation (206) it can be shown that

$$\langle \mu\mu_0 e^{-i\vec{k}\cdot\vec{x}} \rangle_{2\beta} = \frac{\pi}{2}\left(\frac{Erf(\sqrt{\beta})}{2\sqrt{\pi}\beta^{3/2}} - \frac{e^{-\beta}}{\pi\beta}\right)(\omega_+ e^{\omega_+ t} - \omega_- e^{\omega_- t}), \tag{213}$$

where the subscript $_{2\beta}$ has been used to denote the second-order solution using equation (175) as the model.

2.6.9 Properties of the Third-Order Solution

Given (109) and (110), the expectation value of μ is

$$\langle \mu \rangle_3 = \frac{2\pi}{ivk} \sum_{i=1}^{3} b_i \omega_i e^{\omega_i t}\Big|_{k=0}. \tag{214}$$

In order to evaluate this, equations (131) and (134) are used to show that

$$\langle \mu \rangle_3 = -\frac{-2\pi}{iv}\left(\frac{1}{2\pi}\left(\frac{\omega_1}{k}\right)\Big|_{k=0} - 2De^{-2Dt}\left(\frac{b_2}{k}\right)\Big|_{k=0} - 6De^{-6Dt}\left(\frac{b_3}{k}\right)\Big|_{k=0}\right), \tag{215}$$

which means the limit of ω_1/k, b_2/k, and b_3/k must be evaluated as $k \to 0$. To determine the limit of ω_1/k at $k \to 0$ L'Hôpital's rule can be used. After one use

$$\lim_{k\to 0} \frac{\omega_1}{k} = \lim_{k\to 0} \frac{d\omega_1}{dk}. \tag{216}$$

The derivative $d\omega_1/dk$ is more easily done by symbolic language software. Therefore by using Matlab's *Symbolic Math Toolbox* it is determined that

$$\frac{d\omega_1}{dk}\Big|_{k=0} = 0 = \lim_{k\to 0} \frac{\omega_1}{k}. \tag{217}$$

To determine the limit of $\frac{b_2}{k}$ at $k \to 0$ L'Hôpital's rule can again be used. L'Hôpital's rule shows that

$$\lim_{k\to 0} \frac{b_2}{k} = \lim_{k\to 0} \frac{db_2}{dk}. \tag{218}$$

Again the derivative is calculated using Matlab. It is determined that

$$\lim_{k\to 0} \frac{db_2}{dk} = \frac{1}{4\pi} g(v, D, \mu_0), \tag{219}$$

where $g(v, D, \mu_0)$ is an unknown function that comes from the requirement to do variable transformations to do the numerical work. By proper use of unit analysis it can be shown that

$$g(v, D, \mu_0) = \frac{\mu_0 v}{D}. \tag{220}$$

Therefore

$$\lim_{k\to 0} \frac{b_2}{k} = \frac{\mu_0 v}{4\pi D}. \tag{221}$$

Lastly to determine the limit of $\frac{b_3}{k} = 0$ at $k \to 0$ L'Hôpitals rule is used again to show

$$\lim_{k\to 0} \frac{b_3}{k} = \lim_{k\to 0} \frac{db_3}{dk}. \tag{222}$$

The derivative of which is found as in the past two limits. The final result was determined to be

$$\lim_{k\to 0} \frac{b_3}{k} = 0. \tag{223}$$

By use of the limits (217) through (223) it can finally be shown that

$$\langle \mu \rangle_3 = \mu_0 e^{-2Dt}, \tag{224}$$

which is exactly the same as the second-order result.

To find $\langle \mu^2 \rangle$, recall that for the second-order solution $C_0^{**} = \sum_{i=1}^{3} b_i e^{\omega_i t}$ and

$$C_2^{**} = \frac{-5}{2ivk}(\dot{C}_1 + 2DC_1 + ivkC_0). \tag{225}$$

It has been shown earlier that,

$$C_0^{**}(k=0) = \frac{1}{2\pi}. \tag{226}$$

Also expanding out C_2^{**} gives

$$C_2^{**} = \frac{-15}{v^2k^2}\Big(\sum_{i=1}^{3} b_i\omega_i^2 e^{\omega_i t} + 2D\sum_{i=1}^{3} b_i\omega_i e^{\omega_i t} + (v^2k^2)\sum_{i=1}^{3} b_i e^{\omega_i t}\Big). \tag{227}$$

Taking this equation at the limit $k \to 0$ makes the third term in (227) go to $(v^2k^2)/(6\pi)$ due to (226). Also using the limits (133) and (134) condenses $C_2^{**}(k=0)$ to

$$\begin{aligned} C_2^{**} = \frac{-15}{v^2}\Big(\frac{1}{2\pi}\Big[\frac{\omega_1^2}{k^2}\Big](k=0) + 4D^2e^{-2Dt}\Big[\frac{b_2}{k^2}\Big](k=0) + 36D^2e^{-6Dt}\Big[\frac{b_3}{k^2}\Big](k=0)\Big) + \\ \frac{-30D}{v^2}\Big(\frac{1}{2\pi}\Big[\frac{\omega_1}{k^2}\Big](k=0) - 2De^{-2Dt}\Big[\frac{b_2}{k^2}\Big](k=0) - 6De^{-6Dt}\Big[\frac{b_3}{k^2}\Big](k=0)\Big) - \frac{5}{2\pi}. \end{aligned} \tag{228}$$

Which reduces further to

$$C_2^{**} = \frac{-15}{v^2}\frac{1}{2\pi}\Big[\frac{\omega_1^2}{k^2}\Big](k=0) - 360\frac{D^2}{v^2}e^{-6Dt}\Big[\frac{b_3}{k^2}\Big](k=0) - \frac{15D}{\pi v^2}\Big[\frac{\omega_1}{k^2}\Big](k=0) - \frac{5}{2\pi}. \tag{229}$$

The following three limits are required to further reduce this equation. As $k \to 0$ (ω_1^2/k^2), b_3/k^2, and ω_1/k^2 must be determined. By two uses of L'Hôpital's rule it can be shown that

$$\lim_{k\to 0} \frac{b_3}{k^2} = \lim_{k\to 0} \frac{d^2b_3}{2dk^2}. \tag{230}$$

This derivative was found using Matlab's *Symbolic Math Toolbox* to be

$$\frac{d^2b_3}{2dk^2} = \frac{1}{288\pi} f(v, D). \tag{231}$$

By using unit analysis it was determined that $f(v,D) = v^2/D^2$, therefore

$$\lim_{k\to 0}\frac{b_3}{k^2} = \frac{v^2}{288D^2\pi} \tag{232}$$

Again by using L'Hôpital's rule twice it can be shown that

$$\lim_{k\to 0}\frac{\omega_1^2}{k^2} = \lim_{k\to 0}\left(\left(\frac{d\omega_1}{dk}\right)^2 + \omega_1\frac{d^2\omega_1}{dk^2}\right). \tag{233}$$

These derivatives were again found numerically and the final result

$$\lim_{k\to 0}\frac{\omega_1^2}{k^2} = 0, \tag{234}$$

was found. Lastly by using L'Hôpital's rule twice it can be shown that

$$\lim_{k\to 0}\frac{\omega_1}{k^2} = \lim_{k\to 0}\frac{d^2\omega_1}{2dk^2}. \tag{235}$$

Which numerically was found to be

$$\lim_{k\to 0}\frac{d^2\omega_1}{2dk^2} = \frac{-1}{6}g(v,D), \tag{236}$$

where by unit analysis it was determined that $g(v,d) = v^2/D$. Therefore

$$\lim_{k\to 0}\frac{\omega_1}{k^2} = \frac{-v^2}{6D}. \tag{237}$$

Using equations (233) through (237) in equation (229) gives

$$C_2^{**}(k=0) = \frac{-5}{4\pi}e^{-6Dt}. \tag{238}$$

Which by equation (163), results in

$$\langle\mu^2\rangle_3 = \frac{1}{3}(1-e^{-6Dt}). \tag{239}$$

Furthermore we can calculate the moment,

$$\langle\mu_0\mu e^{-ikz}\rangle_3 = \frac{-\pi}{ivk}\sum_{n=1}^{3}\omega_n e^{\omega_n t}\int_{-1}^{1}d\mu_0\mu_0 b_n. \tag{240}$$

Once again any odd powers of μ_0 will integrate to 0 over the interval -1 to 1 and therefore the integrals over μ_0 can be written as

$$\int_{-1}^{1}d\mu_0\mu_0 b_1 = \int_{-1}^{1}d\mu_0\frac{ivk\mu_0^2(2D+\omega_2+\omega_3)-v^2k^2\mu_0^2}{2\pi(\omega_1-\omega_2)(\omega_1-\omega_3)} = \frac{ivk(2D+\omega_2+\omega_3)-v^2k^2}{3\pi(\omega_1-\omega_2)(\omega_1-\omega_3)}, \tag{241}$$

$$\int_{-1}^{1}d\mu_0\mu_0 b_2 = \int_{-1}^{1}d\mu_0\frac{ivk\mu_0^2(2D+\omega_1+\omega_3)-v^2k^2\mu_0^2}{2\pi(\omega_2-\omega_3)(\omega_2-\omega_1)} = \frac{ivk(2D+\omega_1+\omega_3)-v^2k^2}{3\pi(\omega_2-\omega_3)(\omega_2-\omega_1)}, \tag{242}$$

and

$$\int_{-1}^{1}d\mu_0\mu_0 b_2 = \int_{-1}^{1}d\mu_0\frac{ivk\mu_0^2(2D+\omega_1+\omega_2)-v^2k^2\mu_0^2}{2\pi(\omega_1-\omega_3)(\omega_2-\omega_3)} = \frac{ivk(2D+\omega_1+\omega_2)-v^2k^2}{3\pi(\omega_1-\omega_3)(\omega_2-\omega_3)}. \tag{243}$$

Given equations (241), (242), and (243) it can be shown that the expectation value

$$\begin{aligned}\langle\mu_0\mu e^{-ikz}\rangle_3 = &\frac{\omega_1 e^{\omega_1 t}(2D+\omega_2+\omega_3+ivk)}{3(\omega_1-\omega_2)(\omega_1-\omega_3)}+\\ &\frac{\omega_2 e^{\omega_2 t}(2D+\omega_1+\omega_3+ivk)}{3(\omega_2-\omega_3)(\omega_2-\omega_1)}+\frac{\omega_3 e^{\omega_3 t}(2D+\omega_1+\omega_2+ivk)}{3(\omega_1-\omega_3)(\omega_2-\omega_3)}.\end{aligned} \tag{244}$$

To determine $\langle e^{-ikz}\rangle_3$ equation (98) must be integrated over μ_0. Since the only μ_0 dependent variables in C_0^{**} are $b_{1,2,3}$ it is useful to find

$$\int_{-1}^{1} d\mu_0 b_{1,2,3}. \tag{245}$$

Since the integral is symmetric all terms which are odd in μ_0 vanish and result in the following three equations

$$\int_{-1}^{1} d\mu_0 b_1 = \frac{\omega_2\omega_3}{\pi(\omega_1-\omega_2)(\omega_1-\omega_3)}, \tag{246}$$

$$\int_{-1}^{1} d\mu_0 b_2 = \frac{\omega_1\omega_3}{\pi(\omega_2-\omega_3)(\omega_2-\omega_1)}, \quad and \tag{247}$$

$$\int_{-1}^{1} d\mu_0 b_3 = \frac{\omega_1\omega_2}{\pi(\omega_1-\omega_3)(\omega_2-\omega_3)}. \tag{248}$$

Combining equations (172), (246), (247), and (248) results in

$$\langle e^{-ikz}\rangle_3 = \frac{\omega_2\omega_3 e^{\omega_1 t}}{(\omega_1-\omega_2)(\omega_1-\omega_3)} + \frac{\omega_1\omega_3 e^{\omega_2 t}}{(\omega_2-\omega_3)(\omega_2-\omega_1)} + \frac{\omega_1\omega_2 e^{\omega_3 t}}{(\omega_1-\omega_3)(\omega_2-\omega_3)}. \tag{249}$$

Due to the length of the equations involved $\langle z\rangle_3$, and $\langle z^2\rangle_3$ were not derived analytically for the third-order solution. However they were numerically calculated by using equation (147) for plotting and comparison purposes. Figure (42) compares the analytic solutions for $<\mu>$ for all orders of solutions as well as the numerical solution. Figure (43) compares the analytic solutions for $<z>$ for all orders as well as the numerical solution. Figure (44) compares the analytic solutions for $<z^2>$ for all orders of solutions as well as the numerical solution. At early times there is a discrepancy between the numerical and analytic solutions. This is due to the finite width Gaussian distribution used as an initial condition for the numerical solution. Due to this finite width Gaussian the numerical solution has a non-zero $\langle z^2\rangle$ at time $t = 0$.

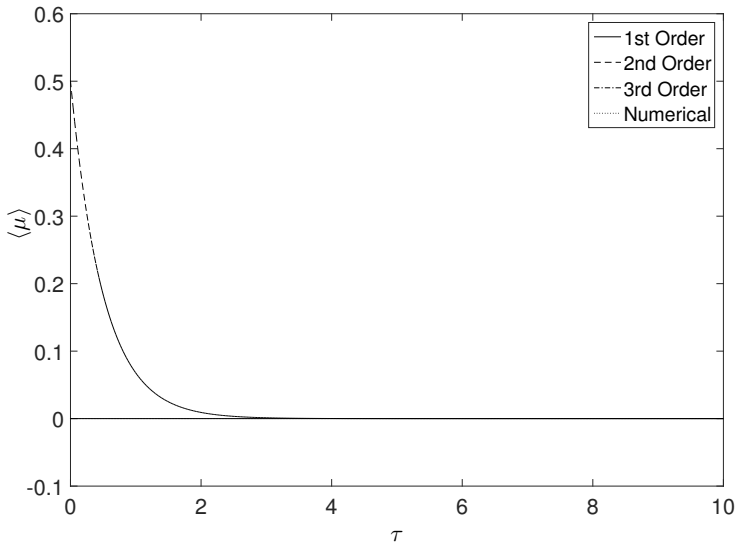

Figure 42: The moment $\langle\mu\rangle$ of equation (61). The first-order solution is given by the dashed-dotted line, the second-order solution is given by the dashed line, the third-order solution is given by the solid line, and the numerical solution is given by the dotted line. The second-order solution, the third-order solution and the numerical results are all in coincidence.

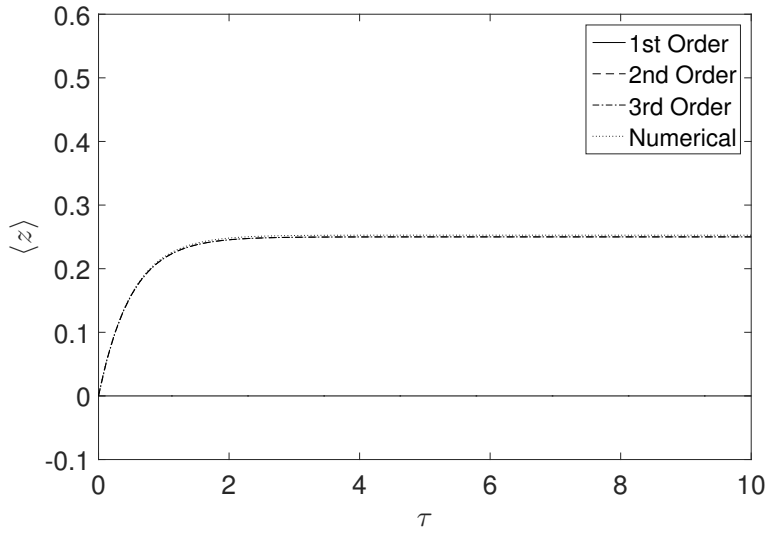

Figure 43: The moment $\langle z \rangle$ of equation (61). The first-order solution is given by the dashed-dotted line, the second-order solution is given by the dashed line, the third-order solution is given by the solid line, and the numerical solution is given by the dotted line. The second-order solution, the third-order solution, and the numerical solution are all in coincidence.

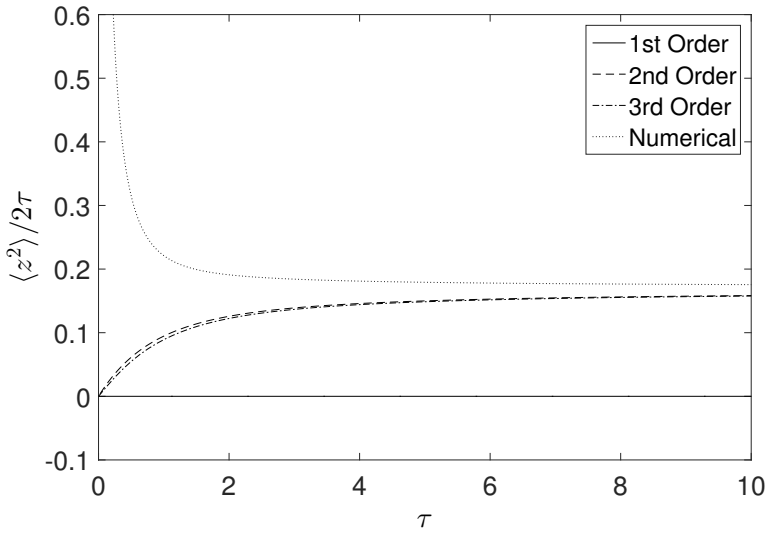

Figure 44: The moment $\langle z^2 \rangle$ of equation (61). The first-order solution is given by the dashed-dotted line, the second-order solution is given by the dashed line, the third-order solution is given by the solid line, and the numerical solution is given by the dotted line. The second-order solution, the third-order solution, and the numerical solution are all in coincidence.

2.6.10 Integrated Solutions

Looking at surface plots to compare each solution can be difficult. It is arguably better to use two dimensional plots to show comparisons. For that purpose each solution was integrated over first its μ domain, and then separately its z domain. These μ- and z-integrated solutions are plotted against each other for times $\tau = 0$, $\tau = 0.2$, and $\tau = 10$. They show that at late times there is no significant difference between second and third-order results, and at early times it is difficult to determine validity of the solutions due to the Gaussian initial conditions of the numerical solution.

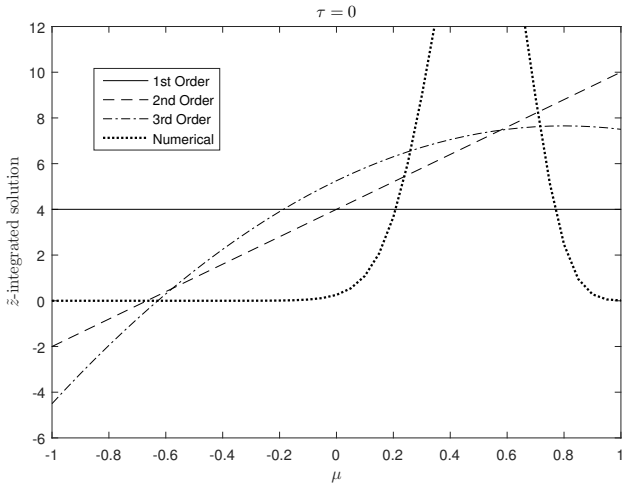

Figure 45: The z-integrated numerical solution to equation (61) for the time $\tau = 0$. The first-order solution is given by the dashed-dotted line, the second-order solution is given by the dashed line, the third-order solution is given by the solid line, and the numerical solution is given by the dotted line.

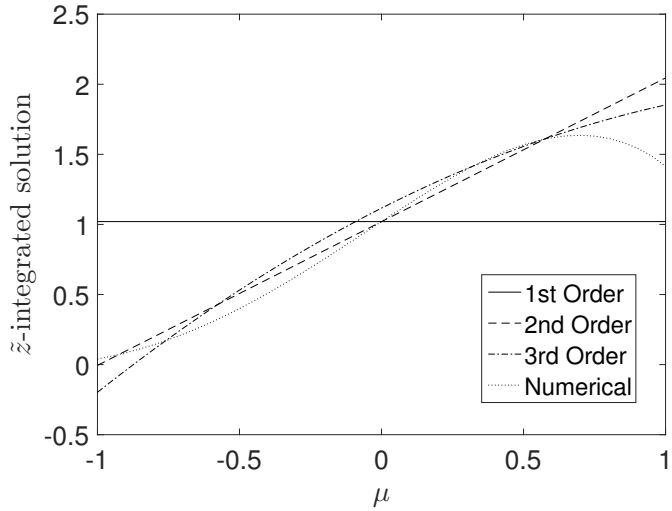

Figure 46: The z-integrated numerical solution to equation (61) for the time $\tau = 0.2$. The first-order solution is given by the dashed-dotted line, the second-order solution is given by the dashed line, the third-order solution is given by the solid line, and the numerical solution is given by the dotted line.

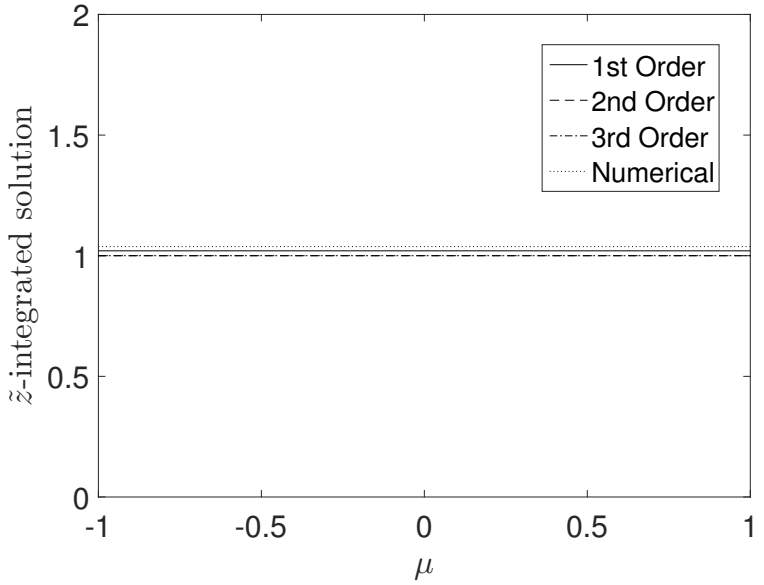

Figure 47: The z-integrated numerical solution to equation (61) for the time $\tau = 10$. The first-order solution is given by the dashed-dotted line, the second-order solution is given by the dashed line, the third-order solution is given by the solid line, and the numerical solution is given by the dotted line. The second and third-order solutions are in coincidence with each other.

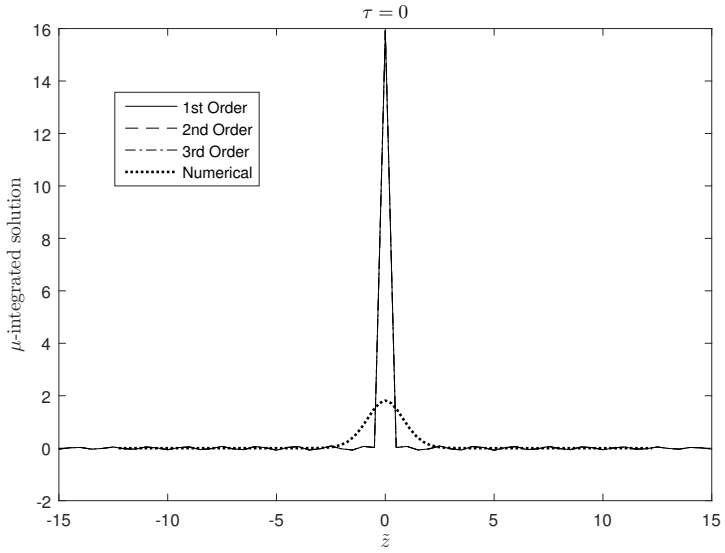

Figure 48: The μ-integrated numerical solution to equation (61) for the time $\tau = 0$. The first-order solution is given by the dashed-dotted line, the second-order solution is given by the dashed line, the third-order solution is given by the solid line, and the numerical solution is given by the dotted line. The first, second, and third-order solutions are all in coincidence with each other.

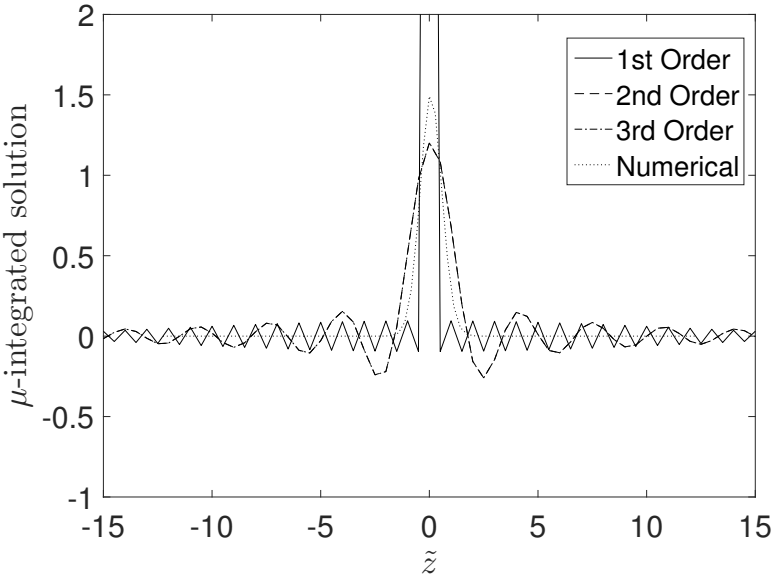

Figure 49: The μ-integrated numerical solution to equation (61) for the time $\tau = 0.2$. The first-order solution is given by the dashed-dotted line, the second-order solution is given by the dashed line, the third-order solution is given by the solid line, and the numerical solution is given by the dotted line. The second and third-order solutions are in coincidence with each other.

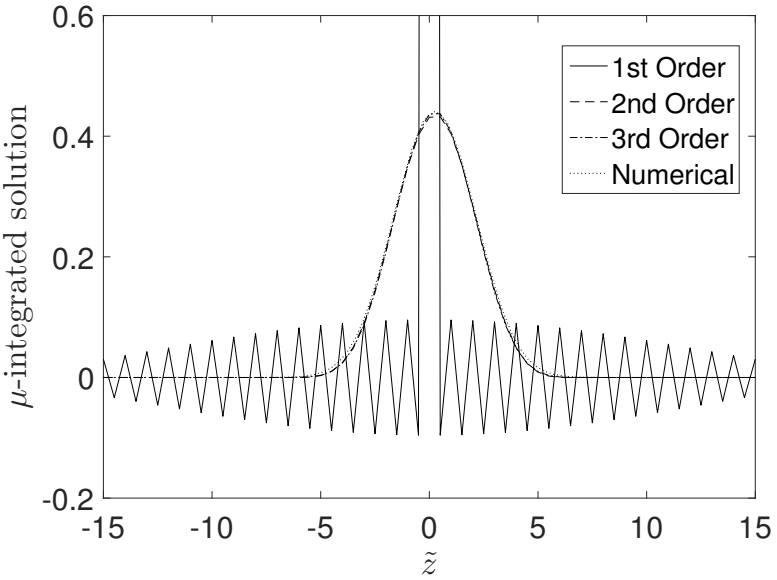

Figure 50: The μ-integrated numerical solution to equation (61) for the time $\tau = 10$. The first-order solution is given by the dashed-dotted line, the second-order solution is given by the dashed line, the third-order solution is given by the solid line, and the numerical solution is given by the dotted line. The second-order, third-order, and numerical solutions are all in coincidence with each other.

3 The Unified Non Linear Transport Theory

3.1 Diffusive UNLT Theory

In the following perpendicular transport of energetic particles is discussed. Parallel transport can be adequately described by quasi-linear theory (see Jokipii (1966)) and extensions thereof (see Shalchi (2005)). However, perpendicular transport requires a non-linear theory to accurately describe particle trajectories. In 2010 A. Shalchi developed the "unified non linear transport theory" (UNLT theory) which was more general than any theory developed previously in that it worked for arbitrary turbulence models (see Shalchi (2010)). The basis of this theory is the Taylor-Green-Kubo (TGK) formulation of how to determine the perpendicular scattering coefficient (see Taylor (1922), Green (1951), Kubo (1957)),

$$\kappa_\perp = \Re \int_0^\infty dt \langle v_x(0) v_x(t) \rangle. \tag{250}$$

Shalchi assumes both axis-symmetric and homogeneous turbulence, then uses two approximations. The Corrsin approximation (see Corrsin (1959)). With these tools, in Shalchi (2010), Shalchi manipulates the Fokker-Planck equation to find the following relation without having to actually solve the Fokker-Planck equation,

$$\kappa_\perp = \frac{a^2 v^2}{3B_0^2} \int d^3k \frac{P_{xx}}{A(\vec{k}) + (4/3)\kappa_\perp k_\perp^2 + v/\lambda_\parallel}, \tag{251}$$

where $k_\perp$ and $k_\parallel$ are wave numbers in Fourier space, $\lambda_\parallel$ is the parallel mean free path defined by $\lambda_\parallel = 3\kappa_\parallel/v$, a is a coefficient that comes as a correction factor to match simulations (often it is set to either 1 or $1/\sqrt{3}$), $P_{xx}(\vec{k})$ is the xx-component of the magnetic correlation tensor, and lastly $A(\vec{k})$ is defined as

$$A(\vec{k}) = \frac{(vk_\parallel)^2}{3\kappa_\perp k_\perp^2}. \tag{252}$$

Also note that the integral cannot be directly solved, this is an integral equation in $\kappa_\perp$. Not all of the intricacies in this equation (251) are required knowledge to understand the research done in this thesis. Special attention should be paid to the magnetic turbulence model P_{xx} and to the dependency on the parallel mean free path $\lambda_\parallel$. This work done in 2010 is a limiting case of the more recent and more general theory, namely time dependent UNLT theory.

3.2 Time Dependent UNLT Theory

In 2017 A. Shalchi developed a fully time dependent version of UNLT theory (see Shalchi (2017)). In Shalchi (2017) it is derived directly from the basic equations of motion (2), using fewer assumptions than the time-independent UNLT theory derivation. With turbulent magnetic fields these equations of motion are shown in section 1.7 as equation (8). They can also be written as

$$\begin{aligned} \dot{v}_x &= \Omega v_y + b_y \\ \dot{v}_y &= \Omega v_x + b_x, \end{aligned} \tag{253}$$

where

$$\begin{aligned} b_x &= \Omega \left(v_z \frac{\delta B_x}{B_0} - v_x \frac{\delta B_z}{B_0} \right) \\ b_y &= \Omega \left(v_y \frac{\delta B_z}{B_0} - v_z \frac{\delta B_y}{B_0} \right). \end{aligned} \tag{254}$$

By using the guiding center co-ordinate transformation $\vec{X} = \vec{x} + (\vec{v} \times \vec{e}_z)/\Omega$, these equations can be written as

$$\begin{aligned} V_x = \frac{b_x}{\Omega} &= v_z \frac{\delta B_x(\vec{x})}{B_0} - v_x \frac{\delta B_z(\vec{x})}{B_0} \\ V_y = \frac{b_y}{\Omega} &= v_z \frac{\delta B_y(\vec{x})}{B_0} - v_y \frac{\delta B_z(\vec{x})}{B_0}. \end{aligned} \tag{255}$$

This reduces to

$$V_x = v_z \frac{\delta B_x(\vec{x})}{B_0}$$
$$V_y = v_z \frac{\delta B_y(\vec{x})}{B_0}, \tag{256}$$

for $\delta B_z = 0$. The magnetic field is then written in Fourier space, and the equation of motion for V_x is shown in Shalchi (2017) to be

$$V_x(t) = \frac{1}{B_0} \int d^3k \delta B_x(\vec{k}) \frac{1}{ik_\parallel} \Big(\frac{d}{dt} e^{izk_\parallel} \Big) e^{i\vec{x}_\perp \cdot \vec{k}_\perp} \tag{257}$$

An equation for V_y can similarly be written but is not necessary. This is because, due to symmetry the perpendicular diffusion coefficient can be found using only equation (257). A few approximations are then used. As previously the Corrsin approximation is used (see Corrsin (1959)), this assumes that the magnetic fields and the phases are not correlated. Again as well, turbulence is assumed to be homogeneous and axis-symmetric, and lastly the hypothesis

$$\langle exp[i\vec{x} \cdot \vec{k}] \rangle \approx \langle exp[izk_\parallel] \rangle \langle exp[i\vec{x}_\perp \cdot \vec{k}_\perp] \rangle \tag{258}$$

was used. Given $\vec{x}_\perp(t=0) = 0$, the velocity auto-correlation function can then be written as

$$\langle V_x(t) V_x(0) \rangle = \frac{1}{B_0^2} \int d^3k P_{xx}(\vec{k}) \xi(t,0) \langle e^{i\vec{x}_\perp \cdot \vec{k}_\perp} \rangle, \tag{259}$$

where

$$\xi(t_1, t_2) = \frac{1}{k_\parallel^2} \Big\langle \Big(\frac{d}{dt_1} e^{iz(t_1)k_\parallel} \Big) \Big(\frac{d}{dt_2} e^{iz(t_2)k_\parallel} \Big) \Big\rangle. \tag{260}$$

Note that in this section the parameter a has been fixed at $a = 1$ so it does not appear in the equations. This is often done, because a is always constant in a system and its correct value is argued about. By calculating the derivatives and using $z(0) = 0$ the parallel correlation function ξ can alternatively be written as

$$\xi(t_1, t_2) = \frac{1}{k_\parallel^2} \frac{d}{dt_1} \frac{d}{dt_2} \langle e^{i|z(t_1) - z(t_2)|k_\parallel} \rangle. \tag{261}$$

Recall the TGK formulation, equation (250), relates the perpendicular diffusion coefficient to the velocity auto-correlation function. This time however, it is shown in its more general form, which allows for a non-vanishing initial diffusion coefficient.

$$\kappa_\perp(t) = \kappa_\perp(0) + \Re \int_0^\infty dt \langle v_x(0) v_x(t) \rangle. \tag{262}$$

Since the diffusion coefficient $\kappa_\perp$ is defined as

$$\kappa_\perp = \frac{d\langle (\Delta x)^2 \rangle}{2dt}, \tag{263}$$

equation (259) can be plugged into equation (262) to show

$$\frac{d^2}{dt^2} \langle (\Delta x)^2 \rangle = \frac{2}{B_0^2} \int d^3k P_{xx}(\vec{k}) \xi(t,0) e^{-\frac{1}{2}\langle (\Delta x)^2 \rangle k_\perp^2}. \tag{264}$$

This equation is the important result in Shalchi's time dependent UNLT theory. Time dependent UNLT theory can be shown to be consistent with time independent UNLT theory as a special case. To show this first the function ξ must be determined. In Shalchi *et al.* (2011) it was derived, using a two-dimensional subspace approximation like the one used in section 2.6.3, that

$$\xi(k_\parallel, t) = \frac{v^2}{3} \frac{1}{\omega_{+\xi} - \omega_{-\xi}} (\omega_{+\xi} e^{\omega_{+\xi} t} - \omega_{-\xi} e^{\omega_{-\xi} t}). \tag{265}$$

The parameters $\omega_{+\xi}$ and $\omega_{-\xi}$ are given by

$$\omega_{\pm\xi} = -D \pm \sqrt{D^2 - (vk_\parallel)^2/3} = -\frac{v}{2\lambda_\parallel} \pm \sqrt{\left(\frac{v}{2\lambda_\parallel}\right)^2 - (vk_\parallel)^2/3}. \tag{266}$$

Note that equation (265) is exactly the velocity correlation function (191), as found in section 2.6.3, with the factor v^2 in front. This is because the same Legendre polynomial expansion was used in Shalchi *et al.* (2011). The eigenvalues (266), are of course also the same as the eigenvalues (87). Next diffusion is assumed

$$e^{-\frac{1}{2}\langle(\Delta x)^2\rangle k_\perp^2} = e^{-\kappa_\perp k_\perp^2 t}. \tag{267}$$

Integrating over all time and plugging equations (267) and (263) into equation (264) gives

$$\kappa_\perp = \frac{1}{B_0}\int d^3k P_{xx} \int_0^\infty dt\xi e^{-\kappa_\perp k_\perp^2 t}. \tag{268}$$

Which after solving the time integral by using equations (265) and (266) becomes

$$\kappa_\perp = \frac{v^2}{3B_0}\int d^3k \frac{P_{xx}}{\kappa_\perp k_\perp^2 + \frac{v}{\lambda_\parallel} + \frac{(vk_\parallel)^2}{3\kappa_\perp k_\perp^2}}. \tag{269}$$

This is exactly time independent UNLT theory with $a = 1$.

3.3 Turbulence Models

In time dependent UNLT theory the ODE describing the perpendicular diffusion coefficient (264) can only be solved once a model for the turbulence has been defined. In this work four common turbulence models are used to solve for the diffusion coefficient. The results of each model are compared to each other as well as to themselves for different values of the parallel mean free path $\lambda_\parallel/\ell$. In this work the subspace approximation of ξ, (265), is used. Turbulence models with perpendicular complexity are required for diffusion (rather than sub-diffusion) and therefore the four turbulence models studied were noisy slab, Gaussian correlation, two dimensional, and two-component turbulence. The latter being a model which combines both slab and two dimensional turbulence. None of these are new turbulence models, they all have been used in past research; this is the first time they were used with the most general and most recent theory, namely time dependent UNLT theory.

3.3.1 Noisy Slab Turbulence

Noisy slab turbulence is a turbulence model first studied in Shalchi (2015). It has only a small amount of transverse structure, and can be used to study what effects even minimal transverse turbulence has on particle trajectories. It is defined as

$$P_{nm}(\vec{k}) = \frac{2\ell_\perp}{k_\perp} g^{slab}(k_\parallel)\Theta(1 - k_\perp\ell_\perp)\left(\delta_{nm} - \frac{k_n k_m}{k_\perp^2}\right), \tag{270}$$

where Θ is the Heaviside step function. For this turbulence model equation (264) becomes

$$\begin{aligned}\frac{d^2}{dt^2}\langle(\Delta x)^2\rangle &= \frac{8\pi v^2\ell_\perp}{3B_0^2}\int_0^\infty dk_\parallel g^{slab}(k_\parallel)\frac{1}{\omega_{+\xi}-\omega_{-\xi}}(\omega_{+\xi}e^{\omega_{+\xi}t} - \omega_{-\xi}e^{\omega_{-\xi}t}) \\ &\times \int_0^{1/\ell_\perp} dk_\perp e^{-\frac{1}{2}\langle(\Delta x)^2\rangle k_\perp^2},\end{aligned} \tag{271}$$

where the wave number integral has been split into its parallel and perpendicular components. The latter component can be solved by using an error function. Therefore

$$\begin{aligned}\frac{d^2}{dt^2}\langle(\Delta x)^2\rangle &= \frac{8\pi v^2\ell_\perp}{3B_0^2}\sqrt{\frac{\pi}{2\langle(\Delta x)^2\rangle}}Erf\left(\sqrt{\frac{\langle(\Delta x)^2\rangle}{2\ell_\parallel^2}}\right) \\ &\times \int_0^\infty dk_\parallel g^{slab}(k_\parallel)\frac{1}{\omega_{+\xi}-\omega_{-\xi}}(\omega_{+\xi}e^{\omega_{+\xi}t} - \omega_{-\xi}e^{\omega_{-\xi}t}).\end{aligned} \tag{272}$$

The spectrum of the magnetic turbulence model, $g^{slab}(k_\parallel)$, was modeled in Bieber *et al.* (1994) as

$$g^{slab}(k_\parallel) = \frac{1}{2\pi} C(s)\delta B^2 \ell_\parallel \frac{1}{\left(1+(k_\parallel \ell_\parallel)^2\right)^{s/2}}, \tag{273}$$

where $C(s)$ is a normalization function given by

$$C(s) = \frac{\Gamma(s/2)}{2\sqrt{\pi}\,\Gamma(\frac{s-1}{2})}. \tag{274}$$

It should be noted that in this work the inertial spectral index s is set to $s = 5/3$. This is most commonly used as was shown to be a valid choice of spectral index in Kolmogorov (1941). In order to solve this equation numerically the following transformations are used.

$$z = \ell_\parallel k_\parallel, \tag{275}$$

$$K = \frac{\ell_\parallel \delta B_x}{\ell_\perp B_0}, \tag{276}$$

$$\tau = \frac{\kappa_\parallel t}{\ell_\parallel^2}, \tag{277}$$

$$\Omega_\pm = \frac{\ell_\parallel^2}{\kappa_\parallel^2}\omega_{\pm\xi} = \frac{3\ell_\parallel}{2\lambda_\parallel}\left(-\frac{\ell_\parallel}{\lambda_\parallel} \pm \sqrt{\frac{\ell_\parallel^2}{\lambda_\parallel^2} - \frac{4}{3}z^2}\right), \tag{278}$$

and

$$\sigma = \frac{\langle(\Delta x)^2\rangle}{\ell_\perp^2}. \tag{279}$$

It should be noted that the parameter K is commonly used in this field and is referred to as the Kubo number. With these transformations and the magnetic spectrum model

$$\frac{d^2\sigma}{dt^2} = 12\sqrt{\pi}K^2 C(s)\frac{\ell_\parallel^2}{\lambda_\parallel^2}\sqrt{\frac{2}{\sigma}}Erf\left(\sqrt{\frac{\sigma}{2}}\right)\int_0^\infty dz(1+z^2)^{-s/2}\frac{1}{\Omega_{+\xi}-\Omega_-}(\Omega_+ e^{\Omega_+ t} - \Omega_- e^{\Omega_- t}). \tag{280}$$

Equation (280) was solved numerically by methods discussed in further detail in section 3.3.5. To solve the ODE numerically the following initial conditions were used,

$$\sigma(0) = 0, \tag{281}$$

and

$$\frac{d\sigma}{d\tau}(0) = 0. \tag{282}$$

These initial conditions correspond to ballistic motion. Figures (51), and (52) show the solutions to equation (280) for Kubo numbers $K = 0.2$, and $K = 0.7$. The solutions are shown specifically as

$$D_\perp = \frac{\ell_\parallel^2}{2\kappa_\parallel}\frac{d\sigma}{dt}, \tag{283}$$

as a function of τ, and for varying values of the parallel mean free path $\lambda_\parallel/\ell_\parallel$.

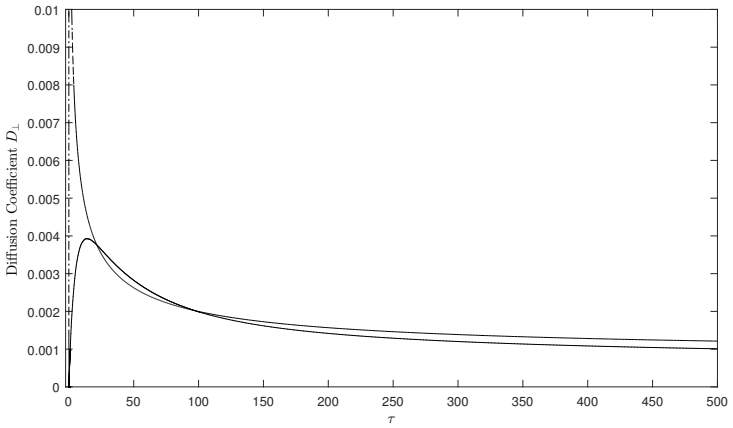

Figure 51: The running diffusion coefficient ratio $D_\perp = (\ell_\parallel^2 \kappa_\perp)/(\ell_\perp^2 \kappa_\parallel)$, plotted vs transformed time $\tau = \kappa_\parallel t/\ell_\parallel^2$, obtained by solving equation (280), for the noisy slab turbulence model and a Kubo number $K = 0.2$. Separate lines are shown for varying values of the parallel mean free path, specifically $\lambda_\parallel/\ell_\parallel = 0.01$ (dotted line), $\lambda_\parallel/\ell_\parallel = 0.1$ (dashed-dotted line), $\lambda_\parallel/\ell_\parallel = 1$ (dashed line), and $\lambda_\parallel/\ell_\parallel = 10$ (solid line). Here the former three lines are all in coincidence.

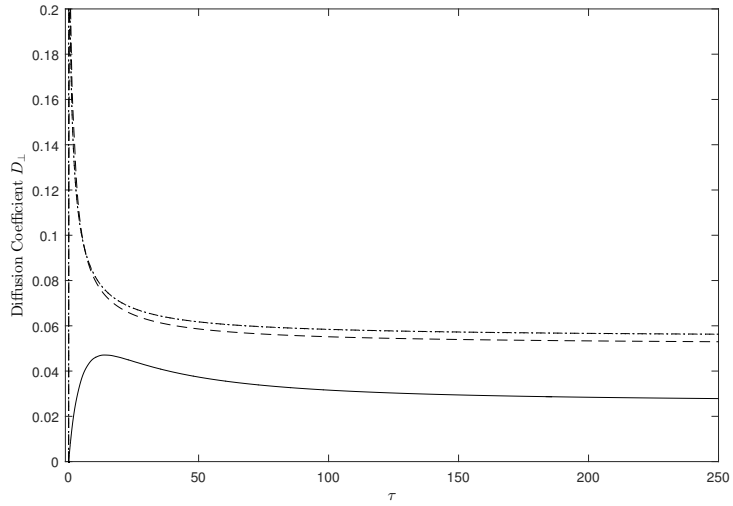

Figure 52: The running diffusion coefficient ratio $D_\perp = (\ell_\parallel^2 \kappa_\perp)/(\ell_\perp^2 \kappa_\parallel)$, plotted vs transformed time $\tau = \kappa_\parallel t/\ell_\parallel^2$, obtained by solving equation (280), for the noisy slab turbulence model and a Kubo number $K = 0.7$. Separate lines are shown for varying values of the parallel mean free path, specifically $\lambda_\parallel/\ell_\parallel = 0.01$ (dotted line), $\lambda_\parallel/\ell_\parallel = 0.1$ (dashed-dotted line), $\lambda_\parallel/\ell_\parallel = 1$ (dashed line), and $\lambda_\parallel/\ell_\parallel = 10$ (solid line). Here the former two lines are in coincidence.

3.3.2 Gaussian Correlation Model

Gaussian correlation is a commonly used turbulence model with transverse complexity. It is used for instance in Neuer & Spatschek (2006). In this model the magnetic correlation tensor is

$$P_{nm}(\vec{k}) = \frac{\ell_\parallel \ell_\perp^4 \delta B_x^2 k_\perp^2}{(2\pi)^{3/2}} e^{-\frac{1}{2}(\ell_\parallel k_\parallel)^2 - \frac{1}{2}(\ell_\perp k_\perp)^2} \left(\delta_{nm} - \frac{k_n k_m}{k_\perp^2}\right). \tag{284}$$

Plugging the magnetic correlation into equation (264), and splitting up the wave number integral into parallel and perpendicular components gives

$$\frac{d^2}{dt^2}\langle(\Delta x)^2\rangle = \frac{2\ell_\parallel \ell_\perp^4}{\sqrt{2\pi}} \frac{\delta B_x^2}{B_0^2} \int_0^\infty dk_\parallel \xi(k_\parallel, t) e^{-(\ell_\parallel k_\parallel)^2/2} \int_0^\infty dk_\perp k_\perp^3 e^{-k_\perp^2(\ell_\perp^2 + \langle(\Delta x)^2\rangle)/2}. \tag{285}$$

The latter integral in equation (285) is solved as

$$\int_0^\infty dk_\perp k_\perp^3 e^{-k_\perp^2(\ell_\perp^2 + \langle(\Delta x)^2\rangle)/2} = \frac{2}{(\ell_\perp^2 + \langle(\Delta x)^2\rangle)^2}, \tag{286}$$

which results in

$$\frac{d^2}{dt^2}\langle(\Delta x)^2\rangle = \frac{\sqrt{8}\ell_\parallel \ell_\perp^4}{\sqrt{\pi}} \frac{\delta B_x^2}{B_0^2} \frac{1}{(\ell_\perp^2 + \langle(\Delta x)^2\rangle)^2} \int_0^\infty dk_\parallel \xi(k_\parallel, t) e^{-(\ell_\parallel k_\parallel)^2/2}. \tag{287}$$

Again equations (265) and (266), as well as transformations (275) - (279) are used. After some algebra the resultant ODE is

$$\frac{d^2\sigma}{d\tau^2} = 6\sqrt{\frac{2}{\pi}} \frac{\ell_\parallel^2 K^2}{\lambda_\parallel^2 (1+\sigma)^2} \int_0^\infty dz \frac{1}{(\Omega_+ - \Omega_-)} (\Omega_+ e^{\Omega_+ \tau} - \Omega_- e^{\Omega_- \tau}) e^{-z^2/2}. \tag{288}$$

Again ballistic motion initial conditions (281) and (282) are used and equation (288) is solved numerically. The results for Kubo numbers of $K = 0.2$ and $K = 2$ and for varying values of $\lambda_\parallel/\ell_\parallel$ are shown in figures (53) and (54).

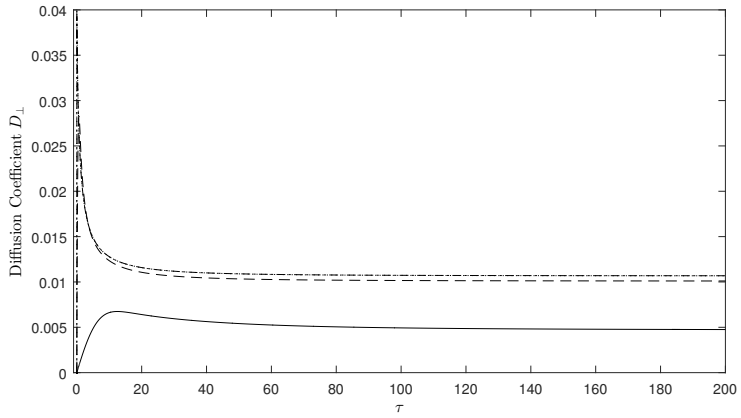

Figure 53: The running diffusion coefficient ratio $D_\perp = (\ell_\parallel^2 \kappa_\perp)/(\ell_\perp^2 \kappa_\parallel)$, plotted vs transformed time $\tau = \kappa_\parallel t/\ell_\parallel^2$, obtained by solving equation (288), for the Gaussian correlation turbulence model and a Kubo number $K = 0.2$. Separate lines are shown for varying values of the parallel mean free path, specifically $\lambda_\parallel/\ell_\parallel = 0.01$ (dotted line), $\lambda_\parallel/\ell_\parallel = 0.1$ (dashed-dotted line), $\lambda_\parallel/\ell_\parallel = 1$ (dashed line), and $\lambda_\parallel/\ell_\parallel = 10$ (solid line). Here the former two lines are in coincidence.

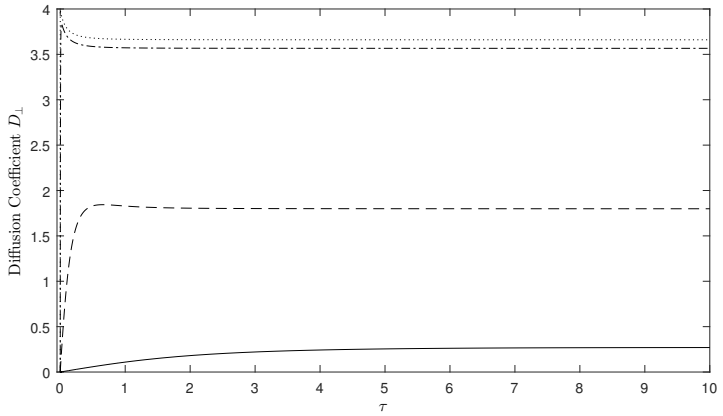

Figure 54: The running diffusion coefficient ratio $D_\perp = (\ell_\parallel^2 \kappa_\perp)/(\ell_\perp^2 \kappa_\parallel)$, plotted vs transformed time $\tau = \kappa_\parallel t/\ell_\parallel^2$, obtained by solving equation (280), for the Gaussian correlation turbulence model and a Kubo number $K = 2$. Separate lines are shown for varying values of the parallel mean free path, specifically $\lambda_\parallel/\ell_\parallel = 0.01$ (dotted line), $\lambda_\parallel/\ell_\parallel = 0.1$ (dashed-dotted line), $\lambda_\parallel/\ell_\parallel = 1$ (dashed line), and $\lambda_\parallel/\ell_\parallel = 10$ (solid line).

3.3.3 2D Turbulence

Where as the slab model has only parallel turbulence components, and the noisy slab model has minimal perpendicular turbulence, the two dimensional turbulence model is a model with only perpendicular turbulence components, i.e. $\delta\vec{B} = \delta\vec{B}(x, y)$. It has the following magnetic correlation tensor components.

$$P_{nm}(\vec{k}) = g^{2D}(k_\perp)\frac{\delta(k_\parallel)}{k_\perp}\left(\delta_{nm} - \frac{k_n k_m}{k_\perp^2}\right), \tag{289}$$

where the spectrum g^{2D} is modeled, as in Shalchi & Weinhorst (2009), namely

$$g^{2D}(k_\perp) = \frac{2D(s,q)\delta B_{2D}^2 \ell_\perp}{\pi}\frac{(k_\perp \ell_\perp)^q}{(1 + k_\perp^2 \ell_\perp^2)^{(s+q)/2}}, \tag{290}$$

where $\ell_\perp$ is the slab bendover scale, a characteristic length scale. The function $D(s, q)$ is a normalization function given by

$$D(s,q) = \frac{\Gamma((s+q)/2)}{2\Gamma(\frac{s-1}{2})\Gamma(\frac{q+1}{2})}. \tag{291}$$

where q is the so called energy range spectral index. Plugging equation (289) into (264), gives

$$\frac{d^2}{dt^2}\langle(\Delta x)^2\rangle = \frac{2\pi}{B_0^2}\int_0^\infty dk_\perp g^{2D}(k_\perp)e^{-k_\perp^2\langle(\Delta x)^2\rangle/2}\int_0^\infty dk_\parallel \xi(k_\parallel, t)\delta(k_\parallel), \tag{292}$$

which by use of the Dirac delta function $\delta(k_\parallel)$ becomes

$$\frac{d^2}{dt^2}\langle(\Delta x)^2\rangle = \frac{2\pi}{B_0^2}\int_0^\infty dk_\perp g^{2D}(k_\perp)e^{-k_\perp^2\langle(\Delta x)^2\rangle/2}\xi(0, t). \tag{293}$$

Evaluating $\xi(k_\parallel = 0)$ gives

$$\xi(k_\parallel = 0, t) = \frac{v^2}{3}e^{-vt/\lambda_\parallel}, \tag{294}$$

therefore

$$\frac{d^2}{dt^2}\langle(\Delta x)^2\rangle = \frac{2\pi v^2}{3B_0^2}\int_0^\infty dk_\perp g^{2D}(k_\perp)e^{-vt/\lambda_\parallel - k_\perp^2\langle(\Delta x)^2\rangle/2}. \tag{295}$$

Plugging in the spectrum (290) and using the transformation $z = k_\perp \ell_\perp$ results in

$$\frac{d^2}{dt^2}\langle(\Delta x)^2\rangle = \frac{4v^2 D(s,q)\delta B_{2D}^2}{3B_0^2} e^{-vt/\lambda_\parallel} \int_0^\infty dz \frac{z^q}{(1+z^2)^{(s+q)/2}} e^{-z^2\langle(\Delta x)^2\rangle/(2\ell_\perp^2)}. \tag{296}$$

Finally this equation can be transformed for numerical work by use of (277), (276), and (279). The resulting ODE is

$$\frac{d^2\sigma}{dt^2} = 24 D(s,q) \frac{\ell_\parallel^2}{\lambda_\parallel^2} K^2 e^{(-3\tau\ell_\parallel^2/\lambda_\parallel^2)} \int_0^\infty dz \frac{z^q}{(1+z^2)^{(s+q)/2}} e^{-\sigma z^2/2}. \tag{297}$$

Again ballistic initial conditions (281) and (282) are used and equation (297) is solved numerically. The results for Kubo numbers of $K = 0.7$ and $K = 2$, energy range spectral indices of $q = 1.5$ and $q = 3$, and for varying values of $\lambda_\parallel/\ell_\parallel$ are shown in figures (55), through (58).

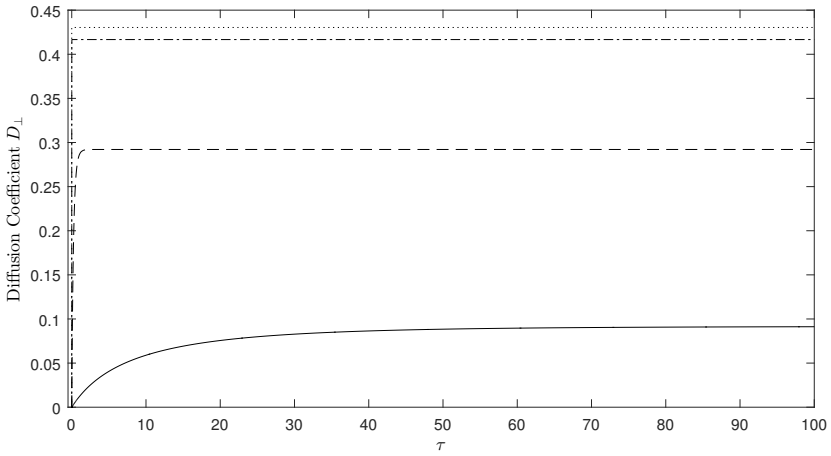

Figure 55: The running diffusion coefficient ratio $D_\perp = (\ell_\parallel^2\kappa_\perp)/(\ell_\perp^2\kappa_\parallel)$, plotted vs transformed time $\tau = \kappa_\parallel t/\ell_\parallel^2$, obtained by solving equation (297), for the 2D turbulence model. Here a Kubo number of $K = 0.7$ and a energy range spectral index of $q = 1.5$ has been used. Separate lines are shown for varying values of the parallel mean free path, specifically $\lambda_\parallel/\ell_\parallel = 0.01$ (dotted line), $\lambda_\parallel/\ell_\parallel = 0.1$ (dashed-dotted line), $\lambda_\parallel/\ell_\parallel = 1$ (dashed line), and $\lambda_\parallel/\ell_\parallel = 10$ (solid line).

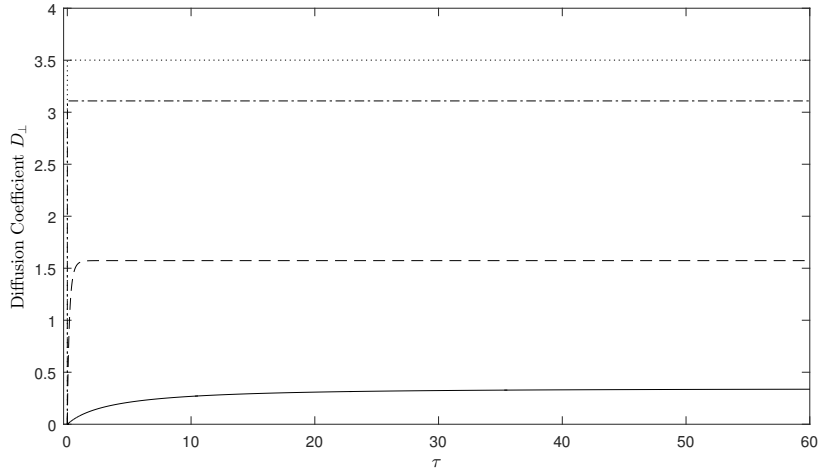

Figure 56: The running diffusion coefficient ratio $D_\perp = (\ell_\parallel^2 \kappa_\perp)/(\ell_\perp^2 \kappa_\parallel)$, plotted vs transformed time $\tau = \kappa_\parallel t/\ell_\parallel^2$, obtained by solving equation (297), for the 2D turbulence model. Here a Kubo number of $K = 2$ and a energy range spectral index of $q = 1.5$ has been used. Separate lines are shown for varying values of the parallel mean free path, specifically $\lambda_\parallel/\ell_\parallel = 0.01$ (dotted line), $\lambda_\parallel/\ell_\parallel = 0.1$ (dashed-dotted line), $\lambda_\parallel/\ell_\parallel = 1$ (dashed line), and $\lambda_\parallel/\ell_\parallel = 10$ (solid line).

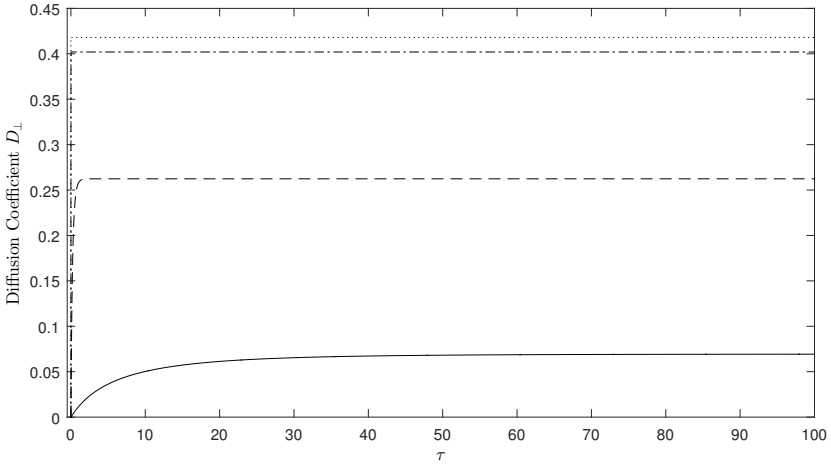

Figure 57: The running diffusion coefficient ratio $D_\perp = (\ell_\parallel^2 \kappa_\perp)/(\ell_\perp^2 \kappa_\parallel)$, plotted vs transformed time $\tau = \kappa_\parallel t/\ell_\parallel^2$, obtained by solving equation (297), for the 2D turbulence model. Here a Kubo number of $K = 0.7$ and a energy range spectral index of $q = 3$ has been used. Separate lines are shown for varying values of the parallel mean free path, specifically $\lambda_\parallel/\ell_\parallel = 0.01$ (dotted line), $\lambda_\parallel/\ell_\parallel = 0.1$ (dashed-dotted line), $\lambda_\parallel/\ell_\parallel = 1$ (dashed line), and $\lambda_\parallel/\ell_\parallel = 10$ (solid line).

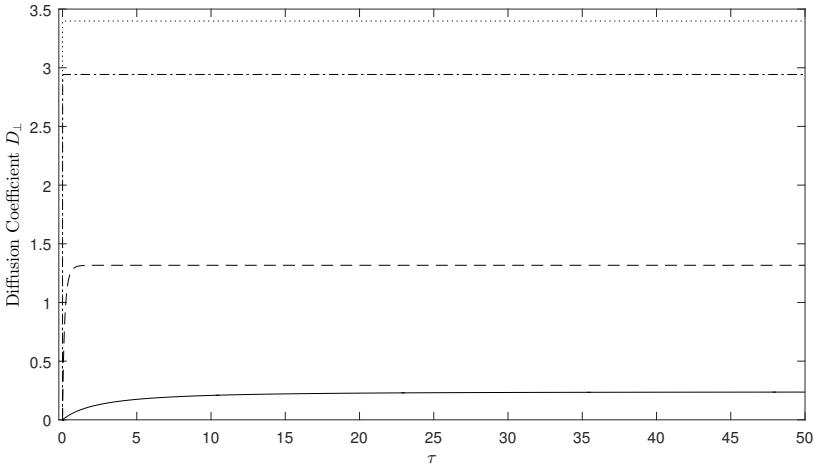

Figure 58: The running diffusion coefficient ratio $D_\perp = (\ell_\parallel^2 \kappa_\perp)/(\ell_\perp^2 \kappa_\parallel)$, plotted vs transformed time $\tau = \kappa_\parallel t/\ell_\parallel^2$, obtained by solving (297), for the 2D turbulence model. Here a Kubo number of $K = 2$ and a energy range spectral index of $q = 3$ has been used. Separate lines are shown for varying values of the parallel mean free path, specifically $\lambda_\parallel/\ell_\parallel = 0.01$ (dotted line), $\lambda_\parallel/\ell_\parallel = 0.1$ (dashed-dotted line), $\lambda_\parallel/\ell_\parallel = 1$ (dashed line), and $\lambda_\parallel/\ell_\parallel = 10$ (solid line).

3.3.4 Two-Component Turbulence

Two-component turbulence is a combination of slab and 2D turbulence. This model has been shown to be a good approximation of the turbulence in the solar wind (see Matthaeus *et al.* (1990) and Bieber *et al.* (1996)). Specifically the magnetic correlation tensor for this model is

$$P_{nm} = g^{slab}(k_\parallel)\frac{\delta(k_\perp)}{k_\perp}\delta_{nm} + g^{2D}(k_\perp)\frac{\delta(k_\parallel)}{k_\perp}\left(\delta_{nm} - \frac{k_n k_m}{k_\perp^2}\right). \tag{298}$$

Using the correlation tensor with equation (264) and then using the same methods as in sections 3.3.1 and 3.3.3 results in

$$\begin{aligned}\frac{d^2}{dt^2}\langle(\Delta x)^2\rangle = {} & \frac{8\pi v^2}{3B_0^2}\int_0^\infty dk_\parallel g^{slab}(k_\parallel)\frac{1}{\omega_{+\xi}-\omega_{-\xi}}(\omega_{+\xi}e^{\omega_{+\xi}t} - \omega_{-\xi}e^{\omega_{-\xi}t}) \\ & + \frac{2\pi v^2}{3B_0^2}\int_0^\infty dk_\perp g^{2D}(k_\perp)e^{-vt/\lambda_\parallel - k_\perp^2\langle(\Delta x)^2\rangle/2}.\end{aligned} \tag{299}$$

Employing the spectra (273) and (290) gives

$$\begin{aligned}\frac{d^2}{dt^2}\langle(\Delta x)^2\rangle = {} & \frac{4v^2\delta B_{slab}^2\ell_\parallel C(s)}{3B_0^2}\int_0^\infty dk_\parallel(1+(k_\parallel\ell_\parallel)^2)^{-s/2}\frac{1}{\omega_{+\xi}-\omega_{-\xi}}(\omega_{+\xi}e^{\omega_{+\xi}t} - \omega_{-\xi}e^{\omega_{-\xi}t}) \\ & + \frac{4v^2 D(s,q)\delta B_{2D}^2\ell_\perp}{3B_0^2}\int_0^\infty dk_\perp\frac{(k_\perp\ell_\perp)^q}{(1+k_\perp^2\ell_\perp^2)^{(s+q)/2}}e^{-vt/\lambda_\parallel - k_\perp^2\langle(\Delta x)^2\rangle/2}.\end{aligned} \tag{300}$$

Then using the transformations (275) - (279), and $y = k_\perp\ell_\perp$ finally results in the numerically solvable ODE

$$\begin{aligned}\frac{d^2}{dt^2}\langle(\Delta x)^2\rangle = {} & \frac{24K^2\ell_\parallel^2}{\lambda_\parallel^2}\left(\frac{C(s)\delta B_{slab}^2}{\delta B^2}\int_0^\infty dz(1+z^2)^{-s/2}\frac{1}{\Omega_+-\Omega_-}(\Omega_+e^{\Omega_+ t} - \Omega_- e^{\Omega_- t})\right. \\ & \left. + \frac{D(s,q)\delta B_{2D}^2}{\delta B^2}\int_0^\infty dy\frac{y^q}{(1+y^2)^{(s+q)/2}}e^{-(3\tau\ell_\parallel^2/\lambda_\parallel^2)-(y^2\sigma/2)}\right).\end{aligned} \tag{301}$$

It should be noted that δB^2 in the above equation is the sum of the squares of the slab and 2D magnetic field components, i.e., $\delta B^2 = \delta B^2_{slab} + \delta B^2_{2D} = 2\delta B^2_x$. Therefore there is a required relation for the slab and 2D magnetic turbulence components, given by

$$\frac{\delta B^2_{slab}}{\delta B^2} + \frac{\delta B^2_{2D}}{\delta B^2} = 1. \tag{302}$$

This equation was solved for the following cases. In figures (59) through (62) two cases are considered for each Kubo number. The first case is $\delta B^2_{slab}/\delta B^2 = 0.2$ and $\delta B^2_{2D}/\delta B^2 = 0.8$, while the second case is $\delta B^2_{slab}/\delta B^2 = \delta B^2_{2D}/\delta B^2 = 0.5$. The two Kubo numbers considered are $K = 0.7$ and $K = 7$, and to keep the number of plots reasonable the only value for the energy range spectral index considered is $q = 3$.

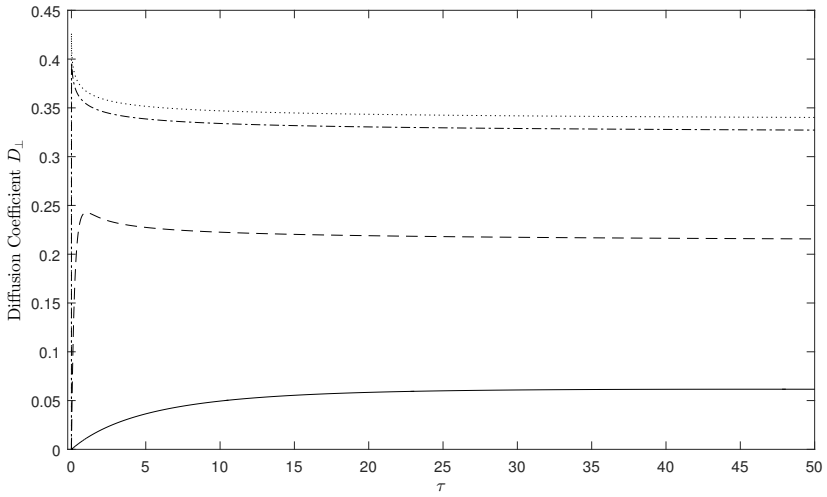

Figure 59: The running diffusion coefficient ratio $D_\perp = (\ell^2_\parallel \kappa_\perp)/(\ell^2_\perp \kappa_\parallel)$, plotted vs transformed time $\tau = \kappa_\parallel t/\ell^2_\parallel$, obtained by solving equation (301), for the 2D turbulence model. Here a Kubo number of $K = 0.7$ and a energy range spectral index of $q = 3$ has been used. The component fractions $\delta B^2_{slab}/\delta B^2 = 0.2$ and $\delta B^2_{2D}/\delta B^2 = 0.8$ are used. Separate lines are shown for varying values of the parallel mean free path, specifically $\lambda_\parallel/\ell_\parallel = 0.01$ (dotted line), $\lambda_\parallel/\ell_\parallel = 0.1$ (dashed-dotted line), $\lambda_\parallel/\ell_\parallel = 1$ (dashed line), and $\lambda_\parallel/\ell_\parallel = 10$ (solid line).

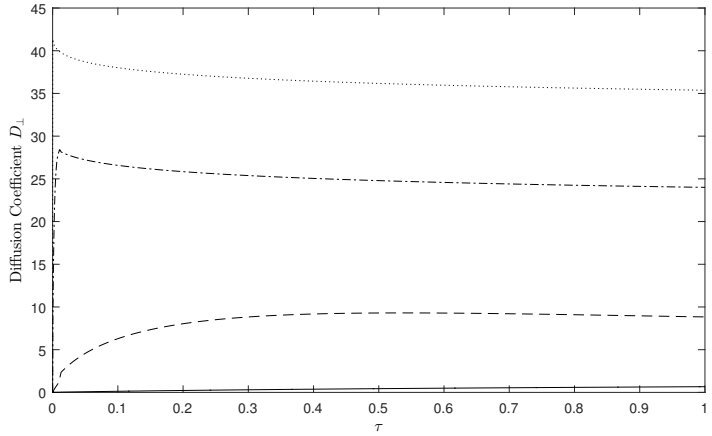

Figure 60: The running diffusion coefficient ratio $D_\perp = (\ell_\parallel^2 \kappa_\perp)/(\ell_\perp^2 \kappa_\parallel)$, plotted vs transformed time $\tau = \kappa_\parallel t/\ell_\parallel^2$, obtained by solving equation (301), for the 2D turbulence model. Here a Kubo number of $K = 7$ and a energy range spectral index of $q = 3$ has been used. The component fractions $\delta B_{slab}^2/\delta B^2 = 0.2$ and $\delta B_{2D}^2/\delta B^2 = 0.8$ are used. Separate lines are shown for varying values of the parallel mean free path, specifically $\lambda_\parallel/\ell_\parallel = 0.01$ (dotted line), $\lambda_\parallel/\ell_\parallel = 0.1$ (dashed-dotted line), $\lambda_\parallel/\ell_\parallel = 1$ (dashed line), and $\lambda_\parallel/\ell_\parallel = 10$ (solid line).

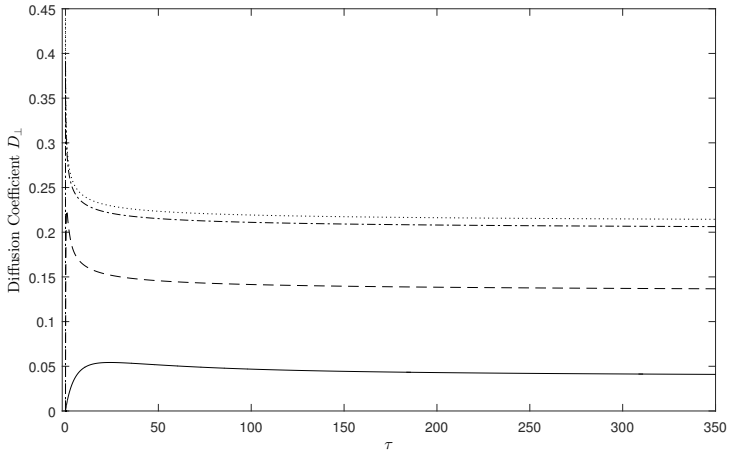

Figure 61: The running diffusion coefficient ratio $D_\perp = (\ell_\parallel^2 \kappa_\perp)/(\ell_\perp^2 \kappa_\parallel)$, plotted vs transformed time $\tau = \kappa_\parallel t/\ell_\parallel^2$, obtained by solving equation (301), for the 2D turbulence model. Here a Kubo number of $K = 0.7$ and a energy range spectral index of $q = 3$ has been used. The component fractions $\delta B_{slab}^2/\delta B^2 = \delta B_{2D}^2/\delta B^2 = 0.5$ are used. Separate lines are shown for varying values of the parallel mean free path, specifically $\lambda_\parallel/\ell_\parallel = 0.01$ (dotted line), $\lambda_\parallel/\ell_\parallel = 0.1$ (dashed-dotted line), $\lambda_\parallel/\ell_\parallel = 1$ (dashed line), and $\lambda_\parallel/\ell_\parallel = 10$ (solid line).

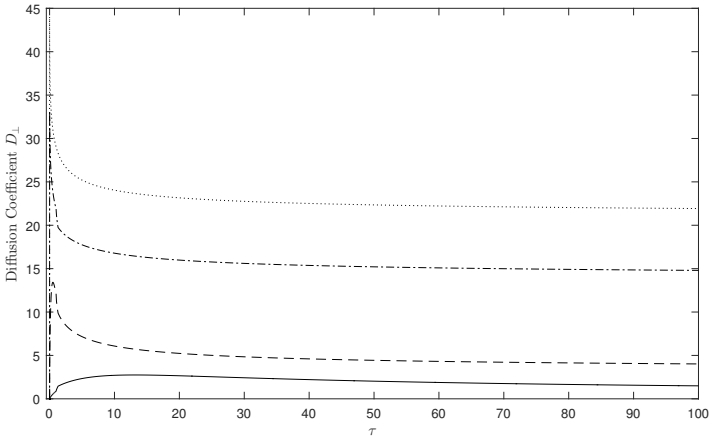

Figure 62: The running diffusion coefficient ratio $D_\perp = (\ell_\parallel^2 \kappa_\perp)/(\ell_\perp^2 \kappa_\parallel)$, plotted vs transformed time $\tau = \kappa_\parallel t/\ell_\parallel^2$, obtained by solving equation (301), for the 2D turbulence model. Here a Kubo number of $K = 7$ and a energy range spectral index of $q = 3$ has been used. The component fractions $\delta B_{slab}^2/\delta B^2 = \delta B_{2D}^2/\delta B^2 = 0.5$ are used. Separate lines are shown for varying values of the parallel mean free path, specifically $\lambda_\parallel/\ell_\parallel = 0.01$ (dotted line), $\lambda_\parallel/\ell_\parallel = 0.1$ (dashed-dotted line), $\lambda_\parallel/\ell_\parallel = 1$ (dashed line), and $\lambda_\parallel/\ell_\parallel = 10$ (solid line).

3.3.5 Numerical Methods

To understand how the results in sections 3.3.1 through 3.3.4 were obtained numerical integration must be understood. The basics of numerical integration were discussed already in section 2.2.4. Matlab's built in ODE45 is a Runge-Kutta (4,5) integrator. This pre-built integrator was used as a basis to find these results. The Runge-Kutta (4,5) method is also known as the Dormand–Prince method (see Shampine & Reichelt (2016)). All explicit Runge-Kutta methods are described by

$$f_{n+1} = f_n + h \sum b_i k_i, \tag{303}$$

where h is the step size and

$$k_i = g(t_n + c_i h, f_n + h(a_{i1}k_1 + a_{i2}k_2 + ... + a_{i,i-1}k_{i-1})). \tag{304}$$

The relation between b_i, $a_{i,j}$, and b_i can be described by what is called a Butcher tableau. A Butcher tableau uniquely defines a set of functions which determine how any particular Runge-Kutta method works. The general form of a Butcher tableau is

$$\begin{array}{c|ccccc} 0 & & & & & \\ c_2 & a_{21} & & & & \\ c_3 & a_{31} & a_{32} & & & \\ \vdots & \vdots & \vdots & \ddots & & \\ c_s & a_{s1} & a_{s2} & ... & a_{s,s-1} & \\ \hline & b_1 & b_2 & ... & b_{s-1} & b_s \end{array}$$

In the case of the Dormand-Prince method (see Dormand & Prince (1980)), the Butcher tableau is

0							
1/5	1/5						
3/10	3/40	9/40					
4/5	44/45	-56/15	32/9				
8/9	19372/6561	−25360/2187	64448/6561	−212/729			
1	9017/3168	−355/33	46732/5247	49/176	−5103/18656		
1	35/384	0	500/1113	125/192	−2187/6784	11/84	
	35/384	0	500/1113	125/192	−2187/6784	11/84	
	5179/57600	0	7571/16695	393/640	−92097/339200	187/2100	1/40

It should be noted that the lowest row in the tableau is only used for error estimation, and is in fact the b coefficients corresponding to the next lowest order approximation. However, the basic ODE45 integrator was used along with some condition checking code to help obtain more accurate solutions. This was required due to the extreme acceleration and jerk of the ODE solution at early times. The error tolerances in the integrator were changed first, to allow for a more accurate solution. The computational time required however for the more stringent error tolerance was on the order of weeks for each solution. So the time steps taken by the integrator had to be manually monitored and changed according to the portion of the solution the integrator was solving for. The solution was broken up into 5 sections, spaced as such

$$\begin{aligned} t_1 &= 0 \to 0.00001, \\ t_2 &= 0.00001 \to 0.0001, \\ t_3 &= 0.0001 \to 0.01, \\ t_4 &= 0.01 \to 1, \\ t_5 &= 1 \to 100, \quad \text{and} \\ t_6 &> 100, \end{aligned} \tag{305}$$

where in each successive time section the error tolerance and the step size variance was allowed to be larger than that of the last section. After finding the solution in one section, the final function value was fed into the integrator as an initial condition for the next section. After finding the solution in all sections, duplicate initial and final solution values were accounted for and then the solutions were stitched together. It can be noted that for some turbulence models the solution reached a level of consistency earlier than others. That is why plots for each turbulence model run to different final time values. So that both early and late times can be seen in each figure.

3.4 Modeling the Perpendicular Exponential

Recall from section 3.2 the UNLT theory equation of motion

$$\langle V_x(t)V_x(0)\rangle = \frac{1}{B_0^2}\int d^3k P_{xx}(\vec{k})\xi(t,0)\langle e^{i\vec{x}_\perp\cdot\vec{k}_\perp}\rangle. \tag{306}$$

In section 3.2 the following assumption was made

$$\langle e^{i\vec{x}_\perp\cdot\vec{k}_\perp}\rangle = e^{-\frac{1}{2}\langle(\Delta x)^2\rangle k_\perp^2}. \tag{307}$$

This is an assumption that the particle distribution will be Gaussian. It is a very common assumption made in this field. However, there are a couple other interesting assumptions that can be made about the particle distribution. Two common ones are the step function distribution and the kappa function distribution. The step function distribution is given by

$$\langle e^{i\vec{x}_\perp\cdot\vec{k}_\perp}\rangle = \Theta\Big(1 - B_{step}\frac{1}{2}\langle(\Delta x)^2\rangle k_\perp^2\Big), \tag{308}$$

where B_{step} is a normalization constant. B_{step} can be determined by employing the normalization condition

$$\int_0^\infty dk_\perp \Theta\left(1 - B_{step}\frac{1}{2}\langle(\Delta x)^2\rangle k_\perp^2\right) = \sqrt{\frac{\pi}{2\langle(\Delta x)^2\rangle}}. \tag{309}$$

Employing this condition leads to

$$B_{step} = 2\sqrt{\frac{2}{\pi}}, \tag{310}$$

therefore the normalized step function can be written as

$$\langle e^{i\vec{x}_\perp \cdot \vec{k}_\perp} \rangle = \Theta\Big(1 - \sqrt{\frac{2}{\pi}}\langle (\Delta x)^2 \rangle k_\perp^2\Big). \tag{311}$$

The kappa distribution is given by

$$\langle e^{i\vec{x}_\perp \cdot \vec{k}_\perp} \rangle = \frac{1}{[1 + B_\kappa \frac{1}{2}\langle (\Delta x)^2 \rangle k_\perp^2]^\kappa}. \tag{312}$$

Where B_κ is a normalization constant. B_κ can be determined by employing the normalization condition

$$\int_0^\infty dk_\perp \frac{1}{[1 + B_\kappa \frac{1}{2}\langle (\Delta x)^2 \rangle k_\perp^2]^\kappa} = \sqrt{\frac{\pi}{2\langle (\Delta x)^2 \rangle}}. \tag{313}$$

Employing this condition leads to

$$B_\kappa = \left(\frac{\Gamma(\kappa - 1/2)}{\Gamma(\kappa)}\right)^2, \tag{314}$$

therefore the normalized kappa function can be written as

$$\langle e^{i\vec{x}_\perp \cdot \vec{k}_\perp} \rangle = \frac{1}{\left[1 + \left(\frac{\Gamma(\kappa - 1/2)}{\Gamma(\kappa)}\right)^2 \frac{1}{2}\langle (\Delta x)^2 \rangle k_\perp^2\right]^\kappa}. \tag{315}$$

In this section these two other particle distributions are explored for noisy slab turbulence, 2D turbulence, and twp component turbulence (also called composite turbulence).

3.4.1 Step Function Particle Distribution

To solve the time dependent UNLT theory equation with a step function particle distribution, three possible magnetic correlation tensors are used. First the noisy slab model is examined. Recall the magnetic correlation function for the noisy slab model (270), and the parallel correlation function (265). Using these the noisy slab step function velocity auto-correlation, can be written as

$$\begin{aligned} \langle V_x(t_1) V_x(0) \rangle = \frac{4\pi v^2 \ell_\perp}{3B_0^2} \int_0^\infty dk_\parallel g^{slab}(k_\parallel) \frac{1}{\omega_+ - \omega_-}[\omega_+ e^{\omega_+ t} - \omega_- e^{\omega_- t}] \\ \times \int_0^{1/\ell_\perp} dk_\perp \Theta\big(1 - B_{step}\frac{1}{2}\langle (\Delta x)^2 \rangle k_\perp^2\big) \end{aligned} \tag{316}$$

To solve the $k_\perp$ integral two cases must be considered. The first case is when $\langle (\Delta x)^2 \rangle / \ell_\perp^2 \leq \pi/2$. In this case

$$\int_0^{1/\ell_\perp} dk_\perp \Theta\big(1 - B_{step}\frac{1}{2}\langle (\Delta x)^2 \rangle k_\perp^2\big) = \int_0^{1/\ell_\perp} dk_\perp = \frac{1}{\ell_\perp}. \tag{317}$$

The second case is when $\langle (\Delta x)^2 \rangle / \ell_\perp^2 \geq \pi/2$. In this case

$$\int_0^{1/\ell_\perp} dk_\perp \Theta\big(1 - B_{step}\frac{1}{2}\langle (\Delta x)^2 \rangle k_\perp^2\big) = \int_0^{\sqrt{\pi/2\langle (\Delta x)^2 \rangle}} dk_\perp = \sqrt{\frac{\pi}{2\langle (\Delta x)^2 \rangle}}. \tag{318}$$

In order to write the ODE the following function must be defined,

$$G\big(\langle (\Delta x)^2 \rangle\big) = \begin{cases} 1 & if \quad \frac{\langle (\Delta x)^2 \rangle}{\ell_\perp^2} \leq \frac{\pi}{2} \\ \sqrt{\frac{\ell_\perp^2 \pi}{2\langle (\Delta x)^2 \rangle}} & if \quad \frac{\langle (\Delta x)^2 \rangle}{\ell_\perp^2} \geq \frac{\pi}{2}. \end{cases} \tag{319}$$

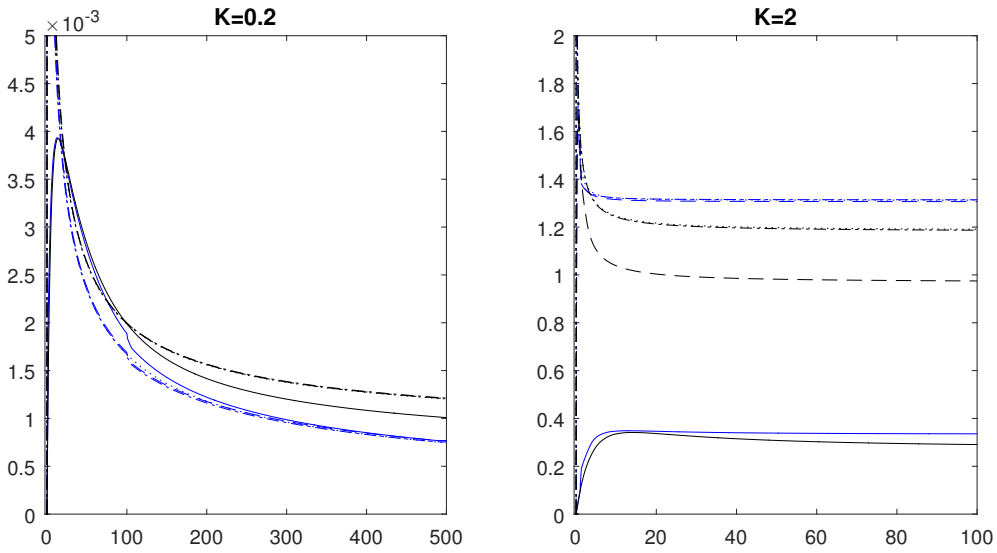

Figure 63: The running diffusion coefficient $D_\perp := (\ell_\parallel^2 d_\perp/\ell_\perp^2\kappa_\parallel)$ plotted versus time $\tau = \kappa_\parallel t/\ell_\parallel^2$ for the step distribution, noisy slab turbulence model (plotted in blue), obtained by solving (320) for $\lambda_\parallel/\ell_\parallel = 0.1$ (dotted line), $\lambda_\parallel/\ell_\parallel = 1$ (dashed-dotted line), $\lambda_\parallel/\ell_\parallel = 10$ (dashed line), and $\lambda_\parallel/\ell_\parallel = 100$ (solid line). The Kubo numbers are as titled. Compared to the running diffusion coefficient versus time for the Gaussian distribution, noisy slab turbulence model as solved in section 3.3.1 (plotted in black).

The TGK formula (250) is then employed, as well as the transformations (275) - (277), and (279). For the spectrum $g^{slab}(k_\parallel)$ equation (273) is used. The numerically solvable ODE can then be written as

$$\frac{d^2}{dt^2}\sigma = 24C(s)K^2G(\sigma)\frac{\ell_\parallel^2}{\lambda_\parallel^2}\int_0^\infty dz(1+z^2)^{-s/2}\frac{1}{\omega_+-\omega_-}[\omega_+e^{\omega_+ t}-\omega_-e^{\omega_- t}]. \tag{320}$$

The solutions to this equation for Kubo numbers of 0.2 and 2 are shown in figure (63) alongside the corresponding solutions to the Gaussian distribution.

Next the 2D magnetic correlation model is examined. Recall the magnetic correlation function for the 2D turbulence model (289), and the parallel correlation function (265). Using these functions evaluated with $k_\parallel = 0$, the 2D turbulence step function velocity auto-correlation function can be written as

$$\langle V_x(t_1)V_x(0)\rangle = \frac{\pi v^2}{3B_0^2}e^{-vt/\lambda_\parallel}\int_0^\infty dk_\perp g^{2D}(k_\perp)\Theta\Big(1-B_{step}\frac{1}{2}\langle(\Delta x)^2\rangle k_\perp^2\Big) \tag{321}$$

Again the TGK formula (250) is employed, as well as the transformations $z = k_\perp\ell_\perp$, (276), (277), and (279). For the spectrum $g^{2D}(k_\parallel)$ equation (290) is used. Finally the numerically solvable ODE can be written as

$$\frac{d^2}{dt^2}\sigma = 24D(s,q)\frac{\ell_\parallel^2}{\lambda_\parallel^2}K^2e^{-3\tau\ell_\parallel^2/\lambda_\parallel^2}\int_0^{\sqrt{\pi/2\sigma}}dz\frac{z^q}{[1+z^2]^{(s+q)/2}}. \tag{322}$$

The solutions to this equation for Kubo numbers of 0.2 and 2 are shown in figure (64) alongside the corresponding solutions for the Gaussian distribution.

Next the composite turbulence magnetic correlation model is examined. Recall that the magnetic correlation function for the composite model is given by equation (298). Using this magnetic correlation function as well as the parallel correlation function (265), the composite turbulence step function velocity auto-correlation can be written as

$$\begin{aligned}\langle V_x(t_1)V_x(0)\rangle = &\frac{\pi v^2}{3B_0^2}\int_0^\infty dk_\perp g^{2D}(k_\perp)e^{-vt/\lambda_\parallel}\Theta\big(1-B_{step}\frac{1}{2}\langle(\Delta x)^2\rangle k_\perp^2\big)\\ &+\frac{4\pi v^2}{3B_0^2}\int_0^\infty dk_\parallel g^{slab}(k_\parallel)\frac{1}{\omega_+-\omega_-}[\omega_+e^{\omega_+ t}-\omega_-e^{\omega_- t}].\end{aligned} \tag{323}$$

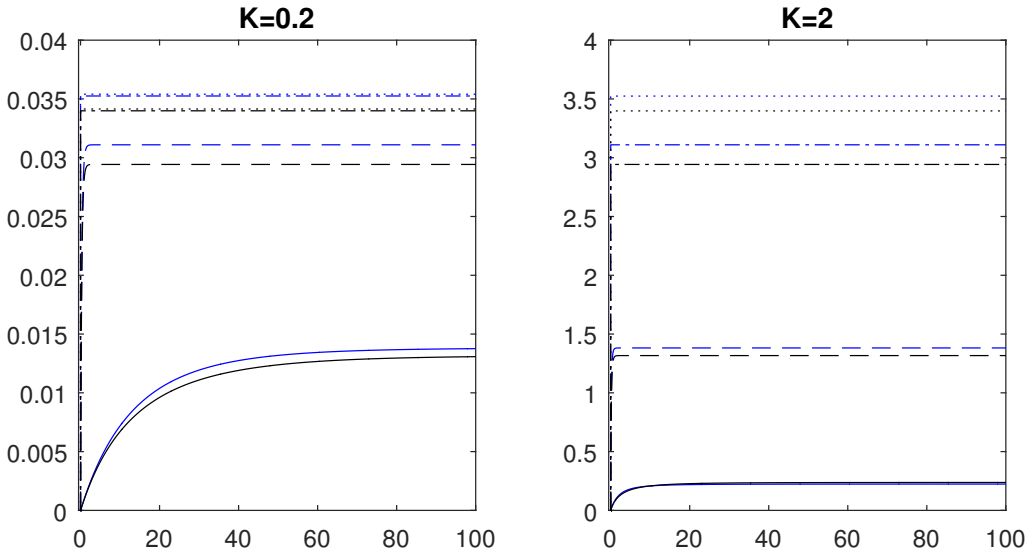

Figure 64: The running diffusion coefficient $D_\perp := (\ell_\parallel^2 d_\perp/\ell_\perp^2\kappa_\parallel)$ plotted versus time $\tau = \kappa_\parallel t/\ell_\parallel^2$ for the step distribution, 2D turbulence model (plotted in blue), obtained by solving (322) for $\lambda_\parallel/\ell_\parallel = 0.1$ (dotted line), $\lambda_\parallel/\ell_\parallel = 1$ (dashed-dotted line), $\lambda_\parallel/\ell_\parallel = 10$ (dashed line), and $\lambda_\parallel/\ell_\parallel = 100$ (solid line). The Kubo numbers are as titled. Compared to the running diffusion coefficient versus time for the Gaussian distribution, 2D turbulence model as solved in section 3.3.3 (plotted in black).

Once again the TGK formula (250) is employed and the transformations (275), $x = \ell_\perp k_\perp$, (276), (277), and (279). For the spectra equations (273) and (290) are employed. Now the numerically solvable ODE is written as

$$\begin{aligned}\frac{d^2}{dt^2}\sigma = {} & 24D(s,q)\frac{\delta B_{2D}^2}{\delta B^2}\frac{\ell_\parallel^2}{\lambda_\parallel^2}K^2 e^{-3\tau\ell_\parallel^2/\lambda_\parallel^2}\int_0^{\sqrt{\pi/2\sigma}} dx \frac{x^q}{[1+x^2]^{(s+q)/2}} \\ & + 24C(s)\frac{\delta B_{slab}^2}{\delta B^2}\frac{\ell_\parallel^2}{\lambda_\parallel^2}K^2\int_0^\infty dz(1+z^2)^{-s/2}\frac{1}{\omega_+-\omega_-}[\omega_+ e^{\omega_+ t} - \omega_- e^{\omega_- t}].\end{aligned} \tag{324}$$

The solutions to this equation for Kubo numbers 0.2 and 2 are shown in figure (65) alongside the corresponding solutions for the Gaussian distribution.

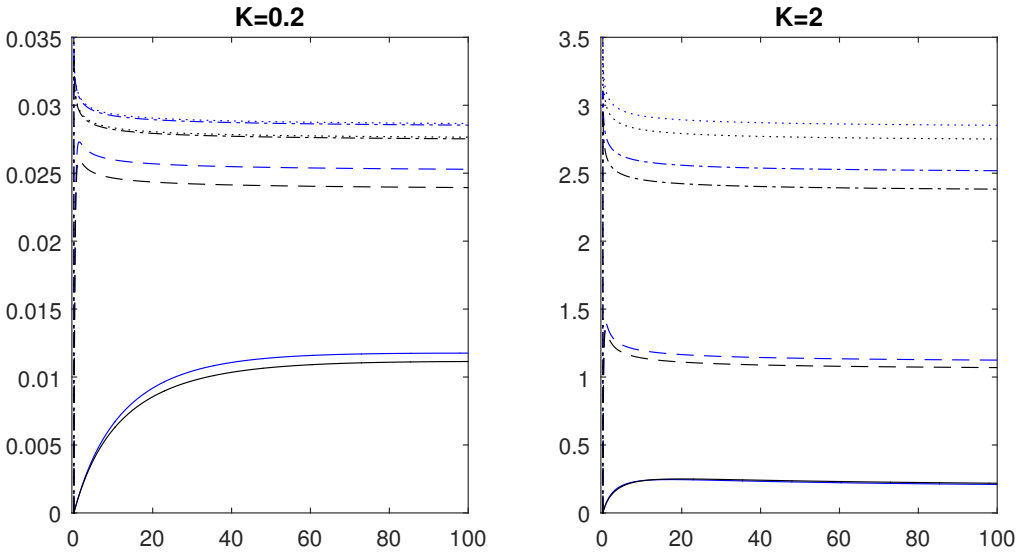

Figure 65: The running diffusion coefficient $D_\perp := (\ell_\parallel^2 d_\perp/\ell_\perp^2\kappa_\parallel)$ plotted versus time $\tau = \kappa_\parallel t/\ell_\parallel^2$ for the step distribution, composite turbulence model (plotted in blue), obtained by solving (324) for $\lambda_\parallel/\ell_\parallel = 0.1$ (dotted line), $\lambda_\parallel/\ell_\parallel = 1$ (dashed-dotted line), $\lambda_\parallel/\ell_\parallel = 10$ (dashed line), and $\lambda_\parallel/\ell_\parallel = 100$ (solid line). The 2D turbulence component $\delta B_{2D}^2/\delta B^2 = 0.2$, and the slab turbulence component $\delta B_{2D}^2/\delta B^2 = 0.8$. The Kubo numbers are as titled. Compared to the running diffusion coefficient versus time for the Gaussian distribution, composite turbulence model as solved in section 3.3.4 (plotted in black).

3.4.2 Kappa Function Particle Distribution

First the kappa function particle distribution is examined using the noisy slab turbulence model. Recall the magnetic correlation function for the noisy slab model (270), and the parallel correlation function (265), the noisy slab kappa function velocity auto-correlation, can be written as

$$\begin{aligned}\langle V_x(t_1)V_x(0)\rangle = \frac{4\pi v^2\ell_\perp}{3B_0^2}\int_0^\infty dk_\parallel g^{slab}(k_\parallel)\frac{1}{\omega_+-\omega_-}[\omega_+e^{\omega_+t}-\omega_-e^{\omega_-t}]\\ \times\int_0^{1/\ell_\perp} dk_\perp \frac{1}{[1+B_\kappa\frac{1}{2}\langle(\Delta x)^2\rangle k_\perp^2]^\kappa}\end{aligned} \tag{325}$$

The integral in $k_\perp$ can be written as a Gaussian hypergeometric function

$$\int_0^{1/\ell_\perp} dk_\perp \frac{1}{[1+B_\kappa\frac{1}{2}\langle(\Delta x)^2\rangle k_\perp^2]^\kappa} = \frac{1}{\ell_\perp}{}_2F_1\left(\frac{1}{2},\kappa;\frac{3}{2},-B_\kappa\frac{\langle(\Delta x)^2\rangle}{2\ell_\perp}\right). \tag{326}$$

The TGK formula (250) is employed, as well as the transformations (275) - (277), and (279). For the spectrum $g^{slab}(k_\parallel)$ again equation (273) is used. Now the numerically solvable ODE is given by

$$\begin{aligned}\frac{d^2}{dt^2}\sigma = 24\sqrt{\pi}C(s)K^2\frac{\ell_\parallel^2}{\lambda_\parallel^2}{}_2F_1\left(\frac{1}{2},\kappa;\frac{3}{2},-B_\kappa\frac{\langle(\Delta x)^2\rangle}{2\ell_\perp}\right)\\ \times\int_0^\infty dz(1+z^2)^{-s/2}\frac{1}{\omega_+-\omega_-}[\omega_+e^{\omega_+t}-\omega_-e^{\omega_-t}].\end{aligned} \tag{327}$$

The solutions to this equation for $\kappa = 2, 10$ and Kubo numbers of 0.2 and 2 are shown in figure (66) alongside the corresponding solutions for the Gaussian distribution.

Next the kappa function particle distribution is examined using the 2D magnetic turbulence model. Recall the magnetic correlation function for the 2D turbulence model (289), and the parallel correlation function (265) evaluated with $k_\parallel = 0$, the 2D turbulence kappa function velocity auto-correlation

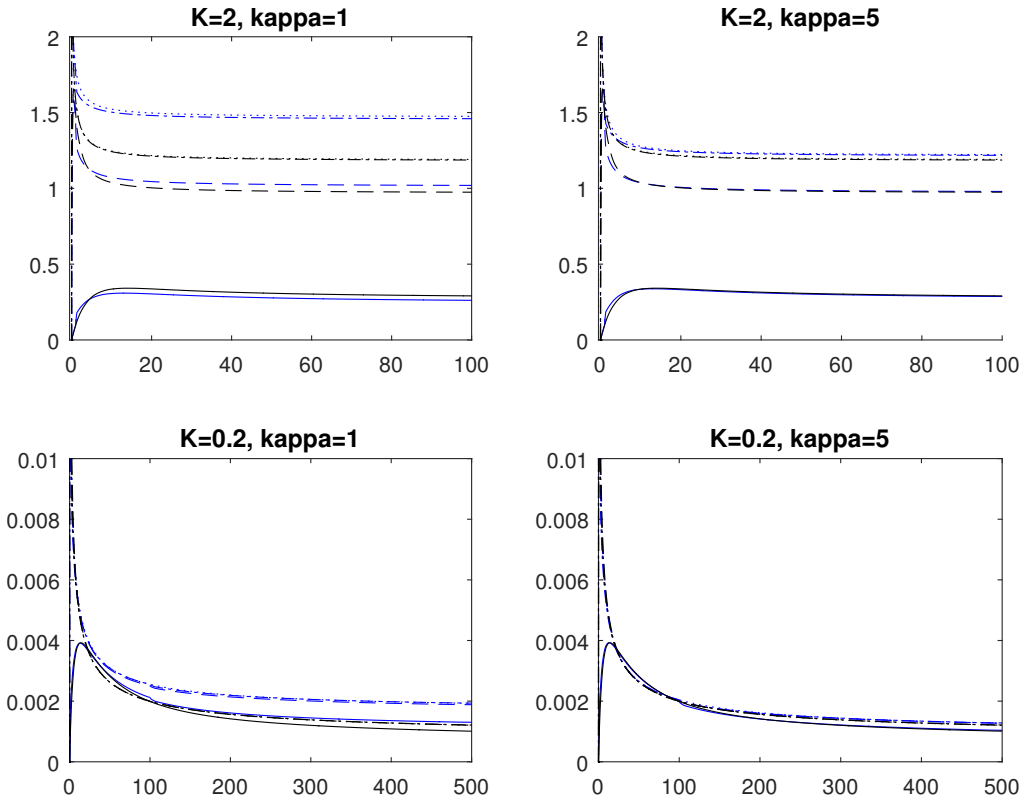

Figure 66: The running diffusion coefficient $D_\perp := (\ell_\parallel^2 d_\perp / \ell_\perp^2 \kappa_\parallel)$ plotted versus time $\tau = \kappa_\parallel t / \ell_\parallel^2$ for the kappa distribution, noisy slab turbulence model (plotted in blue), obtained by solving (327) for $\lambda_\parallel / \ell_\parallel = 0.1$ (dotted line), $\lambda_\parallel / \ell_\parallel = 1$ (dashed-dotted line), $\lambda_\parallel / \ell_\parallel = 10$ (dashed line), and $\lambda_\parallel / \ell_\parallel = 100$ (solid line). The Kubo numbers and values of κ are as titled. Compared to the running diffusion coefficient versus time for the Gaussian distribution, noisy slab turbulence model as solved in section 3.3.1.

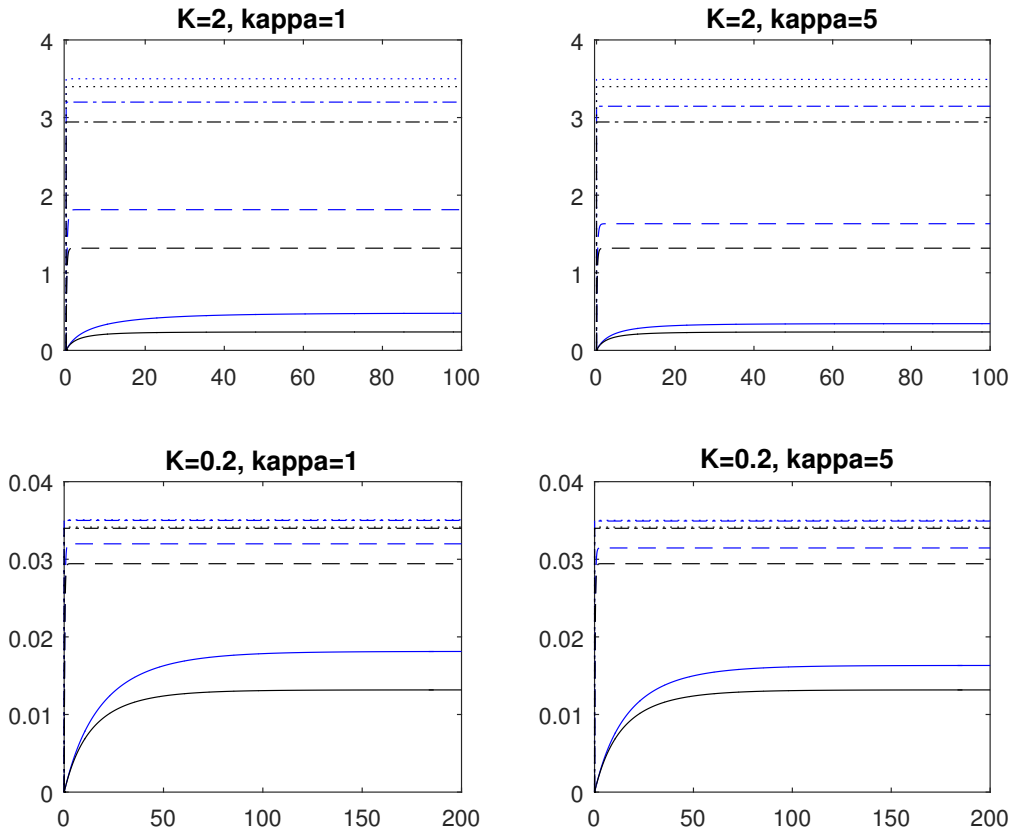

Figure 67: The running diffusion coefficient $D_\perp := (\ell_\parallel^2 d_\perp/\ell_\perp^2\kappa_\parallel)$ plotted versus time $\tau = \kappa_\parallel t/\ell_\parallel^2$ for the kappa distribution, 2D turbulence model (plotted in blue), obtained by solving (329) for $\lambda_\parallel/\ell_\parallel = 0.1$ (dotted line), $\lambda_\parallel/\ell_\parallel = 1$ (dashed-dotted line), $\lambda_\parallel/\ell_\parallel = 10$ (dashed line), and $\lambda_\parallel/\ell_\parallel = 100$ (solid line). The Kubo numbers and values of κ are as titled. Compared to the running diffusion coefficient versus time for the Gaussian distribution, 2D turbulence model as solved in section 3.3.3 (plotted in black).

function, can be written as

$$\langle V_x(t)V_x(0)\rangle = \frac{\pi v^2}{3B_0^2}\int_0^\infty dk_\perp g^{2D}(k_\perp)e^{-vt/\lambda_\parallel}\frac{1}{[1+B_\kappa\frac{1}{2}\langle(\Delta x)^2\rangle k_\perp^2]^\kappa}. \tag{328}$$

Again the TGK formula (250) is employed. Also employed are the transformations $x = \ell_\perp k_\perp$, (276), (277), and (279). For the spectrum $g^{2D}(k_\perp)$ equation (290) is used. Now the numerically solvable PDE can be written as

$$\frac{d^2}{dt^2}\sigma = 24D(s,q)\frac{\ell_\parallel^2}{\lambda_\parallel^2}K^2 e^{-3\tau\ell_\parallel^2/\lambda_\parallel^2}\int_0^\infty dx\frac{x^q}{[1+x^2]^{(s+q)/2}}\frac{1}{[1+B_\kappa\sigma x^2/2]^\kappa}. \tag{329}$$

The solutions to this equation for $\kappa = 2, 10$ and Kubo numbers of 0.2 and 2 are shown in figure (67) alongside the corresponding solutions for the Gaussian distribution.

Lastly the kappa function particle distribution is examined using the composite turbulence model. Recall the magnetic correlation function for the composite turbulence model is given by equation (298). Using this model along with the parallel correlation function (265), the composite turbulence kappa

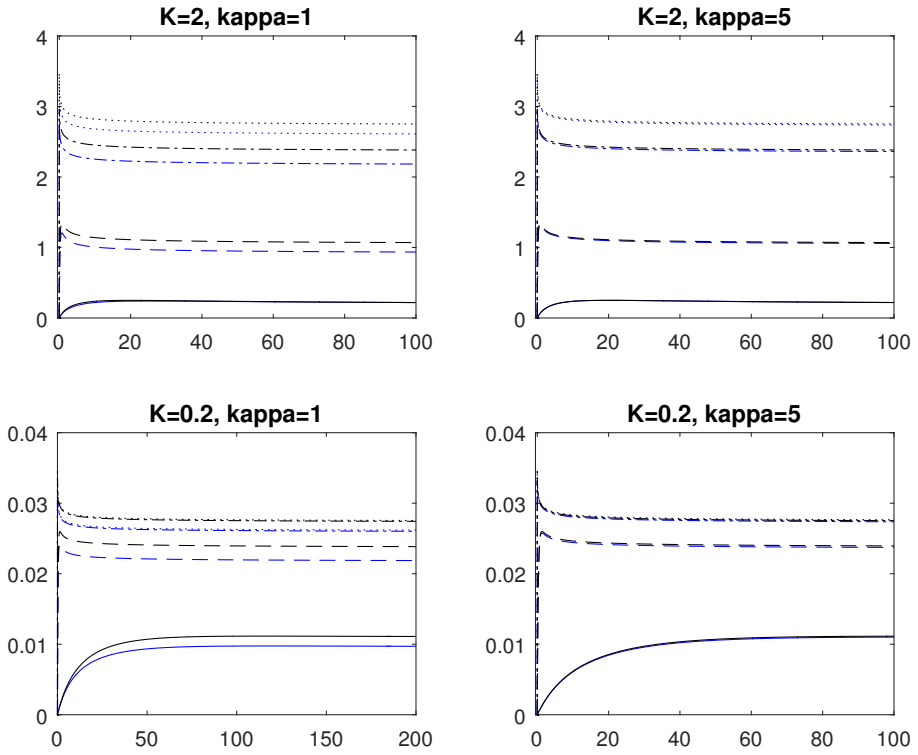

Figure 68: The running diffusion coefficient $D_\perp := (\ell_\parallel^2 d_\perp/\ell_\perp^2\kappa_\parallel)$ plotted versus time $\tau = \kappa_\parallel t/\ell_\parallel^2$ for the kappa distribution, composite turbulence model (plotted in blue), obtained by solving (331) for $\lambda_\parallel/\ell_\parallel = 0.1$ (dotted line), $\lambda_\parallel/\ell_\parallel = 1$ (dashed-dotted line), $\lambda_\parallel/\ell_\parallel = 10$ (dashed line), and $\lambda_\parallel/\ell_\parallel = 100$ (solid line). The 2D turbulence component $\delta B_{2D}^2/\delta B^2 = 0.2$, and the slab turbulence component $\delta B_{2D}^2/\delta B^2 = 0.8$. The Kubo numbers and values of κ are as titled. Compared to the running diffusion coefficient versus time for the Gaussian distribution, composite turbulence model as solved in section 3.3.4 (plotted in black).

function velocity auto-correlation, can be written as

$$\begin{aligned}\langle V_x(t_1)V_x(0)\rangle = &\frac{\pi v^2}{3B_0^2}\int_0^\infty dk_\perp g^{2D}(k_\perp)e^{-vt/\lambda_\parallel}\frac{1}{[1+B_\kappa\frac{1}{2}\langle(\Delta x)^2\rangle k_\perp^2]^\kappa}\\ &+\frac{4\pi v^2}{3B_0^2}\int_0^\infty dk_\parallel g^{slab}(k_\parallel)\frac{1}{\omega_+-\omega_-}[\omega_+e^{\omega_+t}-\omega_-e^{\omega_-t}].\end{aligned} \tag{330}$$

Again the TGK formula (250) is used and the transformations (275) - (277), (279), and $x = \ell_\perp k_\perp$. For the spectra equations (273) and (290) are used. Which results in the numerically solvable ODE,

$$\begin{aligned}\frac{d^2}{dt^2}\sigma = &24D(s,q)\frac{\delta B_{2D}^2}{\delta B^2}\frac{\ell_\parallel^2}{\lambda_\parallel^2}K^2e^{-3\tau\ell_\parallel^2/\lambda_\parallel^2}\int_0^\infty dx\frac{x^q}{[1+x^2]^{(s+q)/2}}\frac{1}{[1+B_\kappa\sigma x^2/2]^\kappa}\\ &+24C(s)\frac{\delta B_{slab}^2}{\delta B^2}\frac{\ell_\parallel^2}{\lambda_\parallel^2}K^2\int_0^\infty dz(1+z^2)^{-s/2}\frac{1}{\omega_+-\omega_-}[\omega_+e^{\omega_+t}-\omega_-e^{\omega_-t}].\end{aligned} \tag{331}$$

The solutions to this equation for $\kappa = 2, 10$ and Kubo numbers of 0.2 and 2 are shown in figure (68) alongside the corresponding solutions for the Gaussian distribution.

4 Discussion of Results

In this thesis a wide variety of results were obtained. In this section significant figures are discussed, and a summary of derived equations is provided.

4.1 Fokker-Planck Scattering Coefficient Models

The isotropic model (equation (52)) for the Fokker-Planck scattering coefficient has been proven to have some validity, and it is commonly used. For that reason it is the benchmark used here to compare the other models against. In numerical solutions it is shown that the fully z-dependent solution follows the following process (see figures (6) through (10)). Initially the Gaussian function expands along the μ-axis. This happens quickly and the solution leaves its anisotropic state. Once isotropization has happened, the solution is of course independent of μ. Next the only major change in the function is that it slowly propagates along the z-axis. Figures (13) - (16) show the solution for the constant $D_{\mu\mu}$. The biggest difference in this model is that during the isotropization process the solution does not maintain its Gaussian distribution in μ. The Gaussian distribution is a significant property of the isotropic model solution so this may be worth further study. Figures (17) - (20) show the linear model solution. They show that while this solution maintains its Gaussian nature, it takes significantly longer than both the isotropic model and the constant model for this solution to reach pitch angle isotropization. Figures (21) - (24) show the quasi-linear model solution. It is clear immediately that this solution is significantly different than the other models. Namely, the particles do not propagate through the $\mu = 0$ boundary. For this reason the late time limit of the solution depends heavily on whether $\mu_0 < 0$ or $\mu_0 > 0$. This means that the solution never truly loses its dependence on μ_0, which is contrary to the expected behaviour of cosmic rays. Therefore the quasi-linear model is most likely a very poor model, and should not be used in the future. Figures (29) - (32) are the μ only dependent solutions. They show that the linear $D_{\mu\mu}$ model solution expands the quickest along the μ axis. It also especially quickly has a significant number of particles travelling parallel with respect to the magnetic field, $\mu = 1$. These figures also show that all but the quasi-linear model eventually becomes independent of μ, and because they become constant at $F = 1$, it verifies that the solutions are normalized. Figure (33) is the velocity correlation function for all solutions as a function of time. It shows that the isotropic, constant, and linear models all converge to the same value for their VCF as $t \to \infty$. From the quickest to the slowest, they approach this point in the following order; constant model, isotropic model, linear model. Figure (34) shows the running diffusion coefficient for each model. It shows that the isotropic, constant, and linear models all become either diffusive or slightly sub-diffusive, while the quasi-linear model becomes either super-diffusive or ballistic in its propagation (recall equation (10)). In figure (35) as well as in many of the other figures discussed so far, it can be observed that the constant model solution is slightly more similar to the isotropic model solution than the linear one is. This is great to see, because the constant model is much easier to work with in analytic work than any of the others.

4.2 Approximate Solutions to the Fokker-Planck Equation

Concerning the work done in section 2.6, all of the plots show that the first-order solution is a poor approximation, but both the second and third-order solutions appear to be good approximations. Specifically the second-order solution appears in coincidence with the third-order solution at all but the earliest times. This is a useful result, because while the third-order solution is too complicated to be used in analytic work, the second-order solution is not. The second-order solution merits further study, and will likely be used in future analytic work in this field. Below a table summarizing the properties of the solution for all orders is composed.

In figures (42) through (44) some of the above expectation values have been plotted. It is clear from these figures that the second and third-order solutions are both in coincidence with each other as well as with the numerical solution. A slight exception occurs to this at early times for the value of $\langle z^2 \rangle$; this is due to the finite width of the numerical initial conditions and is an expected discrepancy from analytic results. Figures (45) - (47) show that while the properties of the second and third-order solutions are nearly identical at early times their μ-dependence is not exactly the same. However figures (48) through (50) show that the z-dependencies of the second and third-order solutions are in coincidence with each other as well as with the numerical results.

	1st Order	2nd Order	3rd Order
$\langle \mu \rangle$	0	$\mu_0 e^{-2Dt}$	$\mu_0 e^{-2Dt}$
$\langle \mu^2 \rangle$	$\frac{1}{3}$	$\frac{1}{3}$	$\frac{1-e^{-6Dt}}{3}$
$\langle e^{-ikz} \rangle$	1	$\frac{\omega_+ e^{\omega_+ t} - \omega_- e^{\omega_- t}}{\omega_+ - \omega_-}$	$\frac{\omega_2\omega_3 e^{\omega_1 t}}{(\omega_1-\omega_2)(\omega_1-\omega_3)} + \frac{\omega_1\omega_3 e^{\omega_2 t}}{(\omega_2-\omega_3)(\omega_2-\omega_1)} + \frac{\omega_1\omega_2 e^{\omega_3 t}}{(\omega_1-\omega_3)(\omega_2-\omega_3)}$
$\langle z \rangle$	0	$\frac{\mu_0 v}{2D}(1 - e^{-2Dt})$	NA
$\langle z^2 \rangle$	0	$\frac{v^2}{3D}\left(\frac{e^{-2Dt}}{2D} + t - \frac{1}{2D}\right)$	NA
$\langle \mu\mu_0 e^{-ikz} \rangle$	0	$\frac{\omega_+ e^{\omega_+ t} - \omega_- e^{\omega_- t}}{3(\omega_+ - \omega_-)}$	$\frac{\omega_1 e^{\omega_1 t}(2D+\omega_2+\omega_3+ivk)}{3(\omega_1-\omega_2)(\omega_1-\omega_3)} + \frac{\omega_2 e^{\omega_2 t}(2D+\omega_1+\omega_3+ivk)}{3(\omega_2-\omega_3)(\omega_2-\omega_1)} + \frac{\omega_3 e^{\omega_3 t}(2D+\omega_1+\omega_2+ivk)}{3(\omega_1-\omega_3)(\omega_2-\omega_3)}$
$\langle \mu\mu_0 e^{-i\vec{k}\cdot\vec{x}} \rangle_\alpha$	0	$\frac{e^{-\alpha}(-\alpha^2-2\alpha+2e^\alpha-2)}{\alpha^3(\omega_+-\omega_-)}(\omega_+ e^{\omega_+ t} - \omega_- e^{\omega_- t})$	NA
$\langle \mu\mu_0 e^{-i\vec{k}\cdot\vec{x}} \rangle_\beta$	0	$\frac{\pi}{2}\left(\frac{Erf(\sqrt{\beta})}{2\sqrt{\pi}\beta^{3/2}} - \frac{e^{-\beta}}{\pi\beta}\right)(\omega_+ e^{\omega_+ t} - \omega_- e^{\omega_- t})$	NA

4.3 Turbulence Models for Time Dependent UNLT Theory

This work is among the first examinations of the results from time dependent UNLT theory. Two of the key components of the theory are examined in detail. The magnetic correlation tensor, and the particle distribution. It is found that in general all models have the following behavior. At very early times perpendicular particle transport is ballistic, while at late times transport becomes either diffusive or possibly slightly sub-diffusive. There are different behaviors for the middle times though. In all cases increasing the Kubo number makes the diffusion coefficient larger, and larger values of $\lambda_\parallel/\ell_\parallel$ result in small values for the diffusion coefficient. Figures (51) and (52) show that for the noisy slab turbulence model the ballistic transport regime is always followed by an extreme sub-diffusive regime before leveling off to near diffusion. The sub-diffusive regime is more pronounced for smaller values of $\lambda_\parallel/\ell_\parallel$. The Kubo numbers for this model change the scale of the results but not the general behaviour of the curves. Figure (51) shows the only found case where for a small time one model witch has a larger value of $\lambda_\parallel/\ell_\parallel$ has a larger diffusion coefficient than a model witch has a smaller value of $\lambda_\parallel/\ell_\parallel$. Figures (53) and (54) show that for small Kubo numbers and small values of $\lambda_\parallel/\ell_\parallel$ the Gaussian turbulence model behaves similarly to the noisy slab model. With an extremely sub-diffusive regime proceeding ballistic transport. For small values of $\lambda_\parallel/\ell_\parallel$ and large Kubo numbers this extreme sub-diffusive regime still exits but is very short lived. For all cases of large $\lambda_\parallel/\ell_\parallel$ values, the sub-diffusive regime is nearly diffusive,

and in fact for large Kubo numbers as well there is no sub-diffusive regime at all, particle transport moves smoothly from ballistic to diffusive transport. Figures (55) - (58) show the 2D turbulence model results. It is found that for different values of the energy range spectral index q, the results do not change significantly. In general larger values of q result in only slightly smaller diffusion coefficients. For this model there is no sub-diffusive regime at all. All transport moves directly from being ballistic to being diffusive. For small values of $\lambda_{\parallel}/\ell_{\parallel}$ this occurs very rapidly, while for larger values of $\lambda_{\parallel}/\ell_{\parallel}$ the change from ballistic to diffusive transport is slower. Two-component turbulence is the most complicated model and has the most complicated results. Figures (59) - (62) show that for this model sometimes there is a sub-diffusive regime and sometimes there is not. The following results in more extreme sub-diffusion at middle times; smaller values of $\lambda_{\parallel}/\ell_{\parallel}$, smaller Kubo numbers, and larger contributions from slab turbulence rather than 2D turbulence. All these results show that perpendicular turbulence, high Kubo numbers, and large values of $\lambda_{\parallel}/\ell_{\parallel}$ all suppress the sub-diffusive regime that can often appear before late time diffusion.

4.4 Particle Distribution Models for Time Dependent UNLT Theory

Figures (63) - (65) show the time dependent UNLT theory results for a step function particle distribution. These figures show that the step function distribution compared to the Gaussian distribution changes the diffusion coefficient slightly but does not change the general behaviour of the curves. The difference between the results from the two models is most significant in the slab model where there is no perpendicular turbulence, is least significant in the 2D model results where all the turbulence is perpendicular to the mean field. Figures (66) - (68) show the results using the kappa function particle distribution. In all cases the results are nearly identical as the results using a Gaussian distribution. Therefore the question of whether the particle distribution should be a Gaussian or the kappa function is not a particularly interesting one. In general the results between particle distribution models deviate from each other more for small values of $\lambda_{\parallel}/\ell_{\parallel}$, and are usually in coincidence with each other at large values of $\lambda_{\parallel}/\ell_{\parallel}$. Overall the particle distribution model does not affect the resultant curves very significantly. Therefore further analytic study can be done using simple particle distribution models as fair approximations to more complex systems.

5 Conclusion

In this thesis the Fokker-Planck equation was thoroughly examined. Specifically numerical solutions to it were found for four different models of the Fokker-Planck scattering coefficient. These models were compared to each other and then integrated over z space to compare them with analytic solutions to $F(\mu, t)$ found by A. Shalchi. It was found that the simple $D_{\mu\mu} = constant$ model was similar enough to the isotropic model to merit further analytic investigation. Analytic approximations using Legendre polynomials were found to the fully z-dependent Fokker-Planck equation using an isotropic scattering coefficient model. These solutions were compared to each other as well as to the numerical solution. As well, eight different properties of these approximate solutions were found. It was determined that the second-order solution was a good approximation and was analytically simple enough to use in further work. Aside from the Fokker-Planck equation, the newly developed time dependent UNLT theory for perpendicular transport was examined. Specifically different models for both the magnetic correlation tensor, as well as the particle distribution assumption were tested. The resulting ODE for each model was solved numerically and the resulting functions were compared to each other, as well as (in some cases) to time independent UNLT theory. It was found that time dependent UNLT theory produces significantly better results than the time independent theory. It was also determined that changing the particle distribution function does not make a significant different in the resulting solution. This means that even the simple step function model can be used with validity in further analytic work.

References

Abramowitz, Milton, & Stegun, IA. 1964. Handbook of Mathematical Functions: With Formulas, Graphs, and Mathematical Tables Applied mathematics series. *National Bureau of Standards, Washington, DC*.

Babcock, Horace W. 1948. Magnetic variable stars as sources of cosmic rays. *Physical Review*, **74**(4), 489.

Bieber, John W, Matthaeus, William H, Smith, Charles W, Wanner, Wolfgang, Kallenrode, May-Britt, & Wibberenz, Gerd. 1994. Proton and electron mean free paths: The Palmer consensus revisited. *The Astrophysical Journal*, **420**, 294–306.

Bieber, John W, Wanner, Wolfgang, & Matthaeus, William H. 1996. Dominant two-dimensional solar wind turbulence with implications for cosmic ray transport. *Journal of Geophysical Research: Space Physics*, **101**(A2), 2511–2522.

Blasi, Pasquale. 2013. The origin of galactic cosmic rays. *The Astronomy and Astrophysics Review*, **21**(1), 70.

Burden, Richard L., & Faires, J. Douglas. 1993. *Numerical analysis*. PWS-Kent Pub. Co.

Carlson, Per, & De Angelis, Alessandro. 2011. Nationalism and internationalism in science: the case of the discovery of cosmic rays. *The European Physical Journal H*, **35**(4), 309.

Christian, Dr Eric R. 2011. *Anomalous Cosmic Rays*.

Corrsin, S. 1959. Progress report on some turbulent diffusion research. *Pages 161–164 of: Advances in Geophysics*, vol. 6. Elsevier.

Dormand, John R, & Prince, Peter J. 1980. A family of embedded Runge-Kutta formulae. *Journal of computational and applied mathematics*, **6**(1), 19–26.

Green, Melville S. 1951. Brownian motion in a gas of noninteracting molecules. *The Journal of Chemical Physics*, **19**(8), 1036–1046.

Heisenberg, W. 1946. *Cosmic Radiation*. 1 edn. New York: Dover Publications.

Hess, Victor F. 1912. Über Beobachtungen der durchdringenden Strahlung beisieben Freiballonfahrten. *Phys. Z.*, **13**, 1084–1091.

Hooper, J E, & Scharff, M. 1958. *The Cosmic Radiation*. 1 edn. London: Methuen and Co LTD.

Hörandel, Jörg R. 2013. Early cosmic-ray work published in German. *Pages 52–60 of: AIP Conference Proceedings*, vol. 1516. AIP.

Jacobsen, Martin. 1996. Laplace and the origin of the Ornstein-Uhlenbeck process. *Bernoulli*, **2**(3), 271–286.

Jokipii, J.R. 1966. Cosmic-ray propagation. I. Charged particles in a random magnetic field. *The Astrophysical Journal*, **146**, 480.

Kolmogorov, AN. 1941. Dissipation of energy in the locally isotropic turbulence. *Proceedings: Mathematical and Physical Sciences*, **434**(1890), 15–17.

Kubo, R. 1957. Stochastic theory of magnetic resonance. *Il Nuovo Cimento*, **6**(S3), 1063–1080.

Lasuik, J., & Shalchi, A. 2017. Solutions of the Cosmic Ray Velocity Diffusion Equation. *The Journal of Mathematical Physics*.

Lasuik, J, & Shalchi, A. 2019. Subspace Approximations to the Cosmic Ray Fokker-Planck Equation. *Monthly Notices of the Royal Astronomical Society, in Press*.

Lasuik, J., Fiege, J.D., & Shalchi, A. 2016. Numerical analysis of the Fokker-Planck equation with adiabatic focusing: Realistic pitch-angle scattering. *Advances in Space Research*.

Malkov, MA. 2017. Exact solution of the Fokker-Planck equation for isotropic scattering. *Physical Review D*, **95**(2), 023007.

Matthaeus, WH, Qin, G, Bieber, JW, & Zank, GP. 2003. Nonlinear collisionless perpendicular diffusion of charged particles. *The Astrophysical Journal Letters*, **590**(1), L53.

Matthaeus, William H, Goldstein, Melvyn L, & Roberts, D Aaron. 1990. Evidence for the presence of quasi-two-dimensional nearly incompressible fluctuations in the solar wind. *Journal of Geophysical Research: Space Physics*, **95**(A12), 20673–20683.

Mishev, Alexander. 2006. Possible correlation between cosmic ray variation and atmosphere parameters (present status and future activities at BEO Moussala and Alomar observatory). *arXiv preprint physics/0602120*.

Neuer, Marcus, & Spatschek, Karl H. 2006. Diffusion of test particles in stochastic magnetic fields for small Kubo numbers. *Physical Review E*, **73**(2), 026404.

NobelMedia. 2018. *The Nobel Prize in Physics 1936*.

Pacini, D. 1912. La radiazione penetrante alla superficie ed in seno alle acque. *Il Nuovo Cimento*, **3**(Dec.), 93–100.

Planck, Max. 1917. *Über einen Satz der statistischen Dynamik und seine Erweiterung in der Quantentheorie*. Reimer.

Press, William H, Flannery, Brian P, Teukolsky, Saul A, Vetterling, William T, *et al.* . 1989. *Numerical recipes*. Cambridge university press Cambridge.

Revuz, Daniel, & Yor, Marc. 2013. *Continuous martingales and Brownian motion*. Vol. 293. Springer Science & Business Media.

Shalchi, A. 2005. Second-order quasilinear theory of cosmic ray transport. *Physics of Plasmas*, **12**(5), 052905.

Shalchi, A. 2010. A unified particle diffusion theory for cross-field scattering: subdiffusion, recovery of diffusion, and diffusion in three-dimensional turbulence. *The Astrophysical Journal Letters*, **720**(2), L127.

Shalchi, A, & Weinhorst, B. 2009. Random walk of magnetic field lines: Subdiffusive, diffusive, and superdiffusive regimes. *Advances in Space Research*, **43**(9), 1429–1435.

Shalchi, A, Škoda, T, Tautz, RC, & Schlickeiser, R. 2009. Analytical description of nonlinear cosmic ray scattering: isotropic and quasilinear regimes of pitch-angle diffusion. *Astronomy & Astrophysics*, **507**(2), 589–597.

Shalchi, A, Tautz, RC, & Rempel, TJ. 2011. Test-particle transport: higher-order correlations and time-dependent diffusion. *Plasma Physics and Controlled Fusion*, **53**(10), 105016.

Shalchi, Andreas. 2009. *Nonlinear cosmic ray diffusion theories*. Vol. 362. Springer.

Shalchi, Andreas. 2015. Perpendicular diffusion of energetic particles in collisionless plasmas. *Physics of Plasmas*, **22**(1), 010704.

Shalchi, Andreas. 2017. Time-dependent perpendicular transport of energetic particles in magnetic turbulence with transverse complexity. *Physics of Plasmas*, **24**(5), 050702.

Shampine, L. F., & Reichelt, M. W. 2016. *odefun, https://www.mathworks.com/help/matlab/ref/ode45.html*.

Stassinopoulos, EG, & Raymond, James P. 1988. The space radiation environment for electronics. *Proceedings of the IEEE*, **76**(11), 1423–1442.

Taylor, Geoffrey I. 1922. Diffusion by continuous movements. *Proceedings of the london mathematical society*, **2**(1), 196–212.

Thomson, Brian S. 1994. *Symmetric properties of real functions*. Dekker.

Townsend, Lawrence W. 2005. Implications of the space radiation environment for human exploration in deep space. *Radiation protection dosimetry*, **115**(1-4), 44–50.

Ziegler, James F. 1996. Terrestrial cosmic rays. *IBM journal of research and development*, **40**(1), 19–39.

Ziegler, James F., Curtis, Huntington W., Muhlfeld, Hans P., Montrose, Charles J., Chin, B., Nicewicz, Michael, Russell, C. A., Wang, Wen Y., Freeman, Leo B., Hosier, P., LaFave, L. E., Walsh, James L., Orro, José M., Unger, G. J., Ross, John M., O'Gorman, Timothy J., Messina, B., Sullivan, Timothy D., Sykes, A. J., Yourke, H., Enger, Thomas A., Tolat, Vikram R., Scott, T. S., Taber, Allen H., Sussman, R. J., Klein, W. A., & Wahaus, C. W. 1996. IBM experiments in soft fails in computer electronics (1978-1994). *IBM Journal of Research and Development*, **40**, 3–18.